Facile Synthesis of Pd-Based Core@Shell Catalysts for Improved Stability and Activity

by

Chang Yup Seo

A dissertation submitted in partial fulfillment
of the requirements for the degree of
Doctor of Philosophy
(Chemical Engineering)
in the University of Michigan
2018

Doctoral Committee:

Professor Johannes W. Schwank, Chair
Professor Mark A. Barteau
Adjunct professor Galen B. Fisher
Professor Richard M. Laine

Chang Yup Seo

cyseo@umich.edu

ORCD iD: 0000-0001-9587-3274

Acknowledgements

The completion of this dissertation would not have been possible without the help of many individuals and organizations. The financial support was provided by the Ford motor company, the US Department of Energy, and the University of Michigan. Research collaboration with Oak Ridge National Laboratory and Michigan Center of Materials Characterization is acknowledged.

I thank Dr. Kai Sun and Dr. Haiping Sun at Michigan Center of Materials Characterization for their help in training/operating transmission electron microscope (TEM), which was critical for my research. I owe many thanks to the collaborators at Oak Ridge National Laboratory, Dr. Todd Toops, Dr. Andrew Binder, Dr. Eleni Kyriakidou, and Dr. Lawrence Allard for providing meaningful insights and an opportunity to obtain in-situ TEM results. I would also like acknowledge the collaborators at Ford Motor Co., Dr. Christine Lambert, Dr. Joseph Theis, and Dr. Andrew (Bean) Getsoian for sharing their expert knowledge in automotive catalysts.

My fellow students at Schwank Group provided emotional and intellectual support over the past years. In particular, I am grateful to professor Galen Fisher, Dr. Xiaoyin Chen, Dr. Lei Ma, Mohit Nahata, Cigdem Kokenoz, and Dr. Kevin Dahlberg for their mentorship, ideas, collaborations, and encouragement at difficult times. People who are not member of the group: Dr. Eongyu Yi, Amin Reihani, and my committee members, professor Mark Barteau and professor Richard Laine offered a tremendous help in my research, hence is acknowledged here. Above all, I thank my advisor, professor Johannes Schwank, for the support and suggestions for new ideas which led to interesting results and allowed me to complete this dissertation.

Lastly and most importantly, I thank my family members: my father, Junik Seo, my mother, Hyangsuk Lee, my brother, Hyungyo Seo, my wife Marie Tata, and all the other Tatas. Without their unconditional love and support, I would not be standing where I am now.

Table of Contents

List of Tables

List of Figures

Abstract

Discovery of catalysts with improved durability, activity, and selectivity may provide solutions for environmental and energy issues. One of the recent developments in such materials is to use core@shell architectures, in which two materials are synthesized in two concentric spheres with an oxide shell surrounding a metal core. This morphology provides not only a barrier to sintering but also facilitates strong metal-support interactions by maximizing the number of perimeter sites. However, commonly known synthesis methods for core@shell nanomaterials are often complicated and expensive, which has hindered extensive research using this architecture. In this thesis, some creative uses of core@shell materials as model catalysts are introduced. The outcome of this study provides new and useful information about the thermal stability and metal-support interactions of Pd-based core@shell materials.

First, a simple, one-pot and scalable synthesis has been explored, targeting palladium@silica (Pd@SiO_2) core@shell catalysts in an aqueous environment at room temperature. The method offers independent tunability of the Pd cores size (D = 1.6±0.4, 2.7±0.4, and 3.5±0.4 nm) and the SiO_2 shell thickness (D = 24±3, 31±4, and 43±6 nm). The catalysts also have very high surface areas (BET: 519-1165 m^2/g) and high mesopore volumes (1.3-1.8 cm^3/g). Based on transmission electron microscopy (TEM) images, a new mechanism for SiO_2 shell formation around Pd cores is proposed. CO oxidation and TEM were used to probe the thermal stability of the catalysts. Surprisingly, improved CO light-off was observed after

aging above 800 °C, in striking contrast with the catalytic activity of impregnation-prepared Pd/SiO_2 supported catalysts with a similar Pd loading.

To explain the improved activity after aging at elevated temperature, we used a combination of catalytic activity measurements and TEM studies and obtained direct evidence of Pd redispersion from nanoparticles (~ 4 nm) to smaller atom clusters (≤ 2 nm). The improved catalytic CO oxidation activity of $Pd@SiO_2$ after high temperature aging was consistent with the TEM results. TEM analysis also indicated that the activity enhancement by aging is attributed to the core@shell geometry, which allows the Pd particles to redisperse within the internal mesopores of the silica shells.

The synthesis method was also applied to prepare Pd nanoparticles encapsulated by CeO_2, aiming to enhance the catalytic activity. A metalloorganic compound, cerium (IV) atrane, was prepared and used as a water-stable CeO_2 precursor. The CeO_2 shell of the synthesized $Pd@CeO_2$ nanoparticles is composed of 2-5 nm crystals exhibiting both micro- and meso-pores. The catalyntic activity as well as the accessibility of reactants to the Pd core are confirmed by CO oxidation, where excellent low temperature activity was observed. The thermal stability of the as-prepared $Pd@CeO_2$ can be enhanced by two methods: (1) forming CeO_2-ZrO_2 solid solutions and (2) forming SiO_2 secondary shells as barrier to sintering.

On successful expansion of the synthesis method to another shell material, application of core@shell materials as three-way auto exhaust catalysts was studied. It was found that the catalysts' hydrothermal stability could be improved by using different shell materials. However, aging at elevated temperature often destroyed the core@shell architecture due to Pd vaporization and shell recrystallization. Moreover, even this facile synthesis method was found unsuitable for

producing catalysts at volumes required by industry. Therefore, the focus shifted towards using the Pd@CeO_2 as a model catalyst to study Pd-CeO_2 interaction. Using core@shell geometry, the quantification of metal-support interaction was simplified.

Chapter 1

Introduction

The modern society is not sustainable without catalysts. For example, the world's food supply relies heavily on nitrogen fixation by the Haber-Bosch process, which is unsustainable without aid of a catalyst [1]. Catalysts also play vital roles in the production of consumer and commodity chemicals, refining and reforming of petrochemicals, and in environmental applications. The importance of catalyst application to a chemical process is reflected in its market estimated to show an annual 4.2% growth from 2016 to 2024, becoming a 34-billion-dollar market in 2024 [2]. Such rapid market growth is very reasonable, since catalysts enable us to achieve higher energy and material efficiency by providing improved activity and selectivity. As of today, there is an ongoing demand for catalysts with higher activity [3-6], selectivity [7-9], and durability [10-14] also represented by the amount of research targeting catalytic materials and applications.

Catalyst deactivation due to metal sintering

Although catalysts should not undergo change, per definition, catalyst degradation is unavoidable. In many catalytic processes, the materials are exposed to harsh conditions that can cause loss of activity (deactivation). Of the six categories of catalyst deactivation [15, 16], thermal degradation is particularly an issue for environmental catalytic processes which often

operate at elevated temperatures [17-19]. Representative environmental catalyst applications, highly affected by thermal degradation are automotive emission control catalysts. First commercialized in 1975, the gasoline three-way auto exhaust catalysts have successfully minimized air pollution from mobile sources [20, 21]. The catalyst, which oxidizes hydrocarbons and carbon monoxide while reducing nitrous oxides, is activated by waste heat from combustion and thus is directly exposed to the engine exhaust. The exhaust contains a large amount of vapor and may reach over 1000 °C when high power output is required. Such environments place the catalyst under hydrothermal stress which often induces loss of active sites due to metal sintering [22].

Metal sintering is a phenomenon where the exposed active sites decrease due to particle growth [23-25]. Typically, catalysts are prepared by loading an active material such as platinum group metals (PGM) or transition metals on a support with a high surface area. It is often advantageous to obtain high dispersion (small particle size) of the active species to expose more active sites to participate in the reaction. Therefore, in general, catalyst supports are required to be thermally stable to minimize changes in morphology during operation. However, upon exposure to elevated temperatures, metal particles tend to sinter to larger particles via processes such as particle migration and coalescence (PMC), and atomic migration (Ostwald ripening) [17, 26-29]. Upon sintering, a catalyst often undergoes a significant loss of activity, because the metal particles increase in size and consequently, the relative number of active metal atoms on the surface decreases. Therefore, the overall activity of a catalyst would decrease, although turnover frequency (TOF) per active site may stay constant. In addition, sintering may also cause changes in the reaction pathway, since surfaces of a larger metal particles are composed of atoms with high coordination (i.e., terraces) while the surface atoms of a smaller metal particles have lower

coordination (i.e., steps, kinks). Therefore, particle sintering would change the reaction results by favoring the reaction that occurs on atoms with high coordination numbers, if the reaction is structure sensitive [30-32]. Nonetheless, sintering is one of the leading causes for catalyst deactivation, often requiring the catalyst to be replaced or regenerated.

Nanomaterials with core@shell geometries

Despite the tremendous research efforts to prevent sintering, no one has found a solution that prevents sintering from occurring. However, in the past decade, the development of nanomaterial syntheses and analysis suggest a few possible pathways to prevent or slow down sintering. Many different methods such as metal anchoring onto support [33-35], atomic-layer deposition [36, 37], and metal particle embedding [12, 38, 39] have been reported to improve catalysts' thermal stability. Core@shell nanomaterials comprised of an active core, such as PGM, encapsulated in a porous shell, such as SiO_2. It has been reported that, if used correctly, catalysts with core@shell morphologies can exhibit thermal stability unattainable by conventional, supported, catalysts with similar compositions. A graphical comparison between core@shell and supported architectures is shown in Figure 1.1.

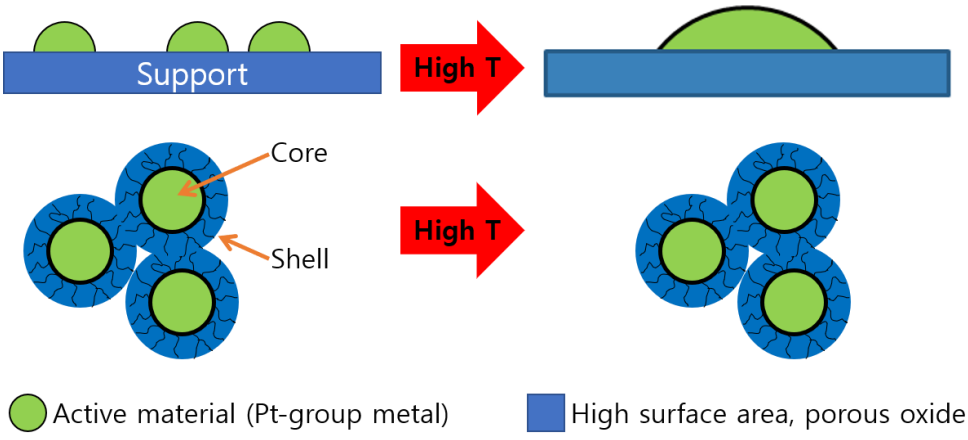

Figure 1.1 Graphical representation of elevated thermal stability expressed by (bottom) core@shell architecture compared to (top) traditional, supported catalyst architecture.

Many types of core@shell catalysts have been synthesized and used to demonstrate elevated thermal stability [12, 39, 40]. The working hypothesis is that by encapsulating an active (but less thermally stable) core with a thermally stable shell, which is often much less active, one can provide a sintering barrier for the cores. Since the active sites are mainly provided by the cores, the shell must remain porous after exposure to elevated temperatures to allow reactants to access the active core while transporting reaction products away. Therefore, the choice of the shell materials has been limited to an amorphous oxide material with high thermal stability such as silica or an aluminosiliate [41]. However, diverse cores in both PGM (Pt [10, 42, 43], Pd [44-46], Au [12, 47-49]) and transition metals (Fe [41, 50], Cu [51], Ni [39, 52, 53], Co [54]) have been encapsulated successfully by SiO_2 to impart improved thermal stability, demonstrating that catalyst thermal stability may be altered by a simple change in morphology.

Another characteristic of core@shell catalysts, is that the geometry offers high degree of metal-support interaction sites. It is well-known that a catalytic metal's activity can be altered based on the support. For example, CeO_2 is known to provide active oxygen to a supported PGM, enabling low-temperature oxidation. Another well-known example is the interaction between Au and TiO_2, which can catalyze CO oxidation below room temperature [55]. It is understood that such low-temperature activity is caused by the support supplying oxygen to the metal surface sites occupied by CO [56, 57]. Therefore, it is reasonable that many studies suggest that the interfacial metal atoms, those in contact with the active support, are responsible for high activity at low temperatures.

For traditional supported catalysts, the number of interfacial sites can be maximized by minimizing the metal particle size [58-61]. However, as small metal particles are prone to

sintering, the number of interfacial sites diminishes quickly at elevated temperatures or even by the exothermic reactions. Therefore, it is difficult to isolate and quantify the activity enhancement contributed by metal-support interactions. One way to account for this difficulty is to use core@shell materials as model catalysts. The geometry, theoretically, offers metal-support interactions between all the metal core's surface atoms in all directions which emphasizes the activity enhancement caused by the interaction. In addition, the geometry suppresses metal sintering, enabling the metal-support interaction to be investigated apart from the effect of sintering.

Synthesis methods for core@shell materials

Since the advantages of core@shell catalysts over supported catalysts have been reported repeatedly over the last decade, one might ask: Why is it not yet implemented in practical catalytic processes? The underlying reason for the mismatch is that the preparation of nanoscale core@shell materials is too expensive. While various core@shell nanomaterial synthesis methods have been developed [12, 44, 62, 63], these methods are often very complicated, involve the use of toxic organic solvents or metal cores that must be separated and re-dispersed [45]. Compared to a commonly-used catalyst preparation method, impregnation, such processes are much higher in cost and time of catalyst production. Furthermore, typical core@shell syntheses (Figure 1.2, top) do not lend themselves to scale-up. Therefore, for core@shell catalysts to be implemented in practical processes, breakthroughs in synthesis are necessary.

Recently, a few researchers have reported a simplified synthesis method, often referred as one-pot two-step synthesis. In this synthesis method, the cores and the shells are synthesized in the same pot, without separation (Figure 1.2, bottom). Furthermore, successful exclusion of

organic solvents from the synthesis has also been demonstrated, which may significantly reduce the cost of catalyst production.

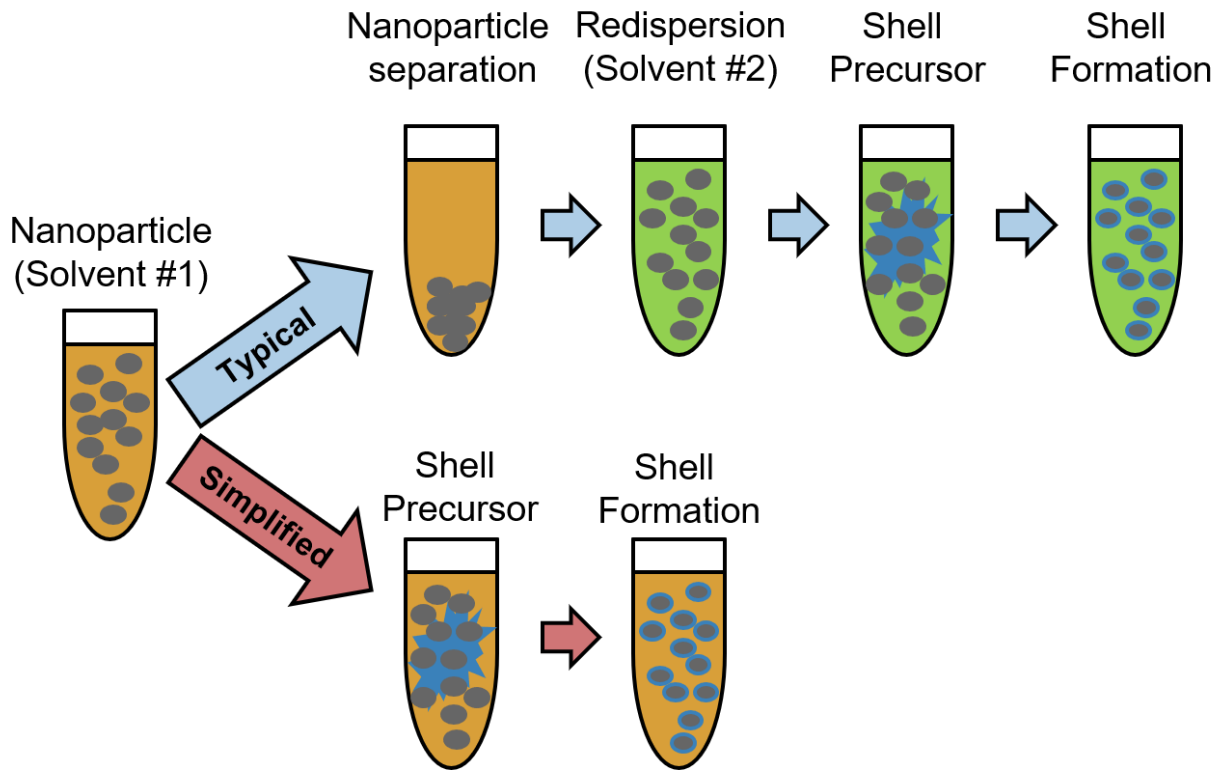

Figure 1.2 Graphical representation of core@shell nanomaterial preparation. (top) A typical method requires nanoparticle re-dispersion and solvent exchange while (bottom) a recently developed simplified synthesis method does not.

Such breakthroughs in synthesis have allowed us to push the boundaries and control the catalysts' morphologies, beyond achieving core@shell geometries. The work presented in Chapter 2 approaches the synthesis with independent tunability of the core and the shell sizes, by looking at the core@shell formation mechanism. By carefully studying the formation mechanism of Pd@SiO_2 nanoparticles, independent tunability of the core and the shell sizes have been achieved using the one-pot two-step synthesis method. The relationship between the formation of Pd@SiO_2 and each step of the synthesis was studied, resulting a discovery of formation mechanism of core@shell geometries instead of random mixture of Pd and SiO_2 nanoaprticles.

To test the prepared Pd@SiO_2 nanoparticles' catalytic activity, CO oxidation was used to probe how the catalysts' activity correlates with core size. In addition, the prepared catalysts were thermally stable up to 850 °C, one of the highest temperature reported for Pd@SiO_2 catalysts.

Upon successful synthesis of Pd@SiO_2, the next step was to apply the method to another material: CeO_2. Although silica can be a good support material with high surface areas and thermal stability, the material itself is known to be inert. In other words, no metal-support interaction can be expected between the core and the shell. However, the formation of shells, other than SiO_2, in aqueous environments has been challenging. Work in Chapter 3 successfully provides a possible solution to the challenge and provides a pathway towards achieving one-pot two-step synthesis of Pd@CeO_2 in aqueous environment [64]. As expected, the prepared catalyst exhibits much better low-temperature CO oxidation activity compared to its counterpart, Pd@SiO_2. Furthermore, the core and shell sizes of Pd@CeO_2 were also independently tunable. After successful synthesis of Pd@CeO_2, the same synthesis method was applied to prepare core@shell materials that contain a shell with more than one oxide as its component for elevated thermal stability.

Core@shell materials as catalysts

As implied above, a significant effort was spent to understand the formation mechanism and perfecting the synthesis of Pd-based core@shell materials. This ability to synthesize the materials was exploited for the next portion of the thesis: study of core@shell nanomaterials as model catalysts. Currently, core@shell materials are not used in real-life applications, because of the cost of production. However, it was demonstrated that the cost of production can be reduced by simplifying the synthesis. Therefore, it was worth investigating catalytic application of core@shell materials under realistic operating conditions. In Chapter 4, the application of

core@shell catalysts as three-way auto exhaust catalyst (TWC) are studied, based on the criteria that a three-way catalyst must have high thermal stability and high activity which can be expected from core@shell catalyst. In this chapter, different combinations of core@shell materials were explored under a realistic gasoline exhaust environment [65]. By comparing the catalysts' performance before and after severe hydrothermal aging, design parameters for core@shell catalysts with different compositions are suggested in order to obtain better activity and hydrothermal stability.

Apart from material screening, a more fundamental materials study was also conducted using core@shell catalysts. In a core@shell geometry, each core is encapsulated in one shell, which helps identifying morphological change of the core [66]. In Chapter 5, the geometry was used to explore the behavior of palladium at elevated temperature. In the past, a few reports, including one by us, reported redispersion of Pd at temperatures near 700 °C [67, 68]. However, the mechanism is not clearly understood. In this chapter, redispersion is much more clearly demonstrated by using Pd@SiO_2 as model catalyst. The work clearly demonstrates Pd redispersion which only occurs above 700 °C. Furthermore, the underlying reason for apparent thermal stability enhancement in core@shell catalyst was explained by comparing the behavior of Pd nanoparticle between the core@shell and supported geometries.

Aim and scope of this thesis

The aim of this thesis is to provide a facile core@shell nanomaterial synthesis method and to expand catalytic applications of the material. In this thesis, simplified steps leading to the preparation of core@shell nanomaterial are demonstrated, with minimal laboratory set up. In particular, independent tunability of the core and the shell size was achieved, which has not yet been studied in detail. Upon successful synthesis, the prepared materials were used as model

catalysts to investigate the thermal stability enhancement, metal-support interaction, and behavior of PGM under sintering conditions. Chapter 6 and 7 summarizes the new findings and provides preliminary results for a future work regarding metal-support interaction in a core@shell geometry.

References

[1] P.H. Emmett, J.T. Kummer, Industrial & Engineering Chemistry 35 (1943) 677-683.

[2] Catalyst Market Size Expected To Reach $34.3 Billion By 2024, June 2016 ed., Grand View Research, 2016.

[3] H.-L. Jiang, T. Akita, Q. Xu, Chemical Communications 47 (2011) 10999-11001.

[4] D.-H. Lee, J.-Y. Jung, M.-J. Jin, Green Chemistry 12 (2010) 2024-2029.

[5] K.L. Billingsley, K.W. Anderson, S.L. Buchwald, Angewandte Chemie International Edition 45 (2006) 3484-3488.

[6] M. Cargnello, J.J.D. Jaén, J.C.H. Garrido, K. Bakhmutsky, T. Montini, J.J.C. Gámez, R.J. Gorte, P. Fornasiero, Science 337 (2012) 713-717.

[7] Y. Wang, J. Yao, H. Li, D. Su, M. Antonietti, Journal of the American Chemical Society 133 (2011) 2362-2365.

[8] H. Klein, R. Jackstell, K.-D. Wiese, C. Borgmann, M. Beller, Angewandte Chemie International Edition 40 (2001) 3408-3411.

[9] J. Bao, J. He, Y. Zhang, Y. Yoneyama, N. Tsubaki, Angewandte Chemie 120 (2008) 359-362.

[10] S.H. Joo, J.Y. Park, C.-K. Tsung, Y. Yamada, P. Yang, G.A. Somorjai, Nature Matererials 8 (2009) 126-131.

[11] J.-N. Park, A.J. Forman, W. Tang, J. Cheng, Y.-S. Hu, H. Lin, E.W. McFarland, Small 4 (2008) 1694-1697.

[12] J. Chen, R. Zhang, L. Han, B. Tu, D. Zhao, Nano Research 6 (2013) 871-879.

[13] C.W. Han, P. Majumdar, E.E. Marinero, A. Aguilar-Tapia, R. Zanella, J. Greeley, V. Ortalan, Nano Letters 15 (2015) 8141-8147.

[14] F. Wei, C. Cao, Y. Sun, S. Yang, P. Huang, W. Song, ChemCatChem 7 (2015) 2475-2479.

[15] C.H. Bartholomew, Applied Catalysis A: General 212 (2001) 17-60.

[16] J.A. Moulijn, A.E. van Diepen, F. Kapteijn, Applied Catalysis A: General 212 (2001) 3-16.

[17] T.W. Hansen, A.T. DeLaRiva, S.R. Challa, A.K. Datye, Accounts of Chemical Research 46 (2013) 1720-1730.

[18] V. Blasco, C. Royo, A. Monzón, J. Santamaría, AIChE Journal 38 (1992) 237-243.

[19] P. Euzen, J.-H. Le Gal, B. Rebours, G. Martin, Catalysis Today 47 (1999) 19-27.

[20] M. Shelef, R.W. McCabe, Catalysis Today 62 (2000) 35-50.

[21] H.S. Gandhi, G.W. Graham, R.W. McCabe, Journal of Catalysis 216 (2003) 433-442.

[22] Q. Xu, K.C. Kharas, B.J. Croley, A.K. Datye, ChemCatChem 3 (2011) 1004-1014.

[23] C.T. Campbell, S.C. Parker, D.E. Starr, Science 298 (2002) 811-814.

[24] J.J. Chen, E. Ruckenstein, Journal of Catalysis 69 (1981) 254-273.

[25] A.K. Datye, Q. Xu, K.C. Kharas, J.M. McCarty, Catalysis Today 111 (2006) 59-67.

[26] S.B. Kang, S.J. Han, S.B. Nam, I.-S. Nam, B.K. Cho, C.H. Kim, S.H. Oh, Topics in Catalysis 56 (2013) 298-305.

[27] S.B. Kang, J.B. Lim, D. Jo, I.-S. Nam, B.K. Cho, S.B. Hong, C.H. Kim, S.H. Oh, Chemical Engineering Journal 316 (2017) 631-644.

[28] R.J. Liu, P.A. Crozier, C.M. Smith, D.A. Hucul, J. Blackson, G. Salaita, Applied Catalysis A: General 282 (2005) 111-121.

[29] S.B. Simonsen, I. Chorkendorff, S. Dahl, M. Skoglundh, S. Helveg, Surface Science 648 (2016) 278-283.

[30] B. Atalik, D. Uner, Journal of Catalysis 241 (2006) 268-275.

[31] M. Bowker, Q. Guo, Y. Li, R.W. Joyner, Catalysis Letters 18 (1993) 119-123.

[32] R.A. Van Santen, Accounts of Chemical Research 42 (2009) 57-66.

[33] C.T. Campbell, J.R.V. Sellers, Faraday Discussions 162 (2013) 9-30.

[34] X. Liu, Q. Zhu, Y. Lang, K. Cao, S. Chu, B. Shan, R. Chen, Angewandte Chemie International Edition 56 (2017) 1648-1652.

[35] Z. Li, N.M. Schweitzer, A.B. League, V. Bernales, A.W. Peters, A.B. Getsoian, T.C. Wang, J.T. Miller, A. Vjunov, J.L. Fulton, J.A. Lercher, C.J. Cramer, L. Gagliardi, J.T. Hupp, O.K. Farha, Journal of the American Chemical Society 138 (2016) 1977-1982.

[36] H. Feng, J. Lu, P.C. Stair, J.W. Elam, Catalysis Letters 141 (2011) 512-517.

[37] J. Lu, B. Fu, M.C. Kung, G. Xiao, J.W. Elam, H.H. Kung, P.C. Stair, Science 335 (2012) 1205-1208.

[38] Y.H. Ng, S. Ikeda, T. Harada, T. Sakata, H. Mori, A. Takaoka, M. Matsumura, Langmuir 24 (2008) 6307-6312.

[39] K.A. Dahlberg, J.W. Schwank, Chemistry of Materials 24 (2012) 2635-2644.

[40] Y. Xu, J. Ma, Y. Xu, L. Xu, L. Xu, H. Li, H. Li, RSC Advances 3 (2013) 851-858.

[41] J. Yang, D. Shen, Y. Wei, W. Li, F. Zhang, B. Kong, S. Zhang, W. Teng, J. Fan, W. Zhang, S. Dou, D. Zhao, Nano Research 8 (2015) 2503-2514.

[42] N. Almana, S.P. Phivilay, P. Laveille, M.N. Hedhili, P. Fornasiero, K. Takanabe, J.-M. Basset, Journal of Catalysis 340 (2016) 368-375.

[43] X. Wang, D. Liu, S. Song, H. Zhang, Journal of the American Chemical Society 135 (2013) 15864-15872.

[44] K. Bakhmutsky, N.L. Wieder, M. Cargnello, B. Galloway, P. Fornasiero, R.J. Gorte, ChemSusChem 5 (2012) 140-148.

[45] M. Cargnello, N.L. Wieder, T. Montini, R.J. Gorte, P. Fornasiero, Journal of the American Chemical Society 132 (2010) 1402-1409.

[46] A.J. Forman, J.-N. Park, W. Tang, Y.-S. Hu, G.D. Stucky, E.W. McFarland, ChemCatChem 2 (2010) 1318-1324.

[47] B. Li, T. Gu, T. Ming, J. Wang, P. Wang, J. Wang, J.C. Yu, ACS Nano 8 (2014) 8152-8162.

[48] T. Mitsudome, M. Yamamoto, Z. Maeno, T. Mizugaki, K. Jitsukawa, K. Kaneda, Journal of the American Chemical Society 137 (2015) 13452-13455.

[49] J.-T. Song, X.-S. Zhang, M.-Y. Qin, Y.-D. Zhao, Dalton Transactions 44 (2015) 7752-7756.

[50] J. Lee, Y. Lee, J.K. Youn, H.B. Na, T. Yu, H. Kim, S.-M. Lee, Y.-M. Koo, J.H. Kwak, H.G. Park, H.N. Chang, M. Hwang, J.-G. Park, J. Kim, T. Hyeon, Small 4 (2008) 143-152.

[51] Q. Yao, Z.-H. Lu, Z. Zhang, X. Chen, Y. Lan, 4 (2014) 7597.

[52] W. Fu, H. Yang, L. Chang, M. Li, H. Bala, Q. Yu, G. Zou, Colloids and Surfaces A: Physicochemical and Engineering Aspects 262 (2005) 71-75.

[53] H. Peng, X. Zhang, L. Zhang, C. Rao, J. Lian, W. Liu, J. Ying, G. Zhang, Z. Wang, N. Zhang, X. Wang, ChemCatChem 9 (2017) 127-136.

[54] J. Wagner, T. Autenrieth, R. Hempelmann, Journal of Magnetism and Magnetic Materials 252 (2002) 4-6.

[55] S.D. Lin, M. Bollinger, M.A. Vannice, Catalysis Letters 17 (1993) 245-262.

[56] M.M. Schubert, S. Hackenberg, A.C. van Veen, M. Muhler, V. Plzak, R.J. Behm, Journal of Catalysis 197 (2001) 113-122.

[57] D. Widmann, R.J. Behm, Angewandte Chemie International Edition 50 (2011) 10241-10245.

[58] L. Artiglia, F. Orlando, K. Roy, R. Kopelent, O. Safonova, M. Nachtegaal, T. Huthwelker, J.A. van Bokhoven, The Journal of Physical Chemistry Letters 8 (2017) 102-108.

[59] T.P. Senftle, A.C.T. van Duin, M.J. Janik, ACS Catalysis 7 (2017) 327-332.

[60] G.C. Bond, Surface Science 156 (1985) 966-981.

[61] R. Peng, S. Li, X. Sun, Q. Ren, L. Chen, M. Fu, J. Wu, D. Ye, Applied Catalysis B: Environmental 220 (2018) 462-470.

[62] Y. Hu, K. Tao, C. Wu, C. Zhou, H. Yin, S. Zhou, The Journal of Physical Chemistry C 117 (2013) 8974-8982.

[63] J. Zhang, L. Li, X. Huang, G. Li, Journal of Materials Chemistry 22 (2012) 10480-10487.

[64] C. Seo, E. Yi, M. Nahata, R.M. Laine, J.W. Schwank, Materials Letters 206 (2017) 105-108.

[65] K.L.S. Masias, T.C. Peck, P.T. Fanson, RSC Advances 5 (2015) 48851-48855.

[66] S. Zhang, C. Chen, M. Cargnello, P. Fornasiero, R.J. Gorte, G.W. Graham, X. Pan, Nature Communications 6 (2015) 7778.

[67] H. Lieske, J. Voelter, The Journal of Physical Chemistry 89 (1985) 1841-1842.

[68] J.A. Lupescu, J.W. Schwank, K.A. Dahlberg, C.Y. Seo, G.B. Fisher, S.L. Peczonczyk, K. Rhodes, M.J. Jagner, L.P. Haack, Applied Catalysis B: Environmental 183 (2016) 343-360.

Chapter 2

Tunable particle size and remarkable thermal stability of Pd@SiO_2 catalysts: synthesis and CO oxidation

Introduction

Platinum group metal (PGM) based catalysts such as palladium, platinum, and rhodium are widely used in chemical, energy, and environmental applications because of their high activity and stability [1-4]. Such catalysts are conventionally prepared by impregnating a high surface area oxide support (such as alumina or silica) with metal precursor solutions to obtain highly dispersed metal particles. Unfortunately, when exposed to pretreatment and reaction conditions at elevated temperatures, the initially finely dispersed small metal particles agglomerate and sinter into larger ones [5-8]. Such sintering decreases surface metal sites leading to catalyst deactivation. One promising strategy to mitigate this degradation is to encapsulate active metal nanoparticles (NP) in thermally stable oxides, forming core@shell geometries. In this type of catalyst architecture, a porous oxide shell at nanoscale thickness protects an active metal core, allowing reactants and reaction products to be transported through the pores [9-12]. Taking Pd@SiO_2 as an example, previous studies have demonstrated that the core@shell geometry not only improves activity but also imparts sintering-tolerance in many important reactions such as oxidation [9, 13, 14], hydrogenation [9], and Suzuki-Miyaura coupling

reactions [15]. However, despite the numerous studies conducted on the preparation of core@shell structures, the mechanistic details of core@shell formation are not well understood. Consequently, it is quite challenging to come up with a synthesis method that leads to predictable, reproducible, and tunable particle morphologies. Therefore, via this investigation, we would like to address the following questions:

- Can we develop and demonstrate a simple Pd@SiO_2 nanoparticle synthesis method that offers independent tunability of both the metal core diameter and the shell thickness?
- Will the Pd@SiO_2 catalyst possess better sintering resistance at high temperatures than a conventionally prepared Pd/SiO_2 supported catalyst?

To answer the first question, we must acknowledge that preparing a core@shell catalyst is very complex compared to preparing conventional catalysts by impregnation. To date, two major synthesis methods have commonly been used to encapsulate metal nanoparticles in nanoscale shells.

One method uses water-in-oil reverse-micelles as templates. In this process, the core metal NPs are prepared by reducing a water-soluble metal precursor within each reverse-micelle, forming one core within one micelle. Following reduction, a metalloorganic shell precursor is hydrolyzed around the micelles reacting with the water trapped within the micelles, encapsulating the metal particles. This method, however, has two significant drawbacks. First, it requires a large quantity of organic solvent to obtain only a small amount of catalyst, because reverse-micelles are only stable at very high surfactant:water ratios [9, 16, 17]. Moreover, the catalyst morphology may not be tuned easily, because the micelles can be easily destabilized by

small swings in chemical parameters such as pH, surfactant:water ratio, and co-surfactant concentrations.

The second commonly used method, where the metal NPs are first prepared in a separate environment and then in a second step mixed with the shell precursor to finish the encapsulation, allows better control of the catalyst morphology [10, 18-20]. However, this method requires the core NPs to be prepared, separated, purified, and re-dispersed prior to encapsulation. Since there is no guarantee of preserving all the cores throughout the separation and purification processes, the final catalyst composition and morphology cannot be easily predicted or reproduced. Furthermore, this approach may not be suitable for preparing catalysts with core sizes smaller than 10 nm [10, 20, 21], because the separation and re-dispersion of small nanoparticles are labor intensive.

Recently, a modified two-step process has been developed in an attempt to solve the challenges in scalability, repeatability, and tunability with the two methods mentioned above [14, 22]. While this represents a significant advance, some synthesis challenges still remain. As an example, Joo et al. observed that the formation of core@shell geometries was heavily dependent on the amount of SiO_2 precursor (TEOS) used. Attempts to modify the SiO_2 shell thickness by using smaller or larger amounts of TEOS resulted in non-uniform shell structures around the Pt cores [10]. A similar result was reported by Hu et al. [14]; who tried to establish the shell size control by increasing the amount of TEOS. However, numerous SiO_2 particles without Pd cores were formed instead. Both of these articles did not explicitly report core size tuning, as is also the case for many other articles regarding PGM@SiO_2 synthesis. Apparently, this shows that the core@shell formation mechanism in such two-step processes needs more systematic investigation.

Here, we report a one-pot two-step synthesis of $Pd@SiO_2$ with independently tunable Pd core and SiO_2 shell sizes, demonstrating that it is possible to overcome the scalability, repeatability, and tunability issues. First, we explored the core@shell formation mechanism in a water-based modified two-step process. Guided by these mechanistic insights, we successfully synthesized $Pd@SiO_2$ catalysts using palladium (II) nitrate as the Pd precursor, as opposed to commonly used chlorinated Pd precursors [9, 14], to avoid potential chlorine poisoning [23, 24] as well as complex formation between chlorine and metal ions [25-27]. This synthesis method allows the Pd core sizes and shell thicknesses to be controlled independently over a wide range. It is also important to note that this catalyst preparation method lends itself to scale-up by simply increasing the batch size. Finally, we confirmed that core@shell catalysts outperformed conventional Pd/SiO_2 catalysts in terms of CO oxidation activity even after aging up to 850 °C. The underlying reason for the thermal stability of the core@shell geometry is demonstrated directly by high-resolution TEM analysis.

Experimental

Synthesis of $Pd@SiO_2$ catalysts

Palladium (II) nitrate dihydrate ($Pd(NO_3)_2 \times 2H_2O$, 99%, Sigma Aldrich) and potassium tetrachloropalladate (II) (K_2PdCl_4, 99.99%, Acros Organics) were used as two different Pd precursors for the synthesis of $Pd@SiO_2$ catalysts. 64% hydrazine hydrate ($N_2H_4 \times H_2O$, Acros Organics) solution was used to reduce Pd^{2+} into Pd nanoparticles during the first step (nanoparticle formation). Tetraethoxysilane (TEOS, 98%, Sigma Aldrich) diluted in ethanol was used as SiO_2 precursor. Tetradecyltrimethylammonium bromide (TTAB, 98%, MP Biomedicals)

and hexadecyltrimethylammonium bromide (CTAB, 95%) were used as the structural template to form mesoporous SiO_2 shell. Sodium hydroxide (Sigma Aldrich) was used to control the rate of TEOS hydrolysis. The general synthesis scheme is shown in Figure 2.1. The general scheme follows a one-pot, modified two-step procedure, where no organic solvents were used except for a small amount of ethanol for the dilution of TEOS. No purification and re-dispersion of palladium nanoparticles were needed prior to silica shell encapsulation. In addition, all synthesis steps were carried out at room temperature, open to the atmosphere.

We adapted and modified the general procedures for the synthesis of water-soluble Pd-NP described by Veisz and Király [28], where the size-selective synthesis of cubooctahedral Pd particles was carried out through the reduction of $[PdCl_4]^{2-}$ by hydrazine in the presence of either CTAB or TTAB aqueous solution. In our general synthesis, an aqueous palladium nanoparticle (Pd-NP) suspension was prepared by dissolving $Pd(NO_3)_2$ or an equivalent molar amount of K_2PdCl_4 de-ionized (DI) water and adding CTAB or TTAB and hydrazine to convert Pd^{2+} to Pd^0 and stabilize the Pd-NP suspension. Following the Pd-NP preparation, the silica shell was deposited by adding an ethanolic solution of TEOS to the aqueous Pd-NP suspension, after pH adjustment by NaOH, as shown in Figure 2.1.

In a typical synthesis (3Pd-12Si in Table 2.1, representing $Pd@SiO_2$ with 3 nm Pd core and 12 nm shell thickness, thereafter), 20 mL of 10 mmol/L aqueous solution of TTAB (0.2 mmol) was stirred in a flask with a stir bar. To the stirring solution, 20 ml of 1.3 mmol/L $Pd(NO_3)_2 \times 2H_2O$ solution (30.0×10^{-3} mmol) was added. Upon addition, the color of the solution turned from pale yellow to orange-red, indicating palladium-surfactant complex formation. Pd^{2+} in the complex was reduced immediately by adding 5.0 mL of the hydrazine aqueous solution (1.8 mmol), which was prepared in advance by diluting 1 mL $N_2H_4 \times H_2O$ by 50 mL DI water.

The color of the solution turned to clear black from ornage-red and the solution was left to stir for the next 30 min to allow hydrazine decomposition. After stirring for 30 min, 0.06 mol/L aqueous NaOH solution was added to adjust the pH of the nanoparticle suspension to 10.7. Then, a 5 mL of ethanol-diluted TEOS solution (2.7 mmol TEOS), prepared by 6 mL TEOS dissolved in 50 mL dry ethanol, was added to the above pH adjusted Pd nanoparticle suspension under constant stirring condition. After the addition of TEOS, the solution was left to stir for 24 h to allow the hydrolysis of TEOS and the silica shell development. Over 24 h, the color of the solution turned from clear black to opaque black, indicating silica condensation. The final core@shell particles were collected via centrifugation at 4000 rpm. The collected core@shell nanoparticles were washed twice with DI water followed by three times with ethanol to remove residual base and surfactant.

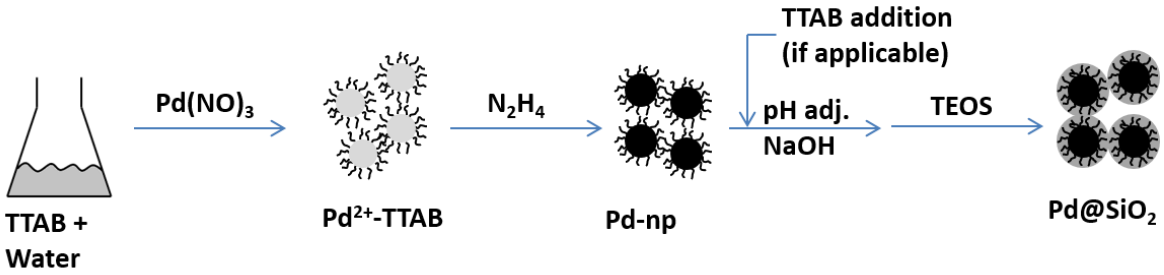

Figure 2.1 One-pot, two step synthesis schematic for $Pd@SiO_2$ catalysts.

Table 2.1 Conditions and parameters for the tunable synthesis of $Pd@SiO_2$ catalysts.

	Synthesis conditions and parameters in precursor solution				Parameters and compositions in products dried at 80 °C		
Sample	$[Pd^{2+}]$ ($\times 10^{-3}$, mmol)	TTAB (mmol)	Hydrazine (mmol)	TEOS (mmol)	Pd[a] (wt.%)	D_{core}[b] (nm)	D_{shell}[b] (nm)
2Pd-16Si	7.5	0.2	0.5	2.7	1.2	1.8	31.3
3Pd-12Si	30.0	0.2	1.8	2.7	3.2	2.7	24.9
4Pd-12Si	120.0	0.2	7.1	2.7	10.8	3.5	24.0
3Pd-*Si	30.0	0.2	1.8	0.7	9.8	2.8	n/a[d]
3Pd-22Si	30.0	1.4[c]	1.8	10.8	1.1	2.7	43.3
4Pd-22Si	120.0	1.4[c]	7.1	10.8	3.6	4.0	44.6

[a] Measured by EDS. [b] Measured by TEM. [c] Additional 1.2 mmol TTAB added into Pd-NP solution prior to pH adjustment by NaOH. [d] Shell size measurement not available.

The Pd-NP size modification was studied and compared by varying the Pd precursor concentrations prior to reduction by hydrazine. Subsequently, the shell thickness modification was studied by varying the amount of SiO_2 precursor, as well as Pd-NP concentration. The synthesis conditions and parameters are listed in Table 2.1. The prepared catalysts were dried at 60 °C in the oven and were sieved to 60-80 mesh. To remove residual organic contaminants, the sieved catalysts were further calcined in a muffle furnace under the static atmosphere with a heating rate at 2 °C/min up to 500 °C. After holding at 500 °C for 2 h, the catalysts were cooled to room temperature prior to activity tests and characterizations. To test high temperature stability, the catalysts were further heated to 800 °C or 850 °C at 2 °C/min and were kept at the elevated temperature for 4 h.

To compare the core@shell catalyst with a conventionally supported catalyst, a SiO_2 supported Pd catalyst (3.6 wt.% Pd/SiO_2) was prepared by impregnating silica with $Pd(NO_3)_2{\cdot}2H_2O$. To prepare the supported catalyst, 32 mg of $Pd(NO_3)_2{\cdot}2H_2O$ dissolved in 3 mL of de-ionized water was added to 300 mg of stabilized SiO_2 powder (60-80 mesh) just enough to fully submerge the silica powder. The slurry was dried at room temperature overnight followed by drying at 60 °C for 24 hours. The dried powder was calcined at 500 °C for 2 h and further aged at 800 °C or 850 °C for 4 h in air.

Characterization of Pd@SiO_2 catalysts

A Genesys 10s UV-Vis spectrometer was used to monitor Pd nanoparticle formation in the synthesis step 1. The formation of a Pd-surfactant complex was observed by the full spectrum scan and the kinetics of Pd reduction was monitored by a kinetics mode scan. In order to monitor

the nanoparticle formation, UV-Vis scans from λ = 190 nm to 1100 nm were obtained at different stages of the Pd-NP formation. The kinetic study was carried out by measuring the absorption at λ = 292 nm once per second for 35 seconds, until there was no further change of the intensity.

The particle morphology was examined by transmission electron microscopy (TEM). A JEOL-2010F TEM operating at 200 kV was used for all images presented, except Figure 2.17, where JEOL-3100 TEM was used at 300 kV for high resolution analysis. For TEM analysis, the catalyst was loaded onto a 200-mesh copper grid with carbon film support. A typical TEM specimen was prepared by dispersing washed Pd@SiO_2 nanopowders in ethanol by sonication for 30 minutes. The suspended nanoparticles were supported on a 200-mesh copper grid with carbon film support. TEM specimens for SiO_2 deposition mechanism study was not sonicated or washed in order to avoid disrupting underdeveloped structures. All size distributions of core and shell diameters were measured by TEM, using Image J software. Each diameter was calculated by the following area mean equation ($\sum(n_i \times d_i)^3 / \sum(n_i \times d_i)^2$) over the measured value of 250 or more particles. The sample elemental composition was measured by low-powered energy-dispersive spectroscopy (EDS) in a Phillips XL30FEG scanning electron microscope. To obtain the bulk composition, approximately 0.1g of the finely ground catalyst was analyzed under EDS at 60x magnification and 30 keV at 5 different locations. The crystallography of the Pd@SiO_2 nanoparticle catalysts was measured with a Rigaku Rotating Anode X-ray powder diffractometer working at 20 mA and 40 kV. Each sample was scanned from 10 ^{o} to 90 ^{o} at 0.01 ^{o}/step with 1 ^{o}/min scanning speed.

The BET specific surface area, pore volume, and pore size distribution of Pd@SiO_2 catalysts were characterized by nitrogen physisorption at 77 K, using a Micromeritics ASAP

2020 instrument. All samples were degassed under vacuum at 350 ^{o}C overnight (at least 12 h) prior to analysis. The features for pore size in the mesoporous range were analyzed by Barrett-Joyner-Halenda (BJH) method. Thermogravimetric analysis coupled with infrared spectroscopy (TGA-IR) was carried out to analyze the decomposition of residual surfactant. About 10 mg of 3Pd-12Si powder, which was washed three times with DI water and six times with dry ethanol, was placed into the TGA sample pan under a 100 ml/min flow of 10 % O_2 in balance N_2. The temperature was stabilized at 50 °C for 2h prior to ramping to 700 °C at 10 °C/min. The effluent gas was analyzed during the entire run by a Nicolet 380 FTIR located downstream of the TGA instrument.

CO oxidation reaction

CO oxidation was carried out with 60 mg of 60-80 mesh catalyst powder mixed with 140 mg 60-80 mesh SiO_2 powder, as a diluting material. The mixture was held in a vertical quartz reactor (inner diameter: 2 mm) by quartz wool plugs placed on the top and bottom of the catalyst bed. The reaction was carried out in flowing the reactant gases (1 % CO + 1.5 % O_2 in balance N_2) at a total flowrate of 200 ml/min for 30 minutes prior to ramping the temperature from 50 °C to 500 °C at a rate of 2 °C per minute (GSHV = 200,000 ml/g h^{-1}).

Results and discussion

Synthesis method validation

The general one-pot synthesis procedures follow Figure 2.1. Various synthesis protocols including using different Pd^{2+} precursors and surfactants were investigated. First, K_2PdCl_4 was used as Pd^{2+} precursor with TTAB as surfactant under the same conditions as the conditions used

for the synthesis of 3Pd-12Si (Table 2.1). As reported previously [14], under such synthesis conditions with K_2PdCl_4 and TTAB, $Pd@SiO_2$ catalysts can be synthesized successfully. When the Pd precursor was replaced by $Pd(NO_3)_2 \times 2H_2O$, no significant difference in $Pd@SiO_2$ structure was observed. Therefore, to avoid potential poisoning, [23, 24] as well as complex formation [25-27] by chlorine derived from K_2PdCl_4 precursor, $Pd(NO_3)_2 \times 2H_2O$ was used instead of K_2PdCl_4 to investigate the synthesis mechanism and the effect of synthesis parameters in the present work.

Figure 2.2 shows TEM images of the $Pd@SiO_2$ particles (3Pd-12Si). A very high fraction of particles possesses core@shell structures (Figure 2.2a). Pd-NPs with higher electron density appear as darker spots at the center of spherical SiO_2 shells (Figure 2.2b). The rough surface morphology of the silica shell indicates that the shell is mesoporous (Figure 2.3) [9, 10, 14],. Further analysis (Figure 2.2c) indicates a narrow core size distribution, with the average Pd cores of 2.7 nm in diameter, suggesting that the synthesis provides a highly dispersed active surface area of the metal.

To the best of our knowledge, two-step syntheses of core@shell catalysts for various precious metal cores including platinum [10] and gold [20] does not achieve such small core sizes. The main reason for such inability to achieve small metal cores in the two-step synthesis method is the difficulty of separating and re-dispersing very small metal nanoparticles (below 10 nm in diameter) while maintaining the size during the process. Lastly, our synthesis method also provides well defined SiO_2 shells (Figure 2.2d) with average diameters of 24.9 nm. The synthesis scale-up was also carried out by simply increasing the synthesis variables by three-fold in one batch, producing ~ 0.5 g of catalyst. No apparent morphology difference was observed between

the catalysts from a smaller and a larger batch, indicating that the synthesis can be reproduced and scaled up.

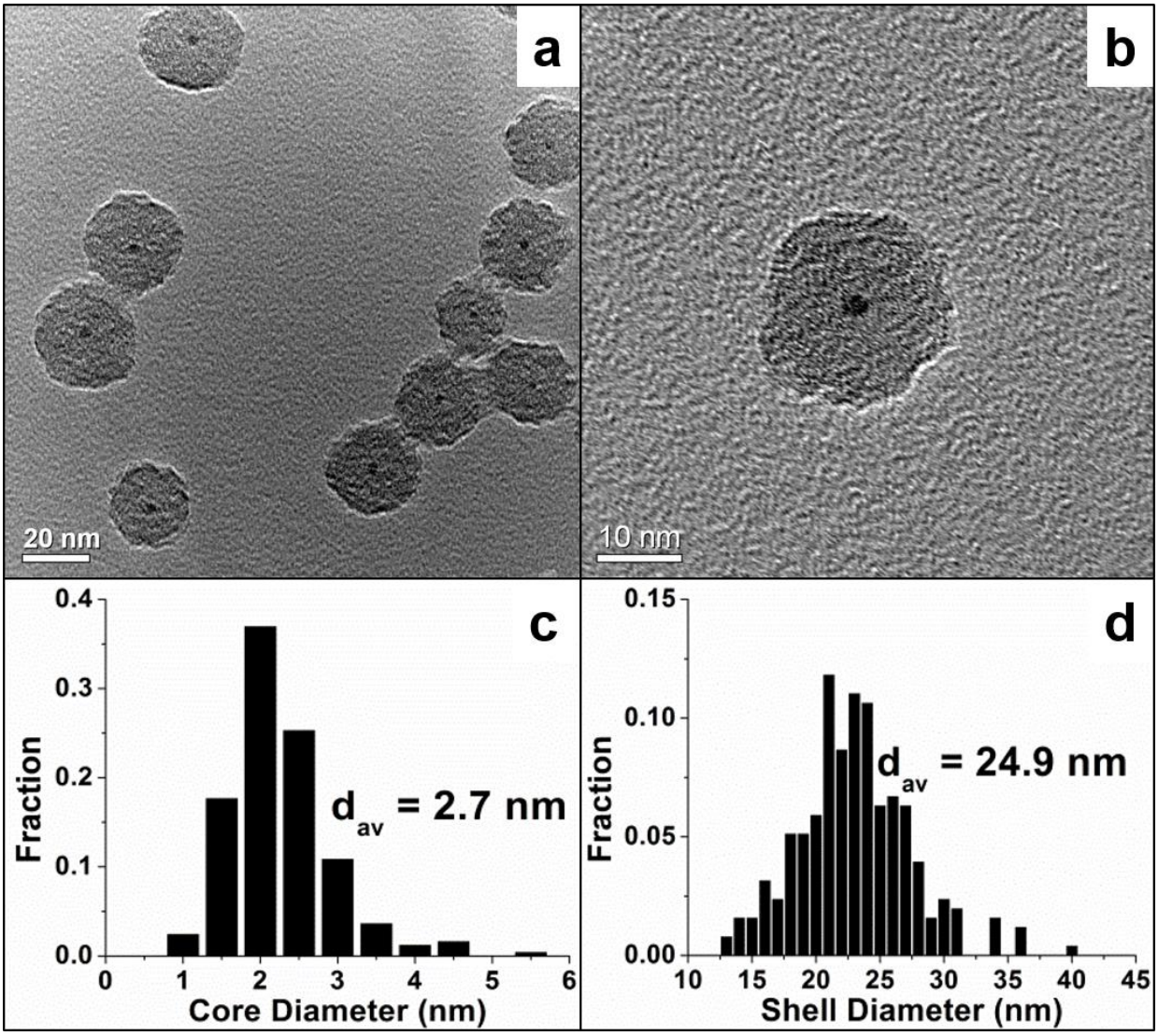

Figure 2.2 TEM micrographs of Pd@SiO_2 (3Pd-12Si) representing (a) overall morphologies (b) individual particles at higher magnification, (c) and core and (d) shell size distributions counted using the equation $d_{avg}=\sum(ni\cdot di)^3/\sum(ni\cdot di)^2$ (over 250 particles).

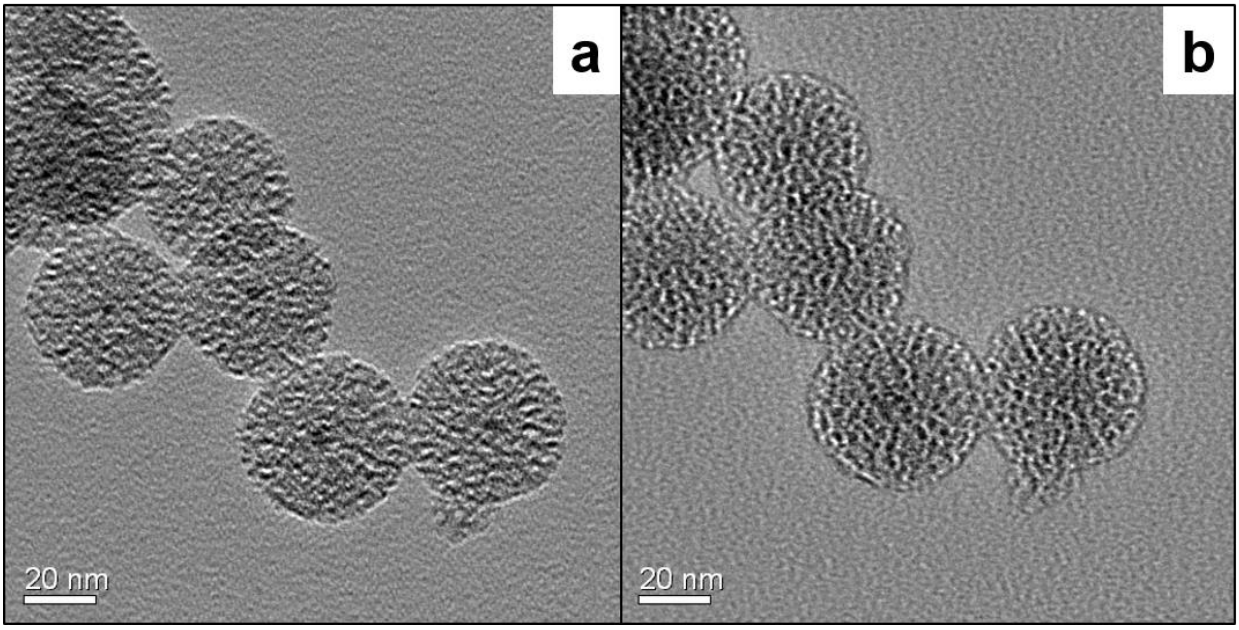

Figure 2.3 TEM analysis of the SiO_2 shell mesoporosity by obtaining the image (a) in focus and (b) out of focus. The rough morphology is a characteristic of mesoporosity.

Palladium core size control

The synthesis method described above allowed us to prepare Pd@SiO_2 nanoparticles in two steps: 1) Pd-NP preparation by reducing Pd^{2+} in the complex of Pd^{2+}-surfactant micelles independent of the SiO_2 shell deposition, and 2) encapsulation by SiO_2 shells through TEOS hydrolysis in the same pot. Each step was studied separately to explore the tunability of the core and the shell. To better control the Pd core size, three stages of Pd-NP formation in the aqueous solution were examined in detail by UV-Vis. Figure 2.4 shows different absorption features of the three aqueous solutions containing Pd^{2+}, Pd^{2+}-surfactant, and the reduced Pd-NP, which represent critical stages of the Pd core formation for a typical sample, 3Pd-12Si. The UV-Vis analysis results were similar with the findings of Veisz and Király [28] in that Pd^{2+} instantly forms a complex with Br^- from the surfactant, indicated by a color change of the Pd^{2+} solution from pale yellow to strong orange (Figure 2.4a). Reduction of the Pd^{2+} to Pd^0 was carried out by addition of hydrazine, which immediately turns the solution color from orange to black. Since

the complete reduction is important, the kinetics of Pd^{2+} to Pd^{0} reduction was also monitored by observing the UV-Vis peak extinction at 292 nm. The complete reduction of Pd^{2+} occurred within 30 sec after hydrazine addition (Figure 2.4b), indicating fast reduction, which could produce small NPs.

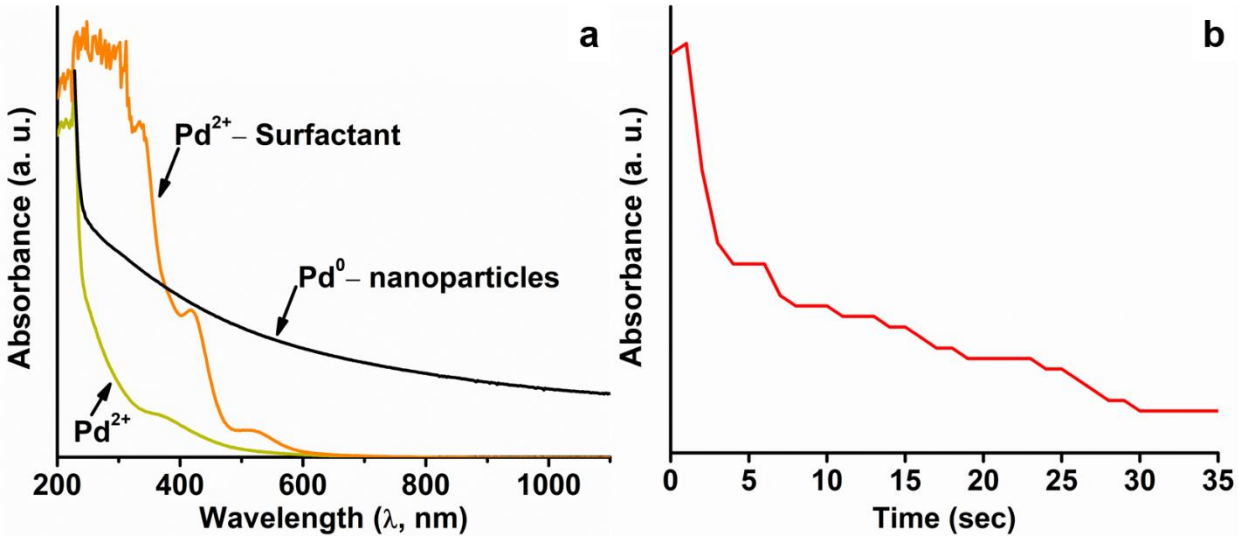

Figure 2.4 UV-Vis spectra during different states of Pd core nanoparticle formation in the step 1 of $Pd@SiO_2$ synthesis.

The stability of the as prepared Pd-NP, necessary for the synthesis of $Pd@SiO_2$ before hydrolysis of TEOS, can be obtained by pH adjustment of the prepared Pd-NP suspension. During formation of Pd-NPs, hydrazine served both as a reductant as well as a weak base that stabilizes the surfactant on the Pd-NP surface to form double-walled micelles [29-31]. As hydrazine decomposes over time, the pH of the solution drops from 9.5 to 3.4 (Figure 2.5). On acidification, the surfactant molecules no longer prevent Pd nanoparticles from agglomerating and Pd-NPs precipitate within one hour. This phenomenon was not reported by Veisz and Király with K_2PdCl_4 as the precursor [28]. Therefore, the agglomeration may be attributed to the higher acidity of $Pd(NO_3)_2{\times}2H_2O$, since the final solution of $Pd(NO_3)_2{\times}2H_2O$ used in our method has a lower pH than the solution of K_2PdCl_4 used by Veisz and Király [28]. The agglomeration of Pd

cores can be prevented by raising the pH of the Pd-NP suspension by adding a base. However, it should be noted that instant agglomeration and precipitation of Pd-NPs occured on addition of ammonia as a base. This agglomeration, unidentical to the one caused by acidification, can be explained by replacement of the amine-based surfactant by ammonium ions which lack the long carbon chains that prevent nanoparticle agglomeration. Sodium hydroxide (NaOH) was finally found to be a better stabilizing base.

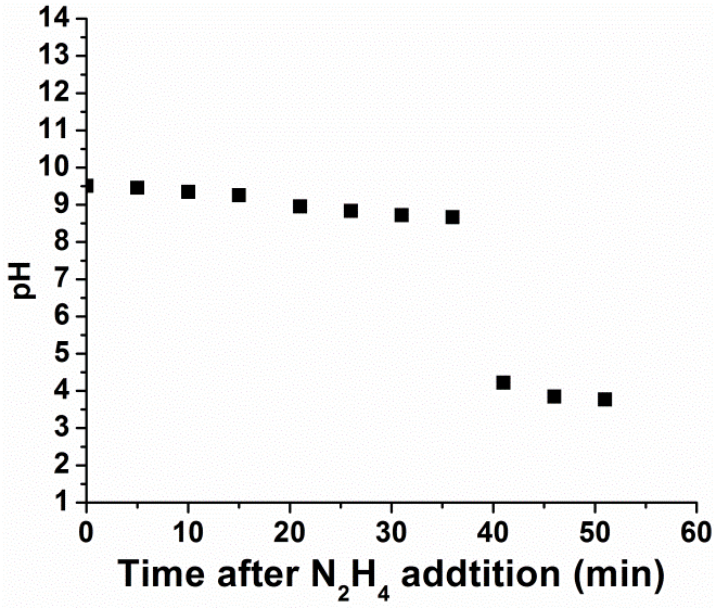

Figure 2.5 The pH of palladium nanoparticle solution was measured over time after hydrazine addition (t=0). The pH of the hydrazine solution was 9.5 and the pH of the palladium nitrate solution was 3.4, prior to mixing.

The study of Pd-NP size control in $Pd@SiO_2$ nanoparticles was investigated mainly by fixing the amounts of surfactant, TEOS, and Pd^{2+}:N_2H_4 ratios. The conditions and parameters are listed in Table 2.1 (samples 2Pd-16Si, 3Pd-12Si, and 4Pd-12Si). We found that the Pd core size is closely related to the Pd^{2+} concentration, i.e., D_{core} increases from 1.8 nm to 2.8 nm and then 3.5 nm when the Pd^{2+} concentration in the aqueous solution increased from 7.5 to 30 and then $120x10^{-3}$ mmol. Interestingly, when the amount of TEOS is fixed, the shell thickness decreased sharply as the core diameter increased. This indicates that the increased concentration of Pd^{2+} not

only generates larger size Pd-NP but also generates a larger number of Pd-NP, as expected. Consequently, a smaller amount of TEOS is available per Pd particle, which resulted in the formation of thinner shells. This could explain the non-linear relationship between the core size vs. the concentration of Pd^{2+}.

Another variable in determining the core size is the surfactant. Surfactant plays critical roles in the synthesis of core@shell structure: 1) the formation of Pd^{2+}-surfactant complexes protects the formed Pd^0 cores after reduction from agglomeration; 2) it serves as the structural templating agent (micelles) directing the formation of SiO_2 on Pd^0 surface through hydrolysis of TEOS.

Although the surfactant concentration determines the final core@shell morphology, as long as the concentration was kept above 10 mmol/L, adjusting the concentration of TTAB under the same Pd^{2+}concentration had a negligible influence on Pd-NP morphology (Figure 2.6a). When 5 mmol/L TTAB was used, elongated Pd nanoparticles were observed (Figure 2.6b) [32], although we expected the particle shape to remain stable while the TTAB concentration stayed above the critical micelle concentration (CMC, 3.8 mmol/L) [33]. This suggests that the NP formation and stabilization may not be totally dictated by the CMC, since a significant excess of surfactant above the CMC is required to prevent agglomeration. On another note, the formation of elongated nanoparticles suggests a possible route to Pd-NP morphology control by varying surfactant concentration. However, this study achieved Pd core size tuning mainly by changing Pd^{2+} concentrations.

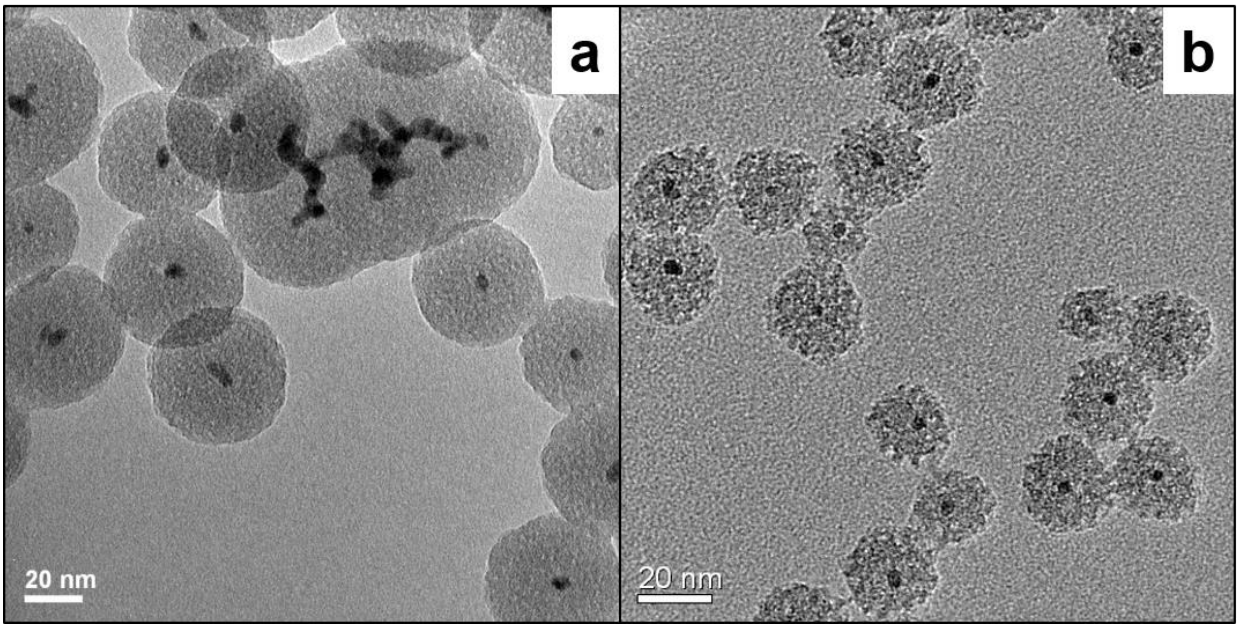

Figure 2.6. TEM images of 4Pd-12Si synthesized with TTAB concentrations of (a) 5 mmol/L and (b) 40 mmol/L.

Synthesis of tunable silica shell

To obtain insights into the mechanistic details of the SiO_2 shell formation, time-lapse TEM images were collected at different stages of shell formation (Figure 2.7). From the time-lapse study, we found that the silica shell formation occurs in three stages: Pd-NP capture, SiO_2 condensation, and separation. During the first stage, which happens instantaneously after TEOS addition, Pd-NPs (Figure 2.7a) are immobilized on the surface of micron-sized TEOS droplets that are suspended in water (Figure 2.7b). This observation contrasts with a commonly described mechanism [11, 34], where dissolved TEOS deposits onto the Pd surface over time.

Instead, our observation suggests that Pd nanoparticles instantaneously attach onto much larger TEOS droplet surfaces, acting as the source of the SiO_2 shell over many Pd cores. The immediate capturing can be explained by the interaction between the surfactant, which stabilizes the Pd-NPs, and TEOS. It is thought that cationic surfactants, e. g. TTAB, form double-walled micelles to stabilize metal nanoparticles. During core@shell formation, the surfactant is attracted

immediately to the TEOS droplet surface, on introduction of TEOS into water. However, the surfactant in this case would contain Pd-NPs within its double-walled micelles, naturally bringing the Pd-NP to the TEOS surface. Such delivery induces immediate encapsulation of Pd-NPs by TEOS as shown in Figure 2.7. Once the Pd-NPs are captured by TEOS, silica starts to form by base-catalyzed hydrolysis on the surfactant that contain the Pd-NP (Figure 2.7c). Over time, the Pd-NPs encapsulated by silica particles undergo self-reorganization to form bigger micelles consisting of Pd-silica-TTAB, which separate from micron-sized TEOS droplet (Figure 2.7d). Finally, distinguishable core@shell particles form after 10 h (Figure 2.7e). We found that the particle morphology remains stable under the synthesis condition for 72 h under stirring (Figure 2.7f), demonstrating that the core@shell structure is thermodynamically stable under the synthesis conditions.

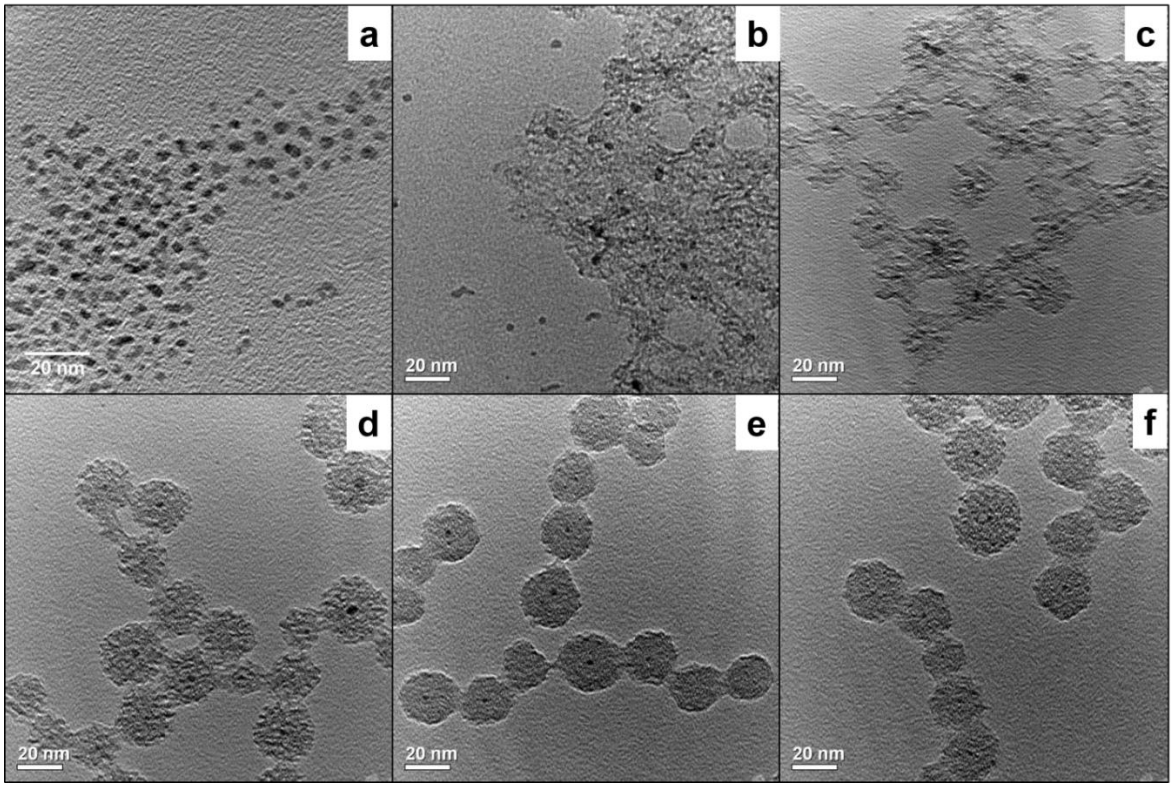

Figure 2.7 TEM images for time-lapse monitoring of SiO_2 shell formation on 3Pd-12Si samples at different stages of the synthesis. a) Pd nanoparticles prior to TEOS addition; b) immediately after TEOS addition; c) 1 h, d) 4 h, e) 10 h, and f) 72 h after TEOS addition.

The efforts to compare the effect of synthesis parameters on shell formation were made by changing the amount of TEOS added to the Pd-NP suspension (see Table 2.2). As the amount of added TEOS decreases, there exists a minimum shell thickness required for the formation of isolated Pd@SiO_2 particles, as indicated by 3Pd-*Si in Table 2.2 and the TEM image shown in Figure 2.8b. When a smaller amount of TEOS than required for the minimum shell thickness formation is provided, shell formation stops at the 2nd (condensation) stage without proceeding to the final (separation) stage, in which dispersible Pd@SiO_2 particles form. Further decreasing the amount of TEOS resulted in surface deposition of Pd-NPs on the surface of a chain-like Pd-embedded SiO_2 structure (Figure 2.9a).

It was suspected that the formation of such interconnected core@shell structures was caused by the overlap of the non-polar surfactant chains. As we have discussed earlier, TEOS hydrolyzes to form silica via slow sol-gel condensation around the hydrophobic surfactant carbon chains [35]. Given smaller amounts of TEOS, the "mother" droplet will become smaller, making the surfactant micelles overlap with one another. Therefore, silica condensation occurs along the overlapped micellular regions, resulting in chain-like morphologies. This hypothesis was tested by replacing TTAB with CTAB, which has 16 carbons as its hydrophobic tail, to increase surfactant overlap. After surfactant substitution, core@shell chains with a higher degree of connectivity formed (Figure 2.9b) even for the same synthesis conditions as for 3Pd-12Si. This supports our hypothesis that the surfactant overlap is closely related to the separation of Pd@SiO_2 nanoparticles.

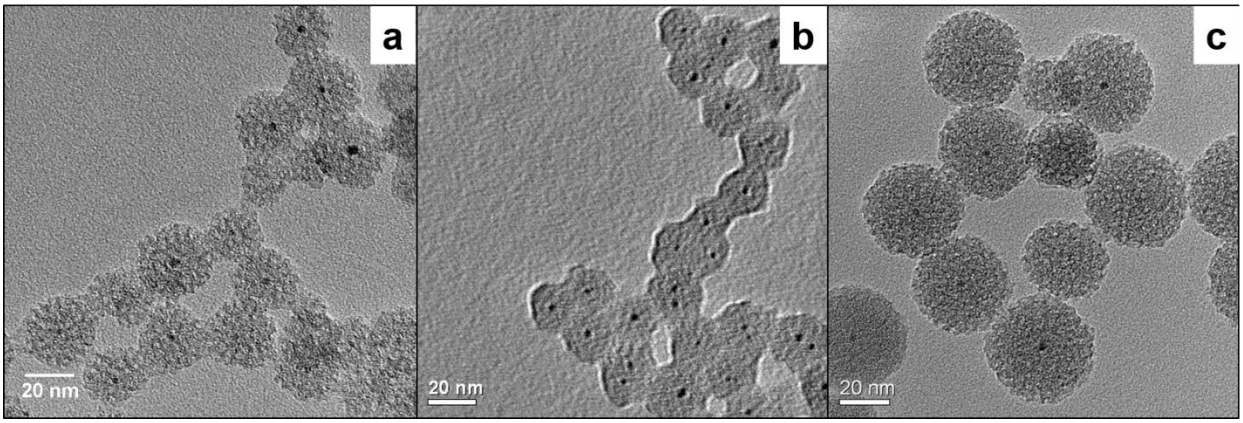

Figure 2.8 TEM images of samples synthesized by addition of different amounts of TEOS. (a) 3Pd-12Si; (b) 3Pd-*Si; (c) 3Pd-22Si.

Table 2.2 Particle size, BET specific surface areas, and pore features after catalyst aging at different temperatures.

Sample / Aging T (°C) / Duration (h)	D_{core}[a] (nm)	D_{shell}[a] (nm)	Surface area (m^2/g)	Pore size[b] (nm)
3Pd-12Si /500/2	2.8	24.9	519	1
3Pd-12Si /800/4	4.5	24.5	96	-
3Pd-12Si /850/4	4.4	24.3	94	-
4Pd-22Si /500/2	4.4	45.3	1165	2
4Pd-22Si /800/4	4.5	45.3	851	1
4Pd-22Si /850/4	4.5	44.5	690	-

[a] Measured by TEM [b] Measured by BJH method from N_2 desorption branch.

To further control the silica shell thicknesses, an increased amount of TEOS (10.8 mmol) was added to the palladium suspension to produce thicker shells. Interestingly, this resulted in core@shell particles that were merged with one another (Figure 2.9c). Since the morphology of these particles was different from the chain-like structures formed when insufficient TEOS was added, we hypothesized that the particles cannot form independent micelles and may not have sufficient space to grow the SiO_2 shell. To test this hypothesis, we decreased the number density of Pd-NP by diluting the Pd-TTAB suspension with water prior to TEOS (10.8 mmol) addition. Such modification caused formation of thicker shells (Figure 2.9d), but with multi-cores within one shell. This indicated that the surfactant does not prevent Pd-NPs agglomeration. Diluting by

de-ionized water below the CMC of TTAB (1.6 mmol/L) did not cause precipitation of Pd-NP. Instead, the number of Pd cores per core@shell particle increased, accompanied by an increase in shell thickness.

Successful thick shell deposition could be achieved (Figure 2.8c) after diluting the Pd-NP suspension with 10 mmol/L TTAB solution (see samples 3Pd-12Si vs 3Pd-22Si and 4Pd-12Si vs 4Pd-22Si in Table 2.2). This modification allows the formation of Pd-silica-TTAB micelles and provides enough growth space for the synthesis of thicker silica shells while preventing Pd-NP from agglomerating to form multi-cores per shell. Based on this detailed study, the SiO_2 shell formation mechanism and its governing parameters can be inferred. A graphical formation mechanism for this one pot synthesis is presented in Figure 2.10.

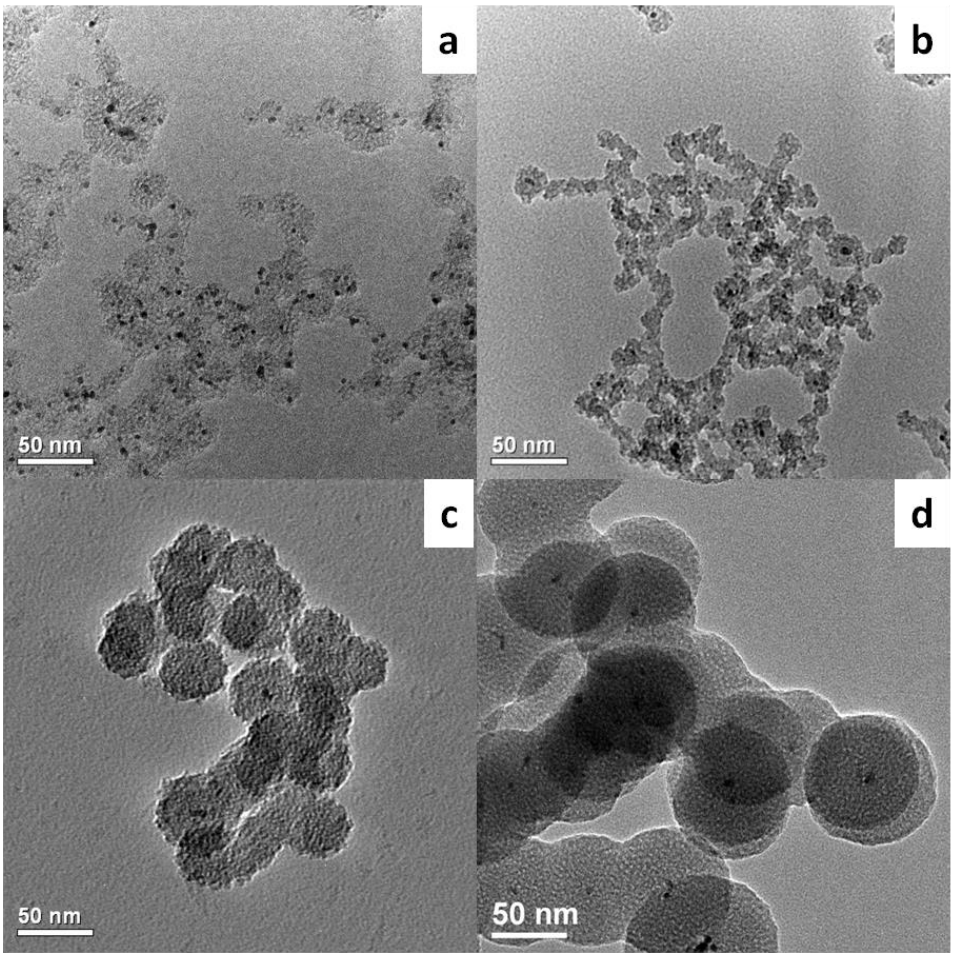

Figure 2.9 TEM images of attempts to synthesize 3Pd-12Si samples by (a) addition of 0.3 mmol TEOS, or (b) 2.7 mmol TEOS but useing CTAB, and by (c) addition of 0.2 mmol TTAB or (d) 0.2 mmol of TTAB but diluting with water only prior to addition of 10.8 mmol TEOS.

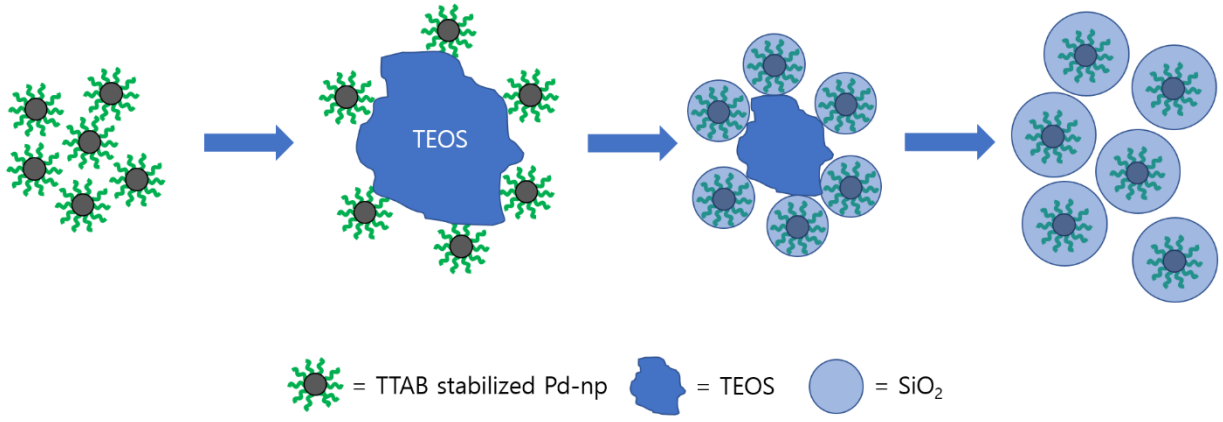

Figure 2.10. Schematic mechanism for the formation of Pd@SiO_2 particles via two steps in one pot synthesis.

Thermal stability of the Pd@SiO_2 nanoparticles

The thermal stability of a catalyst is very important to its utility and is often closely related with reliable catalytic performance over the lifetime of a catalyst. Exposure to high temperatures can induce the active metal to sinter to form larger aggregates, which diminish the available active sites for reaction, causing the catalyst to deactivate. Therefore, there have been multiple studies to understand the sintering mechanism with different explanations (particle migration [36, 37], Ostwald ripening [38, 39], or a combination of both [40]). One agreement with previous studies is that more severe sintering occurs with metallic Pd than its oxide, PdO. Unfortunately, PdO can thermally decomposition to metallic Pd at ca 800 °C, even under oxygen-rich conditions [41]. Therefore, Pd sintering is very severe at temperatures above 800 °C [5].

A significant continuing effort is to improve the thermal stability of Pd catalysts at elevated temperatures. One method used to achieve better thermal stability is to use core@shell structures. However, not many reported studies fully explore the benefits of core@shell structures at temperatures above 800 °C. Recently, Pi et al. investigated the activity and thermal stability of Pd@SiO_2 supported on Si-modified Al_2O_3 for methane oxidation at 800 °C [42]. Their Pd@Al_2O_3-SiO_2 catalyst demonstrated improved thermal stability, compared to a supported Pd/Si-Al_2O_3 catalyst. Park et al. also reported highly active and sinter-resistant Pd encapsulated in silica catalysts at 700 °C [9]. However, 700 °C calcination in air may not cause sintering of supported Pd catalysts. In contrast, it may be a temperature for oxidative Pd re-dispersion on alumina [5, 6]. In addition, not many reports mention the impact of initial Pd particle size, a crucial factor that determines the degree of thermal sintering [43]. Since our preparation method allows us to independently tune the core size and the shell size, we decided

to explore the thermal stability of our Pd@SiO_2 catalysts above the PdO decomposition temperature to gain deeper insight into the aging behavior of Pd encapsulated by SiO_2.

First, the thermal stability of two catalysts (3Pd-12Si and 4Pd-22Si) with a similar Pd loading (3.2 % vs. 3.6 %) with different core sizes and shell thicknesses was investigated: i.e. the 3Pd-12Si catalyst with the smaller Pd cores (d_{av} = 2.7 nm) and thinner SiO_2 shells (d_{av} = 24.9 nm) and the 4Pd-22Si catalyst with larger Pd cores (d_{av} = 4.0 nm) and thicker SiO_2 shells (d_{av} = 44.6 nm).

The thermal stability was characterized by the Pd particle sizes and silica shells' BET specific surface areas and mesopore sizes. Table 2.2 presents the results. It should be noted that prior to aging at high temperatures, all catalysts were calcined at 500 °C to remove the residual surfactants capped on and/or within Pd@SiO_2 (Figure 2.11). This calcination temperature (500 °C) in ambient atmosphere was determined based on the result of temperature programmed gravimetric analysis coupled with infrared analysis (TGA-IR) of evolved gases from TGA (Figure 2.12). To further test the thermal stability of the catalysts, the core@shell powders were then subjected to aging in air at 800 °C and 850 °C for 4 h, respectively. As mentioned above, these two temperatures were selected to investigate the aging behavior of Pd in different oxidation states. At 800 °C, bulk PdO starts to decompose to metallic Pd while at 850 °C surface-supported PdO decomposes into metallic Pd [41, 44]. Since it is suspected that metallic Pd is more prone to sintering [45], 850 °C, at which PdO decomposes to Pd, was an important temperature to test the thermal stability of the prepared Pd@SiO_2 catalysts.

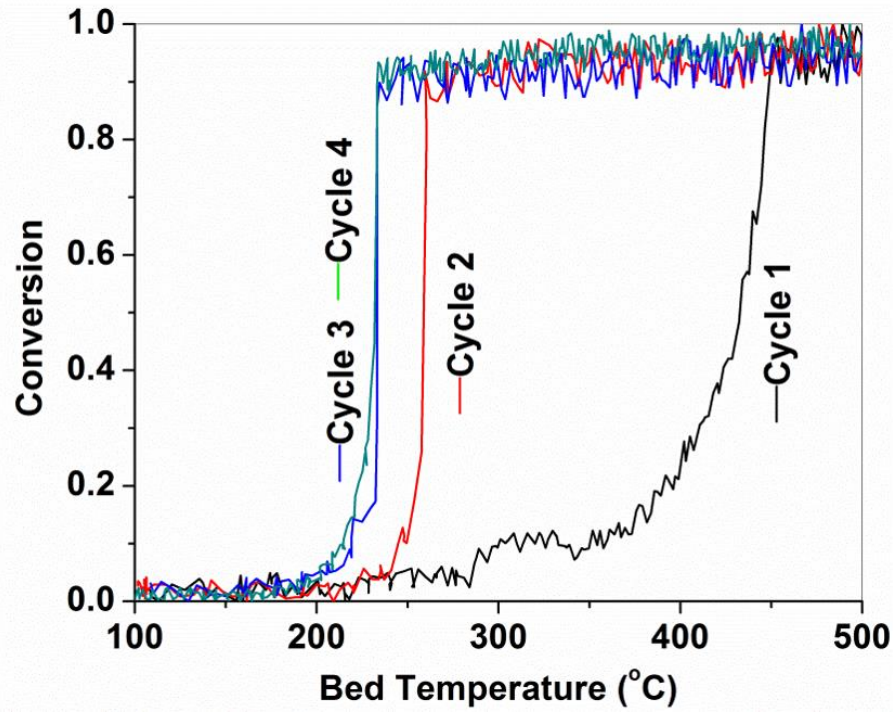

Figure 2.11 Cyclic CO oxidation over an uncalcined Pd@SiO_2 catalyst over 4 cycles during the oxidative removal of residual TTAB surfactant.

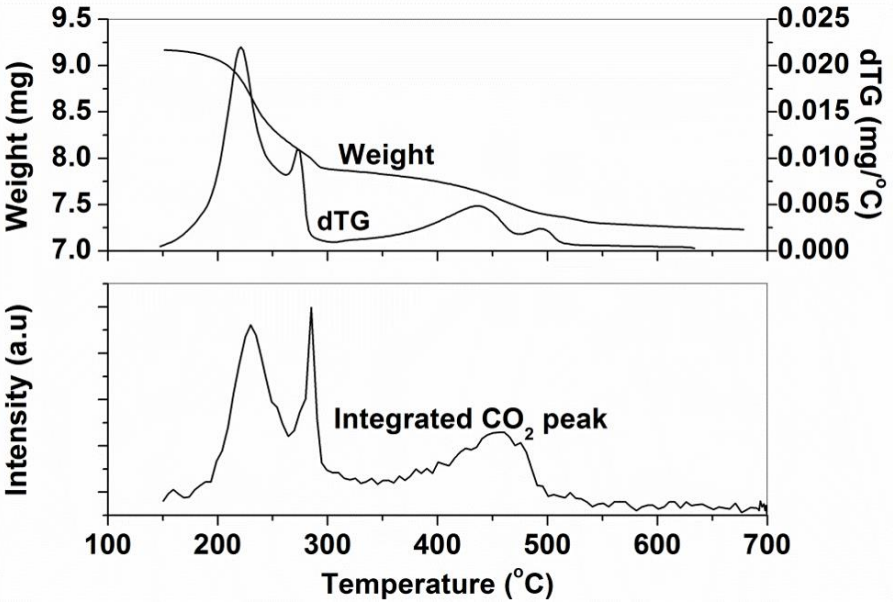

Figure 2.12 TG and DTG curves (a) of an uncalcined Pd@SiO_2 catalyst and (b) integrated CO_2 IR peak during operation of TGA.

TEM results of high temperature aging for both 3Pd-12Si and 4Pd-22Si samples are presented in Figure 2.13. As seen from the Figure 2.13, thermal treatment at 500 °C did not sinter Pd significantly, and most of the particles retain core@shell morphology (Figure 2.13I-a, I-b) for both 3Pd-12Si and 4Pd-22Si catalysts. TEM micrographs after high temperature aging indicate that, the catalyst with smaller particles demonstrates a much higher degree of metal sintering compared to the one with larger particles. For the catalyst with smaller core (3Pd-12Si), it is apparent the aging significantly increased the number of empty silica shells as shown in Figure 2.13II-a. An interesting observation was that there were some silica particles with a void in the middle, as indicated by white arrows in Figure 2.13II-a. It appears that some metal cores can completely vaporize/melt from their original location, leaving empty silica shells, as reported by a few others [10, 14, 21]. On the other hand, the catalyst with a larger core and a thicker shell (4Pd-22Si) demonstrated excellent thermal stability even aging at 850 °C, as presented in Figure 2.13I-b, II-b.

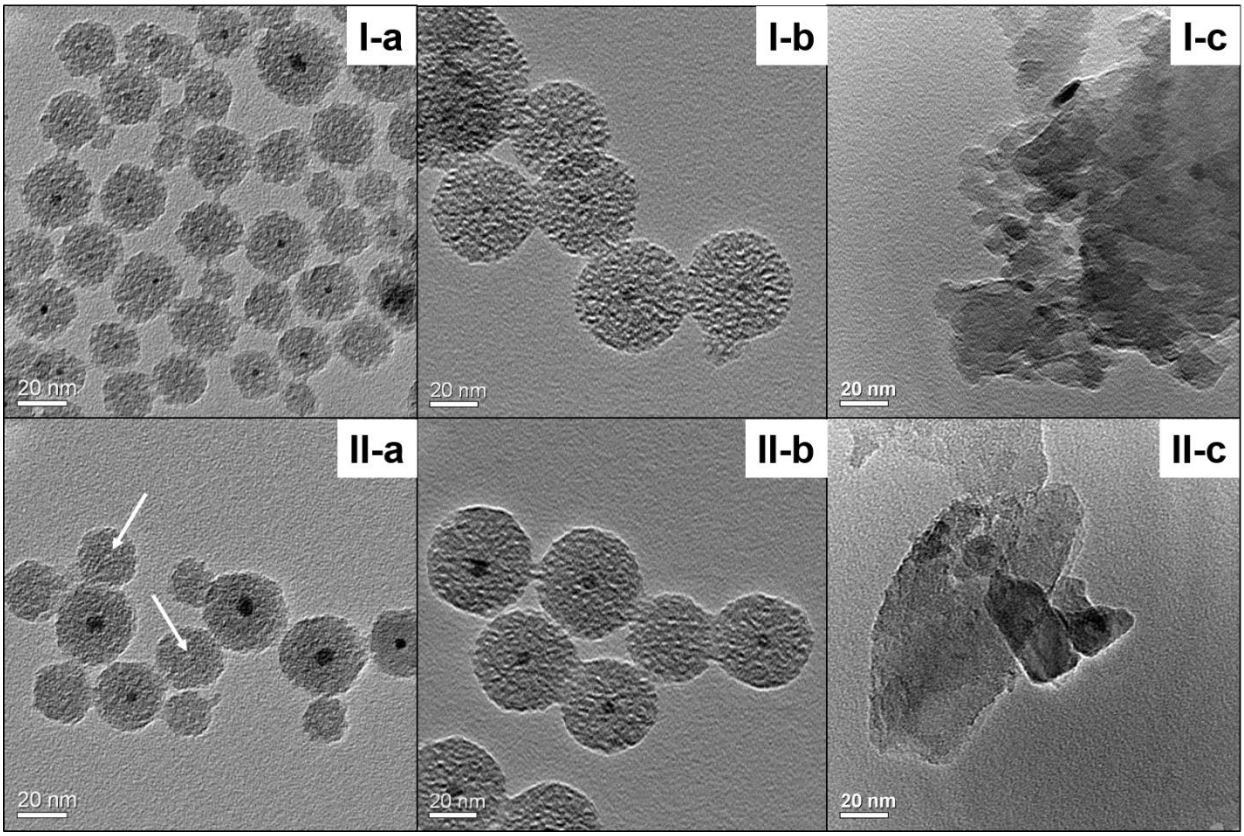

Figure 2.13 TEM micrographs after calcining at 500 °C (I) and aging at 850 °C (II) for (a) 3Pd-12Si and (b) 4Pd-22Si Pd@SiO_2 and (c) Pd/SiO_2 catalysts.

These results provide meaningful insights into the aging behavior of palladium catalysts. First, it supports a claim that an embedded Pd (or PdO) sinters via Ostwald ripening, instead of particle migration/coalescence. Since the pores in the shell are too small for the metal nanoparticles to migrate through, a more probable sintering mechanism is via vaporization of Pd atoms. Also, most of the observable Pd-NPs are located at the center of Pd@SiO_2 nanoparticles after aging. If Pd-NPs were migrating as observed in supported geometries, some of them must appear outside the shell and/or at an off-centered location. Since there were no significant sign of Pd metal outside the shell, it can be inferred that the sintering mainly occurred via atomic diffusion, also known as Ostwald ripening. Second, our observations provide information about size-dependent thermal stability of metal nanoparticles [40, 46, 47]. The size dependence is

demonstrated by comparing the aging behavior between 3Pd-12Si and 4Pd-22 Si. Because of the size dependence, the particle size change for the 4Pd-22Si catalyst, which has larger Pd cores, is minimal. On the other hand, 3Pd-12Si catalyst exhibited a notable size change as well as evolution of empty shells, signifying vaporization of Pd cores. The fact that the aging of 3Pd-12Si catalyst resulted in very similar Pd core size (4.4 nm) as the 4Pd-22Si (4.5 nm) after high temperature aging further supports the hypothesis of size dependent Pd aging. In addition to the TEM study, powder XRD provides further evidence of the thermal stability of core@shell catalysts (Figure 2.14). As seen, 3Pd-12Si shows a slight peak sharpening after 850 °C aging whereas 4Pd-22Si shows almost no peak sharpening, agreeing with the TEM results.

To compare the thermal aging behavior to a traditional supported catalyst, Pd supported on silica (Pd/SiO_2) of similar Pd loading (3.6wt. %) was prepared by impregnation. After aging at 800 °C, Pd/SiO_2 shows a significant peak sharpening compared to fresh catalyst (Figure 2.14a). An interesting observation was the appearance of a metallic Pd peak after 850 °C aging of Pd/SiO_2, indicating the formation and sintering of Pd through PdO decomposition. On the other hand, only PdO is observed for core@shell catalysts after 850 °C aging (Figure 2.14b, c). Such differences are good indications of thermal stability improvement by core@shell geometry, because Pd peak appears due to incomplete re-oxidation of Pd during cool down. During the aging, for the supported catalyst, the PdO decomposes to Pd and the Pd particles sintered too much to be re-oxidized during the course of furnace cooling in the ambient atmosphere [5]. On the other hand, core@shell catalysts kept the Pd size to be small enough for complete re-oxidation during the cool-down because of the confinement by the shell structure. It is also possible that the solid interaction between Pd and SiO_2, caused by close surface contact of the spherical Pd particles with the silica shells. As a result, the Pd particles, which remain smaller in

size, could re-oxidize while the catalyst cools down prior to removal from the furnace. Both the comparison of peak sharpening and the presence of a metallic Pd peak only for the supported catalyst emphasize that the core@shell catalyst is more resistant to sintering than a supported Pd catalyst.

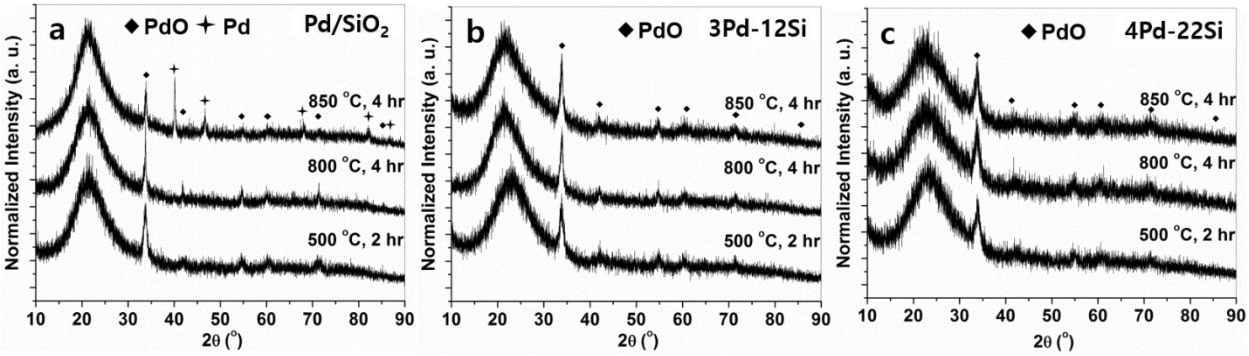

Figure 2.14 XRD patterns of Pd/SiO_2 (a), 3Pd-12Si (b) and 4Pd-22Si (c) catalysts after calcination followed by aging at 800 or 850 °C, respectively. PDF # 00-041-1107 and PDF # 98-002-0622 were used for the identification of PdO and Pd phases, respectively.

The changes in the silica shell after thermal treatment at different temperatures were analyzed by both TEM and nitrogen physisorption (Figure 2.15). TEM results (Figure 2.15, inset) indicate that the shell becomes denser and loses mesopores after aging, which agrees with the results of nitrogen physisorption. The BET surface areas also decreased significantly for both 3Pd-12Si and 4Pd-22Si after aging (Table 2.2). One interesting observation is that the surface area of prepared silica for 4Pd-22Si is much higher than the surface area of 3Pd-12Si (Table 2.2), despite the particle size of 3Pd-12Si being smaller than 4Pd-22Si. This suggests that the majority of surface area is contributed by the pore structure within the shell, as also suggested by no significant change in the shell diameter before and after aging.

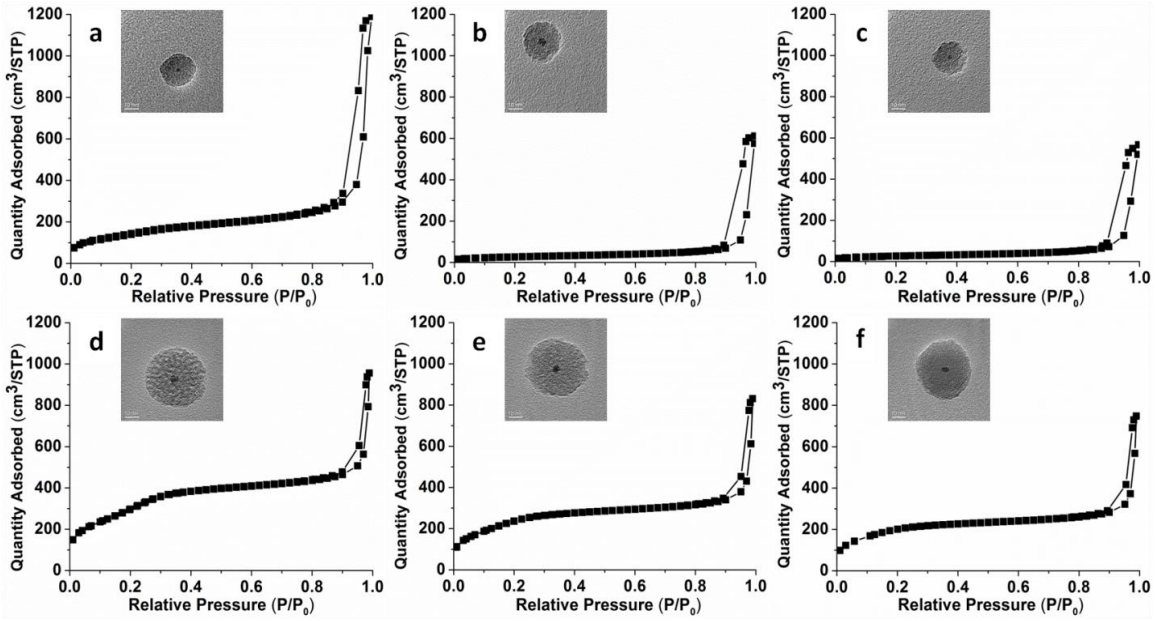

Figure 2.15 Nitrogen adsorption isotherm of Pd@SiO_2 with similar composition but different sizes (inset: TEM image of the catalyst). Top row: 3Pd-12Si calcined in air at (a) 500 ^oC 2 h, (b) 500 ^oC 2 h followed by 800 ^oC 4 h, (c) 500 ^oC 2 h followed by 850 ^oC 4 h; Bottom row: 4Pd-22Si calcined in air at (d) 500 ^oC 2 h, (e) 500 ^oC 2 h followed by 800 ^oC 4 h, (f) 500 ^oC 2 h followed by 850 ^oC 4 h.

Catalytic Activity Testing via CO-oxidation

To confirm the high temperature stability of Pd@SiO_2 catalysts, carbon monoxide (CO) oxidation was selected as a probe reaction, because the CO oxidation reaction is accepted as a structure-insensitive reaction on palladium surfaces [48, 49]. In other words, the CO conversion rate depends on the available Pd surface atoms (the size of Pd particles), given similar palladium loading. The results of CO oxidation (Figure 2.9) show lower light-off temperatures (T_{50}) on 3Pd-12Si than 4Pd-22Si, indicating smaller Pd sizes for 3Pd-12Si than 4Pd-22Si. This result validates our core size control during the synthesis. Another interesting observation was that the 3Pd-12Si catalyst displayed better CO oxidation performance after aging at temperatures above 800 °C than 4Pd-22Si, although XRD and TEM analysis (Figure 2.14 and Table 2.2) indicate slight sintering of Pd for 3Pd-12Si with no significant sintering of 4Pd-22Si. An even more surprising observation was the slight improvement in activity (T_{50} reduced by 15-25 °C), after

aging for both 3Pd-12Si and 4Pd-22Si. This observation was reproducible for two different samples of 3Pd-12Si and over three cycles of one sample. Such improvements in CO oxidation activity was in striking contrast with the aging behavior observed over the Pd/SiO_2 catalyst, which shows T_{50} increases by 23 °C (Figure 2.16) as expected for a precious metal catalyst [8].

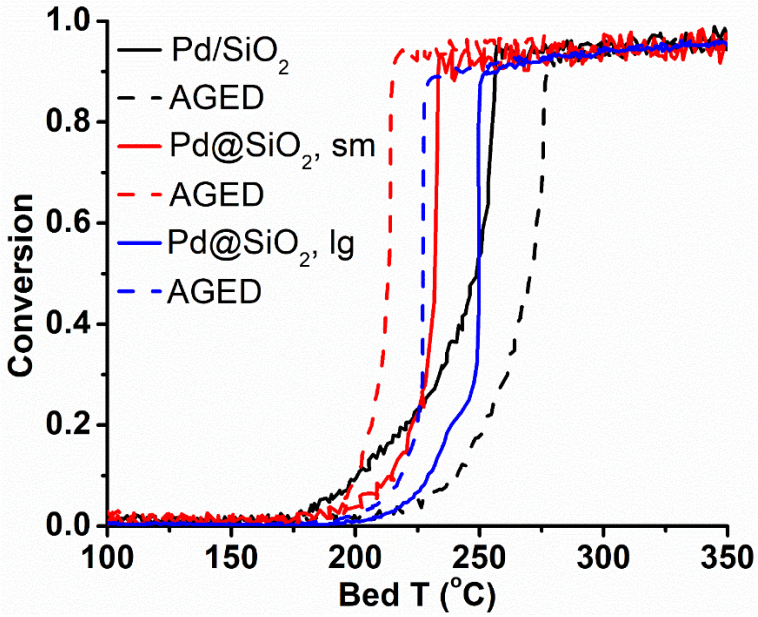

Figure 2.16 CO oxidation light-off curves over $Pd@SiO_2$ core@shell and Pd/SiO_2 supported catalysts after calcining at 500 °C for 2 h or calcining at 500 °C followed by aging at 850 °C for 4 h.

Confirming the deactivation of conventional catalyst after high temperature aging assured us that the enhanced CO oxidation activity expressed by our $Pd@SiO_2$ catalysts after aging is not an experimental artifact. This fact inspired us to find the underlying reason for the activity enhancement by in-depth study of the Pd behavior during aging at high and low temperatures. A few different hypotheses may explain such enhancement. The first is a local heat build-up at the Pd core induced by thermal silica-shell densification (hot-spot). Both nitrogen physisorption and TEM show that the pores shrink on exposure to high temperatures. After a certain point, it is possible that the pores have shrunk to such an extent that the shell begins to act as a thermal barrier that decreases the convective heat transfer from the catalyst to the bulk gas stream. This,

in turn, could lead to hot-spot formation in the Pd core, thereby raising the reaction rates. This hypothesis was ruled out, when we observed insignificant CO adsorption rate difference on the $Pd@SiO_2$ catalysts after aging at different temperatures. The second hypothesis was palladium redispersion in the lean environment as previously demonstrated at temperatures below PdO decomposition to Pd [5, 6]. Recently, Zhang et al. [50] found by *ex-situ* and *in-situ* TEM that $Pd@CeO_2$ catalysts can restructure during aging at 800 °C. Both larger and smaller Pd particles can simultaneously exist after aging.

To test the second hypothesis, we conducted a high-resolution dark field scanning transmission electron microscopy (DF-STEM) for 4Pd-22Si catalyst that had been aged at different temperatures. For as prepared samples, the Pd core is clearly represented in the middle and the mesopores of the SiO_2 shell are also observed (Figure 2.17a), as expected from our previous characterizations. No significant difference is observed after 500 °C calcination (Figure 2.17b), except a sign of decreased numbers of mesopores represented by less sponge-like shell morphology. At this stage, the Pd core is still located in the center and there is no sign of Pd re-dispersion. However, the morphology significantly changes after 800 °C aging (Figure 2.17c). Numerous Pd clusters with 0-2 nm diameter are observed within the pores of the SiO_2 shells, suggesting Pd re-dispersion by aging. Since 800 °C aged sample had already been calcined at 500 °C, we can conclude that the redispersion only occurs at higher temperatures. In comparison, no such Pd clusters are observed for the supported Pd/SiO_2 catalyst after high temperature aging.

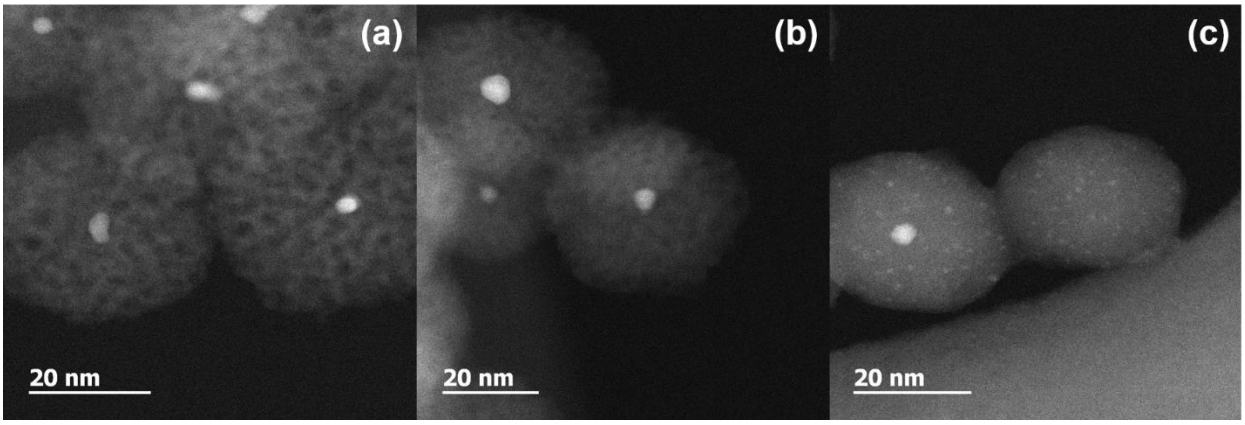

Figure 2.17 High resolution STEM study of Pd@SiO_2 aged at different temperatures. (a) no aging (b) 500 °C 2 h in air and (c) additional 800 °C 4 h in air from (b).

Based on the size difference between the core and the newly evolved Pd clusters, we can infer that the 0-2 nm Pd atom clusters originate from volatilized palladium atoms during the high temperature aging. Since we were not able to observe the atom clusters for the supported catalyst, the Pd redispersion can be attributed to the geometry of catalysts. For the Pd@SiO_2 catalyst, the palladium core is confined by the shell, which limits the growth of the palladium core over a certain size. Since the growth of the core is limited, the volatilized atomic palladium may re-disperse within nearby pores, increasing the overall CO oxidation activity. On the other hand, the supported catalyst is unconfined, allowing particle growth via particle migration as well as Ostwald ripening [38, 39, 43]. These TEM results, as shown in Figure 2.17, provide strong, direct evidence for Pd re-dispersion at high temperatures explaining the unusual CO oxidation activity enhancement for our Pd@SiO_2 catalysts, as shown in Figure 2.16. To the best of our knowledge, such re-dispersion of metal nanoparticle has not been very well investigated for other Pd@SiO_2 systems, possibly because the previous reports have not studied the thermal stability above 800 °C [42].

Conclusions

We have developed a facile one-pot synthesis method for $Pd@SiO_2$ (core@shell) particles under ambient aqueous conditions, which allows Pd nanoparticles smaller than 5 nm to be incorporated within mesoporous silica shells. We also succeeded in independently controlling the size of the core and the shell by modifying chemical parameters such as the palladium precursor concentration, Pd particle density, and the silica shell precursor concentration. Based on the synthesis result, a new $Pd@SiO_2$ formation mechanism has been proposed.

The thermal stability of resulting $Pd@SiO_2$ nanoparticles was studied by TEM, XRD, and CO oxidation. The result showed excellent thermal stability of the catalyst up to 850 °C. When the catalyst was aged above PdO decomposition temperature, improved CO oxidation activity was observed for the $Pd@SiO_2$ catalyst. On the other hand, Pd/SiO_2 deactivated by sintering after the same aging. To explain this difference, DF-STEM was used to investigate Pd redispersion. The DF-STEM provides a direct evidence for palladium metal re-dispersion inside the pores of SiO_2 shells which only occurred within core@shell particles at high temperatures.

Acknowledgements

Financial support for this work by the US Department of Energy under Cooperative Agreement No. DE-EE0006845, Subcontract agreement No. RQ15-337R01 is gratefully acknowledged. The support of the University of Michigan College of Engineering and NSF grant #DMR-9871177 for the JEOL 2010F transmission electron microscope is also acknowledged. The discussion about TEM micrograph interpretations with Dr. Wei Liu is acknowledged.

References

[1] P. Gélin, M. Primet, Applied Catalysis B: Environmental 39 (2002) 1-37.

[2] D. Pakhare, J. Spivey, Chemical Society Reviews 43 (2014) 7813-7837.

[3] T. Pradeep, Anshup, Thin Solid Films 517 (2009) 6441-6478.

[4] J. Wang, H. Chen, Z. Hu, M. Yao, Y. Li, Catalysis Reviews 57 (2015) 79-144.

[5] X. Chen, Y. Cheng, C.Y. Seo, J.W. Schwank, R.W. McCabe, Applied Catalysis B: Environmental 163 (2015) 499-509.

[6] J.A. Lupescu, J.W. Schwank, K.A. Dahlberg, C.Y. Seo, G.B. Fisher, S.L. Peczonczyk, K. Rhodes, M.J. Jagner, L.P. Haack, Applied Catalysis B: Environmental 183 (2016) 343-360.

[7] R.M.J. Fiedorow, B.S. Chahar, S.E. Wanke, Journal of Catalysis 51 (1978) 193-202.

[8] J.R. González-Velasco, J.A. Botas, R. Ferret, M. Pilar González-Marcos, J.-L. Marc, M.A. Gutiérrez-Ortiz, Catalysis Today 59 (2000) 395-402.

[9] J.-N. Park, A.J. Forman, W. Tang, J. Cheng, Y.-S. Hu, H. Lin, E.W. McFarland, Small 4 (2008) 1694-1697.

[10] S.H. Joo, J.Y. Park, C.-K. Tsung, Y. Yamada, P. Yang, G.A. Somorjai, Nature Matererials 8 (2009) 126-131.

[11] J. Chen, R. Zhang, L. Han, B. Tu, D. Zhao, Nano Research 6 (2013) 871-879.

[12] H. Zhang, R. Jin, H. Yao, S. Tang, J. Zhuang, G. Liu, H. Li, Chemical Communications 48 (2012) 7874-7876.

[13] Y. Xu, J. Ma, Y. Xu, L. Xu, L. Xu, H. Li, H. Li, RSC Advances 3 (2013) 851-858.

[14] Y. Hu, K. Tao, C. Wu, C. Zhou, H. Yin, S. Zhou, The Journal of Physical Chemistry C 117 (2013) 8974-8982.

[15] F. Wei, C. Cao, Y. Sun, S. Yang, P. Huang, W. Song, ChemCatChem 7 (2015) 2475-2479.

[16] N. Almana, S.P. Phivilay, P. Laveille, M.N. Hedhili, P. Fornasiero, K. Takanabe, J.-M. Basset, Journal of Catalysis 340 (2016) 368-375.

[17] D. Zhang, X. Song, R. Zhang, M. Zhang, F. Liu, European Journal of Inorganic Chemistry 2005 (2005) 1643-1648.

[18] M. Cargnello, N.L. Wieder, T. Montini, R.J. Gorte, P. Fornasiero, Journal of the American Chemical Society 132 (2010) 1402-1409.

[19] K. Bakhmutsky, N.L. Wieder, M. Cargnello, B. Galloway, P. Fornasiero, R.J. Gorte, ChemSusChem 5 (2012) 140-148.

[20] I. Gorelikov, N. Matsuura, Nano Letters 8 (2008) 369-373.

[21] H. Peng, X. Zhang, L. Zhang, C. Rao, J. Lian, W. Liu, J. Ying, G. Zhang, Z. Wang, N. Zhang, X. Wang, ChemCatChem 9 (2017) 127-136.

[22] G. Li, Z. Tang, Nanoscale 6 (2014) 3995-4011.

[23] D. Roth, P. Gélin, M. Primet, E. Tena, Applied Catalysis A: General 203 (2000) 37-45.

[24] Q. Lin, Y. Ji, Z.-D. Jiang, W.-D. Xiao, Industrial & Engineering Chemistry Research 46 (2007) 7950-7954.

[25] C. Li , R. Sato, M. Kanehara, H. Zeng, Y. Bando, T. Teranishi, Angewandte Chemie 121 (2009) 7015-7019.

[26] J.M. Pettibone, J.W. Hudgens, The Journal of Physical Chemistry Letters 1 (2010) 2536-2540.

[27] B. Li, T. Gu, T. Ming, J. Wang, P. Wang, J. Wang, J.C. Yu, ACS Nano 8 (2014) 8152-8162.

[28] B. Veisz, Z. Király, Langmuir 19 (2003) 4817-4824.

[29] S. Gómez-Graña, F. Hubert, F. Testard, A. Guerrero-Martínez, I. Grillo, L.M. Liz-Marzán, O. Spalla, Langmuir 28 (2012) 1453-1459.

[30] B. Nikoobakht, M.A. El-Sayed, Langmuir 17 (2001) 6368-6374.

[31] S.K. Meena, M. Sulpizi, Langmuir 29 (2013) 14954-14961.

[32] E. Ramirez, S. Jansat, K. Philippot, P. Lecante, M. Gomez, A.M. Masdeu-Bultó, B. Chaudret, Journal of Organometallic Chemistry 689 (2004) 4601-4610.

[33] E. Fuguet, C. Ràfols, M. Rosés, E. Bosch, Analytica Chimica Acta 548 (2005) 95-100.

[34] J.-T. Song, X.-S. Zhang, M.-Y. Qin, Y.-D. Zhao, Dalton Transactions 44 (2015) 7752-7756.

[35] Q. He, X. Cui, F. Cui, L. Guo, J. Shi, Microporous and Mesoporous Materials 117 (2009) 609-616.

[36] R.J. Liu, P.A. Crozier, C.M. Smith, D.A. Hucul, J. Blackson, G. Salaita, Applied Catalysis A: General 282 (2005) 111-121.

[37] Z. Jin, D. Nackashi, W. Lu, C. Kittrell, J.M. Tour, Chemistry of Materials 22 (2010) 5695-5699.

[38] Q. Xu, K.C. Kharas, B.J. Croley, A.K. Datye, ChemCatChem 3 (2011) 1004-1014.

[39] T.W. Hansen, A.T. DeLaRiva, S.R. Challa, A.K. Datye, Accounts of Chemical Research 46 (2013) 1720-1730.

[40] A.K. Datye, Q. Xu, K.C. Kharas, J.M. McCarty, Catalysis Today 111 (2006) 59-67.

[41] X. Chen, J.W. Schwank, G.B. Fisher, Y. Cheng, M. Jagner, R.W. McCabe, M.B. Katz, G.W. Graham, X. Pan, Applied Catalysis A: General 475 (2014) 420-426.

[42] D. Pi, W.Z. Li, Q.Z. Lin, Q.F. Huang, H.Q. Hu, C.Y. Shao, Energy Technology 4 (2016) 943-949.

[43] S.B. Kang, J.B. Lim, D. Jo, I.-S. Nam, B.K. Cho, S.B. Hong, C.H. Kim, S.H. Oh, Chemical Engineering Journal 316 (2017) 631-644.

[44] M. Peuckert, The Journal of Physical Chemistry 89 (1985) 2481-2486.

[45] S.B. Kang, S.J. Han, S.B. Nam, I.-S. Nam, B.K. Cho, C.H. Kim, S.H. Oh, Topics in Catalysis 56 (2013) 298-305.

[46] C.T. Campbell, S.C. Parker, D.E. Starr, Science 298 (2002) 811-814.

[47] Y.-H. Chin, M. García-Diéguez, E. Iglesia, The Journal of Physical Chemistry C 120 (2016) 1446-1460.

[48] F. Gao, Y. Wang, Y. Cai, D.W. Goodman, The Journal of Physical Chemistry C 113 (2009) 174-181.

[49] M. Boudart, F. Rumpf, Reaction Kinetics and Catalysis Letters 35 (1987) 95-105.

[50] S. Zhang, C. Chen, M. Cargnello, P. Fornasiero, R.J. Gorte, G.W. Graham, X. Pan, Nature communications 6 (2015).

Chapter 3

Facile, one-pot synthesis of Pd@CeO_2 core@shell nanoparticles in aqueous environment by controlled hydrolysis of metal-organic cerium precursor

Introduction

Several research groups have recently reported significantly enhanced (photo)catalytic activities of noble metal (NM) particles encapsulated within CeO_2; core@shell geometries [1-4]. Various preparation methods were used to encapsulate Pd, Pt, Au, and Ag [2-7]. However, the reported methods of synthesizing NM@CeO_2 nanoparticles have drawbacks. For example, the method reported by Cargnello et al. [6] uses toxic organic solvents and highly moisture-sensitive precursors. Another approach [3, 7-9] uses auto-redox between the metal core and cerium oxide precursors producing irregularly shaped particles. Recently, localized CeO_2 precipitation around Au [2] and Pd [5] nanoparticles has been reported but requires preparation of cores and shells in separate reactors as they must be synthesized under different conditions.

We report here, a facile, one-pot synthesis of Pd@CeO_2 core@shell nanoparticles in aqueous media, overcoming the abovementioned shortcomings. The core@shell morphology is achieved by controlled hydrolysis of a metalloorganic compound, cerium(IV) atrane, a unique synthesis approach. So far, the use of cerium metal-organic compounds has been limited [10, 11,

12], due to their high moisture sensitivity. Here, this limitation is resolved by introducing a chelating agent, triethanolamine (TEA), to retard hydrolysis, resulting in self-assembly to Pd@CeO_2. The thermal stability of the resulting material is further enhanced by forming either a CeO_2-ZrO_2 solid-solution shell, or a SiO_2 secondary shell, in "one-pot."

Experimental

Preparation of Cerium(IV) isobutyrate (Ce-iso) and Zirconium(IV) isobutyrate (Zr-iso)

Cerium carbonate (46 g, 0.1 mole) was reacted with excess isobutyric acid (250 mL, 2.8 mole) and isobutyric anhydride (75 mL, 0.5 mole) in a 1 L flask equipped with a still head. The solution was heated at 120 °C for 10 h under N_2 flow with magnetic stirring until a transparent dark orange liquid was obtained. On cooling to room temperature, Ce-iso $\{Ce[O_2CCH(CH_3)_2]_4\}$ crystallized and was filtered and dried at room temperature without further purification. Ce-iso was stored for future use by preparing a 0.4 M ethanolic solution with triethanolamine (TEA) as a stabilizing agent at 1:3 (Ce:TEA) molar ratio to form cerium-atrane. Zr-iso $\{Zr[O_2CCH(CH_3)_2]_2(OH)_2\}$ was prepared as described elsewhere [13].

Preparation of Pd nanoparticles (Pd-NP) suspended in water

Aqueous colloidal palladium nanoparticles were prepared by modifying the method reported by Veisz and Kiraly [14]. In a typical synthesis, 20 ml aqueous solution of 0.007 g $Pd(NO_3)_2 \cdot 2H_2O$ was mixed with 20 mL aqueous solution of 0.07 g trimethyltetradecylammonium bromide (TTAB) under vigorous stirring. Upon addition, the color of the solution turned from pale yellow to orange-red. After vigorous stirring for 10 seconds, the Pd^{2+} was reduced by 0.1 mL hydrazine·hydrate to yield a transparent-black palladium

nanoparticle colloidal solution. The palladium colloid was stirred for the next 30 minutes to allow hydrazine decomposition.

Synthesis of palladium@ceria core@shell nanoparticels

In a typical synthesis, the pH of aqueous palladium nanoparticle colloidal solution was adjusted to 10.7 by adding 0.06 mols/L NaOH solution to the palladium nanoparticle solution. To the solution, 20 ml of the prepared 0.4 M Ce-atrane ethanolic solution was added dropwise, over 30 minutes, under stirring. The pH was re-adjusted to 10.7 after 2 hours by adding 0.06 mols/L NaOH solution. Then, the flask was capped and stirred overnight (longer than 8 hours).

Synthesis of palladium@ceria@silica nanoparticles

Silica double-shell was achieved by adding tetraorthosilicate (TEOS) as SiO_2 precursor to an already existing Pd@CeO_2 nanoparticle suspension. In a typical synthesis, 0.5 mL TEOS was added dropwise to already prepared Pd@CeO_2 suspension that was stirred over 8 hours. After the addition of TEOS, the flask was capped and stirred for another 8 hours to complete the hydrolysis of TEOS.

Synthesis of palladium@ceria-zirconia nanoparticles

Synthesis of the mixed shell was achieved by replacing a small portion of Ce-atrane by Zr-atrane. In a typical synthesis, 16 mL of 0.4 M Ce-atrane was mixed with 4 mL of 0.4 M Zr-atrane. Then, the mixed solution was added dropwise to a stirring Pd nanoparticle colloid, at pH 10.7, over 30 minutes. The pH was re-adjusted to 10.7 after 2 hours of stirring and the flask was capped and left to stir overnight.

Characterization

TEM sample was prepared by loading a drop of the dispersed nanoparticle onto a 200-mesh copper grid with carbon film support. Most of reported TEM images were obtained by

JEOL-2010 TEM operating at 200 kV with exception of Figure 3.1b, which was obtained using high resolution JEOL-3011 TEM operating at 300 kV. EDS mapping was obtained by JEOL-2100 TEM operating at 200 kV with high-angle annular dark field detector and EADX r-TEM detector. XRD characterization was carried out with a Rigaku Rotating Anode X-Ray Diffractometer with CuKα radiation from $2\theta = 20°$ to 90° at step size of 0.02°.

Nitogen physisorption was carried out to measure the porosity of prepared catalysts. Prior to physisorption analysis, all samples were pretreated at 120 °C for 8 hours under vacuum to remove adsorbed water as well as potential volatiles. Specific surface area (SSA) and porosity measurements were carried out with LN_2 at -196 °C using a Micromeritics ASAP 2020 sorption analyzer. The SSA was determined by the BET multipoint method. The meso-pore size distribution was calculated by the Barrett-Joyner-Halenda method. The micro-pore size distribution was calculated by Horvath-Kawazoe method at low P/P_0.

Catalytic activity measurement

Prior to the catalytic activity measurement, remaining organic molecules were thermally removed from the $Pd@CeO_2$ catalyst by calcining at 500 °C for 2 h. In a typical calcination process, the catalyst was placed on a quartz boat which was then placed within a muffle furnace under the ambient atmosphere. The furnace was heated to 500 °C from room temperature at 2 °C/min. After 2 h of calcination, the furnace was cooled to room temperature at ambient cooling rate. The catalytic activity measurement was carried out by loading 60 mg of the catalyst into a vertical quartz tube reactor. The reactant gas composed of 1% CO, 10% O_2, and balance N_2 introduced at 200 ml/min through the catalyst at 50 °C for 30 min to saturate the surface. After 30 min, the reactor was heated at 2 °C/min from 50 °C to 250 °C under the same reactant gas flow.

Results and discussion

Synthesis of Pd@CeO_2

This synthesis procedure follows scheme in Chapter 2 which provides independent control of the Pd core size and CeO_2 shell thickness. Therefore, the Pd core must be prepared prior to CeO_2 shell synthesis. Successful synthesis and TEM analysis of Pd cores is shown in Figure 3.1. Due to rapid chemical reduction, the size of Pd core was kept small ($D_{core,\ av}$ = 2.7 nm).

The synthesis of Pd@CeO_2 was achieved by directly adding ethanolic solution of Ce-iso to the Pd nanoparticle suspension. Figure 3.2 summarizes TEM, EDS, and XPS characterization results, demonstrating successful synthesis of Pd@CeO_2 nanoparticles ($D_{shell,\ av}$ = 24 nm). Here, no noticeable signs of scattered CeO_2 nanocrystals with missing cores were observed, indicating the high efficacy of obtaining core@shell morphologies (Figure 3.2a, b). Shells are CeO_2 nanocrystal (2-5 nm) aggregates, similar to those results obtained by others [3, 6]. Unlike in Pd@SiO_2, where the morphology could be easily confirmed by TEM image, the high electron density of CeO_2 makes TEM characterization challenging. Therefore, EDS mapping (Figure 3.2d) was used to further confirm placement of Pd-NPs within the CeO_2 shell. In addition, XPS shows no Pd signals whereas a physical mixture of Pd-NPs+CeO_2 at the same mass fraction does (Figure 3.2e, f). Since XPS is a surface ($\leq$ 5 nm) characterization technique, this comparison strongly indicates that the majority of Pd-NPs are encapsulated by CeO_2. The XPS result further supports high efficacy of this synthesis method, since it proves that most of Pd nanoparticles are encapsulated under CeO_2.

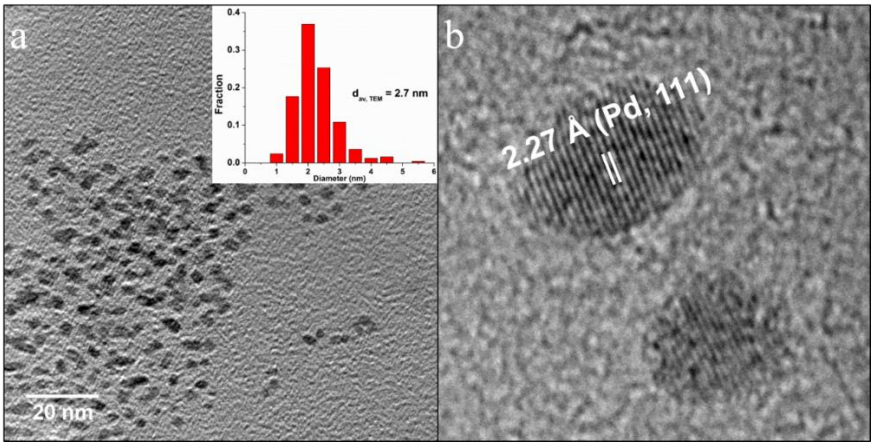

Figure 3.1 TEM characterization of Palladium nanoparticles (a) a low-resolution image (inset: size distribution obtained by counting 250 particles), and (b) a high-resolution image with Pd (111) lattice (ICSD ID: 648679).

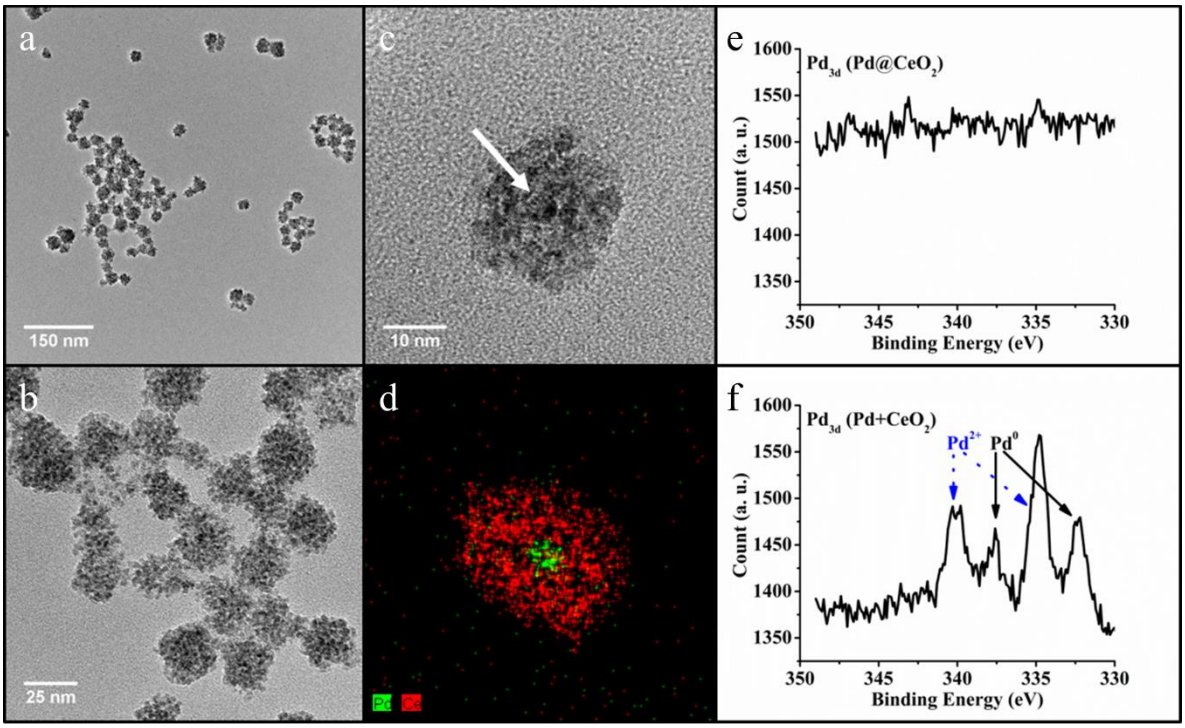

Figure 3.2 TEM images of Pd@CeO_2 core@shell structure at (a) low-magnification (b), (c) high-magnification (white arrow = Pd). (d) EDS map of Pd@CeO_2 (Green = Pd, Red = Ce). XPS signal of Pd for (e) Pd@CeO_2 and (f) Pd-NP/CeO_2 mixture.

Pd@CeO_2 as a catalyst

Since the primary application for the prepared material is in the field of catalysis, the accessibility of Pd core is very important. Therefore, further characterization was carried out by

N_2 physisorption, XRD, and CO oxidation. The isotherm result (Figure 3.3a) as well as the pore-size distribution indicate that the shell contains both micro- and meso-pores, as expected due to its aggregate nature. High specific surface areas of 202 ± 5 m^2/g were achieved, again agreeing with the aggregate nature of the CeO_2 shell. The broad peaks of the Pd@CeO_2 XRD patterns (Figure 3.3b) corroborate the formation of CeO_2 nanocrystals as observed by TEM. Peaks remained broad after 500 °C/2 h calcination in air, performed to remove residual TTAB, with minimal sharpening. Pd was not detected due to relatively small concentration (2 wt. % by EDS) and the small core sizes.

Finally, CO oxidation was performed to directly demonstrate the accessibility of reactant molecules through the pores. As seen in Figure 3.3c, full conversion was achieved at a relatively low temperature of 90 °C. Similar low-temperature CO oxidation activity was also observed by Cargnello et al. (T_{100} = 135 °C) [6] and Wang et al. (T_{100} = 95 °C) [3] using Pd@CeO_2 structures prepared via different methods. To emphasize the importance of the Pd-core accessibility, CO oxidation was measured with only CeO_2. As expected, the CeO_2 without Pd did not show activity up to 250 °C. This result demonstrates two advantages of our synthesis method. First, low light-off temperature means that the method offers high metal-support interaction between the core and shell. Second, the synthesis method yields a porous shell that is stable after 500 °C calcination, which is suitable for catalysis.

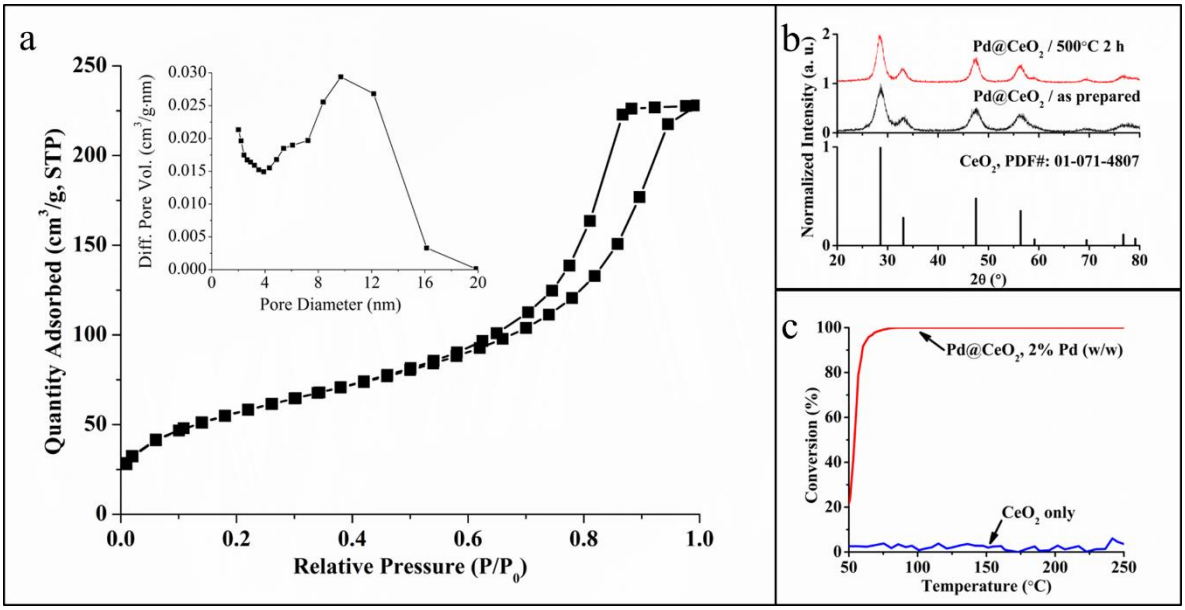

Figure 3.3 (a) N_2 physisorption isotherm of $Pd@CeO_2$ (inset: pore-size distribution). (b) XRD patterns of as-prepared and calcined $Pd@CeO_2$. (c) CO oxidation activity of $Pd@CeO_2$ and blank CeO_2.

Synthesis beyond Pd@CeO₂

The synthesis method reported here provides unique versatility in incorporating other metal oxides, which may be used to improve the thermal stability of CeO_2, thereby significantly broadening the scope of potential applications. Two different approaches were used to achieve said improvements. First, CeO_2-ZrO_2 solid-solution shells were prepared to form $Pd@Ce_{0.8}Zr_{0.2}O_2$. The TEM image (Figure 3.4a) shows a slight morphological change as a consequence of ZrO_2 addition. However, the core@shell structure was preserved. The second approach was to deploy a secondary SiO_2 shell as a sintering-barrier (Figure 3.4b), similar to a method used by Joo et al. [15] to protect TiO_2.

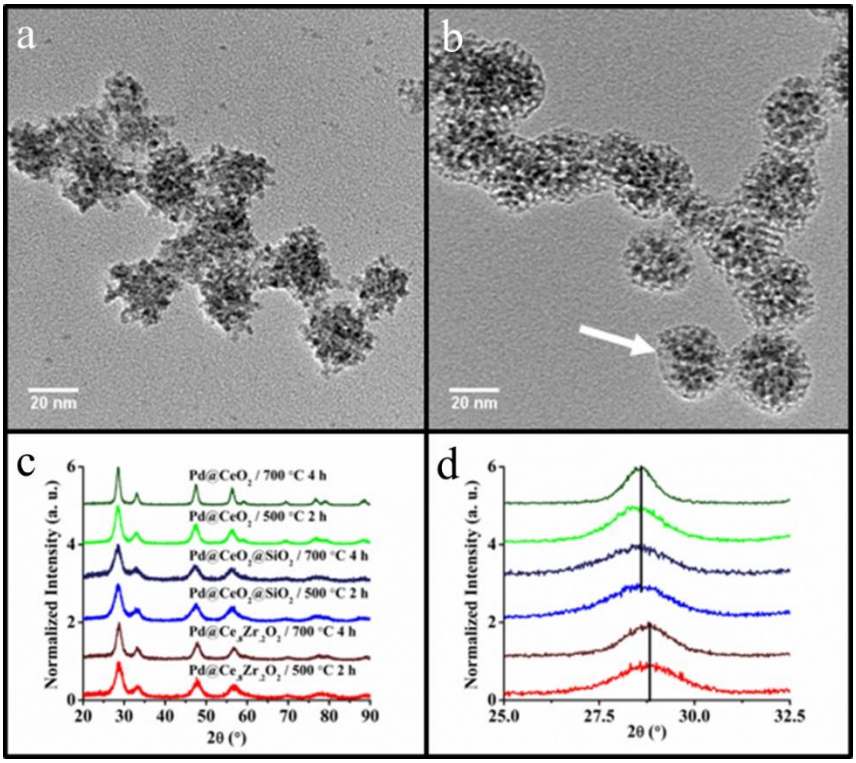

Figure 3.4 TEM images of (a) $Pd@Ce_{0.8}Zr_{0.2}O_2$ and (b) $Pd@CeO_2@SiO_2$ (white arrow = SiO_2 layer). (c) XRD comparison of three core@shell structures after high temperature treatment and (d) the demonstration of the different stability improvement mechanisms between SiO_2 sintering-barrier vs. ZrO_2 solid-solution formation.

The thermal stability was confirmed by comparing XRD patterns, particularly peak sharpness of 500 °C/2 h and 700 °C/4 h calcined powders. As shown in Figure 3.4c, no apparent peak sharpening occurs for both $Pd@Ce_{0.8}Zr_{0.2}O_2$ and $Pd@CeO_2@SiO_2$, while it is noticeable for $Pd@CeO_2$ (700 °C/4 h). The effect is most pronounced for peaks at 78° (2θ). Since the full width at half maximum is inversely proportional to crystallite size, peak sharpening implies growth of crystallize size, i.e., partial sintering. Therefore, $Pd@Ce_{0.8}Zr_{0.2}O_2$ and $Pd@CeO_2@SiO_2$ show superior thermal stabilities compared to $Pd@CeO_2$.

Comparison of the 100 % intensity peak positions further confirms that the two stability improvement strategies arise from different mechanisms. In Figure 3.4d, $Pd@CeO_2@SiO_2$ shows no peak shift compared to the $Pd@CeO_2$ peak position as no solid-solution forms. On the other

hand, the Pd@$Ce_{0.8}Zr_{0.2}O_2$ peak shifts matching that of $Ce_{0.81}Zr_{0.19}O_2$ (PDF#: 01-075-9468). This result shows potential to use the same approach to prepare other shell materials, such as ZrO_2, which has been considered very difficult, due to the fast hydrolysis rates of most ZrO_2 precursors. The same synthesis method could be applied to prepare other core@shell materials with different core and shell sizes.

Conclusions

Pd@CeO_2 nanoparticles were successfully prepared under aqueous conditions, at room temperature, by modifying the ceria precursor's hydrolysis rate in water. Each nanoparticle was composed of a single Pd core and a porous CeO_2 shell. This novel core@shell catalyst proved to be very active for CO oxidation at low temperatures. The thermal stabilities of the Pd@CeO_2 structure were improved by two methods: (1) forming a solid solution with ZrO_2 and (2) providing a secondary SiO_2 shell as a sintering barrier.

Acknowledgements

Financial support for this work by the US Department of Energy under Cooperative Agreement No. DE-EE0006845, Subcontract agreement No. RQ15-337R01 is gratefully acknowledged. Larry Allard at OakRidge National Lab is acknowledged for EDS mapping, University of Michigan College of Engineering and NSF grant # DMR-9871177 is acknowledged for TEM analysis.

References

[1] M. Cargnello, J.J.D. Jaén, J.C.H. Garrido, K. Bakhmutsky, T. Montini, J.J.C. Gámez, R.J. Gorte, P. Fornasiero, Science 337 (2012) 713-717.

[2] B. Li, T. Gu, T. Ming, J. Wang, P. Wang, J. Wang, J.C. Yu, ACS Nano 8 (2014) 8152-8162.

[3] X. Wang, D. Liu, J. Li, J. Zhen, F. Wang, H. Zhang, Chemical Science 6 (2015) 2877-2884.

[4] J. Zhang, L. Li, X. Huang, G. Li, Journal of Materials Chemistry 22 (2012) 10480-10487.

[5] X. Wang, Y. Zhang, S. Song, X. Yang, Z. Wang, R. Jin, H. Zhang, Angewandte Chemie International Edition 55 (2016) 4542-4546.

[6] M. Cargnello, N.L. Wieder, T. Montini, R.J. Gorte, P. Fornasiero, Journal of the American Chemical Society 132 (2010) 1402-1409.

[7] X. Wang, D. Liu, S. Song, H. Zhang, Journal of the American Chemical Society 135 (2013) 15864-15872.

[8] T. Mitsudome, M. Yamamoto, Z. Maeno, T. Mizugaki, K. Jitsukawa, K. Kaneda, Journal of the American Chemical Society 137 (2015) 13452-13455.

[9] T. Mitsudome, Y. Mikami, M. Matoba, T. Mizugaki, K. Jitsukawa, K. Kaneda, Angewandte Chemie International Edition 51 (2012) 136-139.

[10] C.O. Avellaneda, M.A.C. Berton, L.O.S. Bulhões, Solar Energy Materials and Solar Cells 92 (2008) 240-244.

[11] J. Yang, L. Lukashuk, H. Li, K. Föttinger, G. Rupprechter, U. Schubert, Catalysis Letters 144 (2014) 403-412.

[12] M. Cargnello, R.J. Gorte, P. Fornasiero, Catalysis by Ceria and Related Materials, 2nd ed., IMPERIAL COLLEGE PRESS, 2013, pp. 361-396.

[13] E. Yi, W. Wang, J. Kieffer, R.M. Laine, Journal of Materials Chemistry A 4 (2016) 12947-12954.

[14] B. Veisz, Z. Király, Langmuir 19 (2003) 4817-4824.

[15] J.B. Joo, Q. Zhang, I. Lee, M. Dahl, F. Zaera, Y. Yin, Advanced Functional Materials 22 (2012) 166-174.

Chapter 4

Core@shell materials as Three-Way catalysts

Introduction

As mentioned in Chapter 1, most research articles on core@shell materials focus on material synthesis to improve the catalyst's durability, activity, and selectivity. In such studies, simple catalytic model reactions are often used to emphasize the design advantages. Therefore, in many cases the applicability of core@shell catalysts under practical working conditions is not well-known. In a related note, not many articles report the limits of the studied catalysts and the conditions under which these catalysts fail. Regarding such limitations, the applicability of core@shell materials as three-way catalysts (TWCs) is studied under a realistic environment, where multiple redox reactions occur simultaneously. By testing the core@shell catalysts under three-way environments, the benefit of the catalyst morphology in a practical application is assessed.

Since the enactment of the Clean Air Act in 1970, a significant reduction in automotive emissions was achieved via advances in materials research [1-4] and powertrain control [5-7]. Today, all gasoline powered passenger vehicles in the US are equipped with 3-way catalysts to ensure the minimal emission of pollutant gases. However, despite the current system's effectiveness, total prevention of pollutant emission is impossible. This is an inherent issue with

today's system, because it relies on the waste heat from the engine to supply the activation energy for the catalysts. Therefore, a significant amount of pollutants is emitted prior to engine warm-up, especially during colder days [8, 9]. In addition, engines with higher efficiency, such as lean-burn engines [10], may have lower exhaust temperatures [11, 12], creating a new challenge for current aftertreatment systems. To solve such problems, many ideas have been generated and implemented [11, 13]. In the Schwank Lab, a new type of 3-way catalyst was investigated with a goal of achieving low temperature TWC activity. By emphasizing the low temperature activity, the catalyst can effectively treat engine emissions during the engine warm-up and may open possibilities for engine development by providing wider design parameters.

Since developing a new catalyst requires screening through a large number of materials, the project was carried out as a multi-party effort. Starting from the year 2014 to the end of 2017, a three-party (University of Michigan, Collaborator #1: Industrial Partner, Collaborator #2: US National Lab) joint research was conducted, sponsored by The U.S. Department of Energy. During the span of this project, each party was assigned to develop catalyst formulations by pursuing their own specialties. The project's goal was to lower the 90% conversion temperature (T_{90}) of all criteria pollutants to 150 °C [14]; however, any improvement in performance would be considered for further evaluation for material down-selection and production scale-up. In the Schwank Lab, core@shell materials were studied as they were expected to have improved thermal stability and activity, which would be critical for any new TWC.

Experimental

Reactor compatibility confirmation by round-robin catalyst testing

As three parties with three different strategies were involved, it was most sensible to test each party's catalysts at their own facility instead of transferring catalyst samples from one lab to the other. However, the reactor systems in each case were not identical, and this raised the concern that it could affect test results. To assure comparable results, a round-robin catalyst, provided by the Collaborator #1, was tested under a known protocol as reference in all three labs to establish a baseline and to confirm reactor compatibility. The feed gas composition and each lab's testing conditions are listed in Table 4.1 and the reactor schematic used in the Schwank Lab is shown in Figure 4.1.

Table 4.1 Round robin test conditions at all three labs.

<table>
<tr><td rowspan="3">Feed Gas Composition</td><td>[H_2O] = 10%</td><td>[O_2] = stoichiometric</td><td>[CO_2] = 5-10%</td><td rowspan="3">N_2 or Ar Balance</td></tr>
<tr><td>[CO] = 5000 ppm</td><td>[C_3H_8] = 150 ppm</td><td>[C_3H_6] = 500 ppm</td></tr>
<tr><td>[C_2H_4] = 550 ppm</td><td>[H_2] = 1700 ppm</td><td>[NO] = 1000 ppm</td></tr>
<tr><td rowspan="3">Sample Size / Flow Rate</td><td>Collaborator #1</td><td colspan="3">Varied (1 to 3 g / 3.64 to 9.6 L/min)</td></tr>
<tr><td>Collaborator #2</td><td colspan="3">100 mg / 211 mL/min</td></tr>
<tr><td>Univ. of Mich.</td><td colspan="3">200 mg / 389 mL/min</td></tr>
<tr><td>Temperature Control</td><td colspan="4">2 °C/min from 100 °C to above 500 °C</td></tr>
</table>

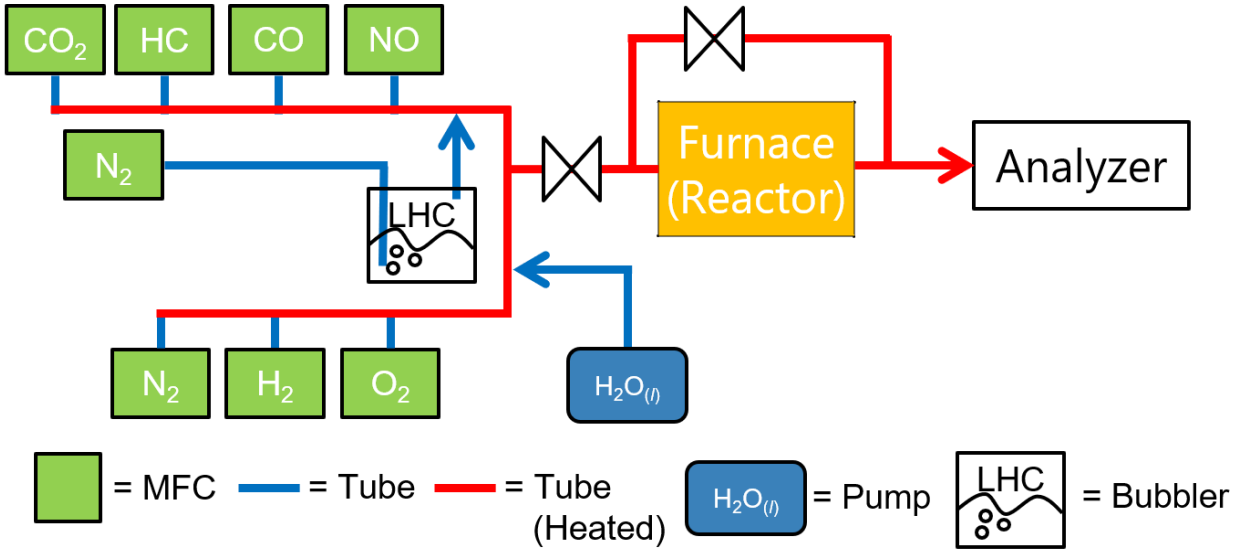

Figure 4.1 Reactor schematic used at Schwank Lab to develop a 3-Way catalyst material.

Testing the performance of core@shell catalysts as 3-Way catalysts

Various core@shell catalysts were prepared for use as TWCs following procedures described in chapters 2 and 3. In a brief summary, regular core@shell catalysts, double-shelled catalysts, and "sandwich" catalysts, containing metal nanoparticles between two oxide layers, were prepared. All prepared catalysts were tested following a known procedure (Table 4.1), except the space velocity was increased to 3,333 ml/min/g catalyst by using 60 mg of catalyst under 200 ml/min flow, compared to 1945 ml/min/g catalyst used for the round-robin testing. Each catalyst test was repeated to confirm reproducibility. After confirming low temperature activity, the catalysts with promising low-temperature activities were in-situ aged under the feed stream at elevated temperatures for 10 h. The aged catalysts were then further tested using the same procedure.

Results and discussion

Reactor compatibility confirmation

As seen from the results summary of round-robin tests (Figure 4.2), the performance of the round-robin catalyst showed similar trends among all three labs. This was an encouraging result, since the reactor compatibility was critical to the productivity of this project. Overall, the reactor in the Schwank Lab tended to require slightly higher temperatures to reach T_{90} than the other reactors, while the reactor owned by Collaborator #2 gave the lowest T_{90} values. The biggest difference in T_{50} was 56 °C (C_3H_8), and for T_{90} it was 82 °C (C_3H_8). The difference may arise for multiple reasons such as the location of thermocouple, reactor geometry, and oxygen concentration in the catalyst bed, to name a few. However, the purpose of this test was not only to obtain a consistent trend but also to use the data to estimate catalysts' performance in all labs. This type of evaluation is very unique because it emphasizes the importance of reactor compatibility, which is often neglected in catalyst evaluation. By using the identical catalyst across three labs, it was demonstrated that each reactor configuration can generate slightly different apparent activities, and such lab-to-lab differences must be considered when evaluating a new catalyst's performance.

A noteworthy discovery made during this cross-lab comparison was that controlling the oxygen concentration in the feed stream was critical to determine the conversion temperature of reactants. Because the three-way reactions requires near-stoichiometric feed conditions, even very small excursions in oxygen concentration can cause switching between rich (fuel-abundant) and lean (oxygen abundant) conditions. By switching from rich to lean condition, the reduction of NO is restricted which causes the overall catalyst performance to drop. A similar very

sensitive response is in the conversion of C_3H_8, which may be converted by steam reforming. Our collaborators found that even a very slight change in oxygen concentration (0.04% change in air-fuel ratio) can alter the T_{90} of propane by 100 °C! This highly sensitive response to even slight fluctuations in feed concentration may explain the mismatches between three labs' Round-Robin results shown in Figure 4.2. This result again emphasizes the importance of controlling the reaction conditions very carefully during catalyst evaluation, a point that is often unnoticed in articles which claim discovery of highly active catalysts.

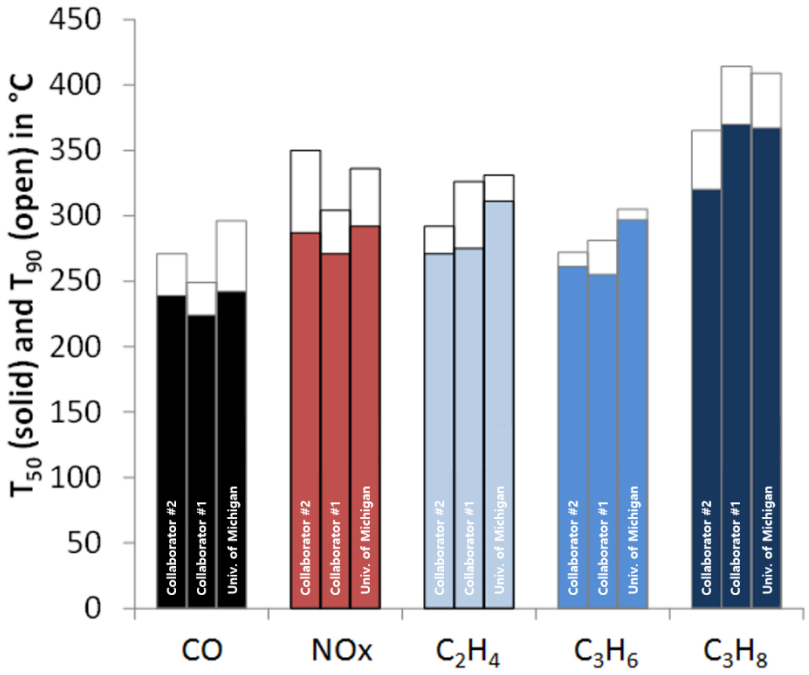

Figure 4.2. Summary of cross-lab testing with the round-robin catalyst test under 3-Way condition.

Core@shell materials as 3-Way catalysts

After confirming reactor compatibility between the three collaborators, the performances of our $Pd@SiO_2$ and Pd/SiO_2 were compared under 3-way conditions (Figures 4.1.3 and 4.1.4). The performance of fresh catalysts showed that $Pd@SiO_2$ showed significantly better activity when it is fresh than after hydrothermal aging at 800 °C for 10 h. As expected, the $Pd@SiO_2$

catalyst exhibited much better hydrothermal stability compared to Pd/SiO_2. As shown in Figures 4.1.3 and 4.1.4, the performance of $Pd@SiO_2$ showed minor aging compared to Pd/SiO_2. This result was surprising, because much worse performance was anticipated from $Pd@SiO_2$ after aging, as SiO_2 is known not to possess hydrothermal stability.

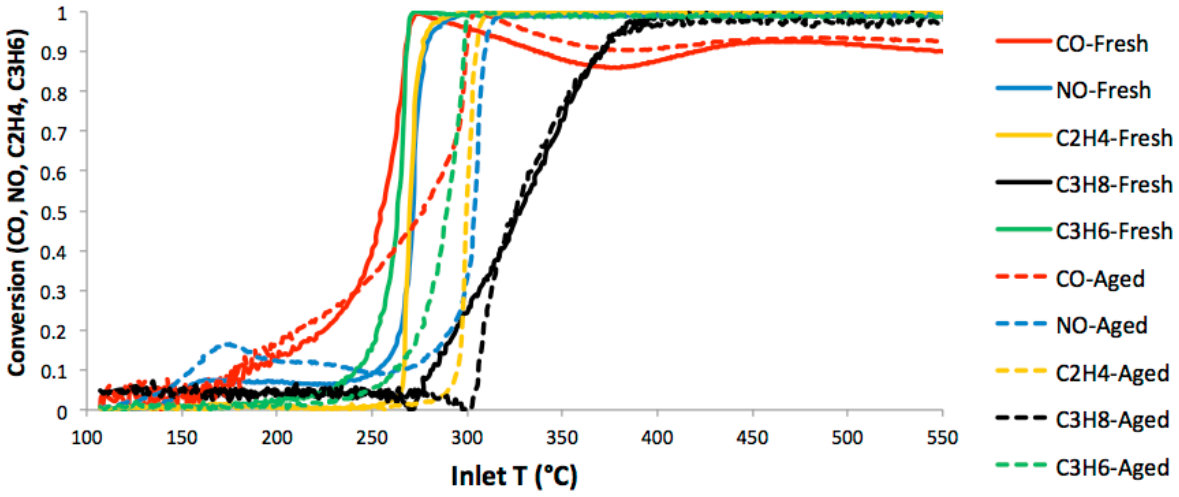

Figure 4.3 Activity of $Pd@SiO_2$ following the reaction condition listed in Table 4.1 (Solid: Fresh catalyst, Dash: Catalyst hydrothermally aged at 800 °C for 10 hours)

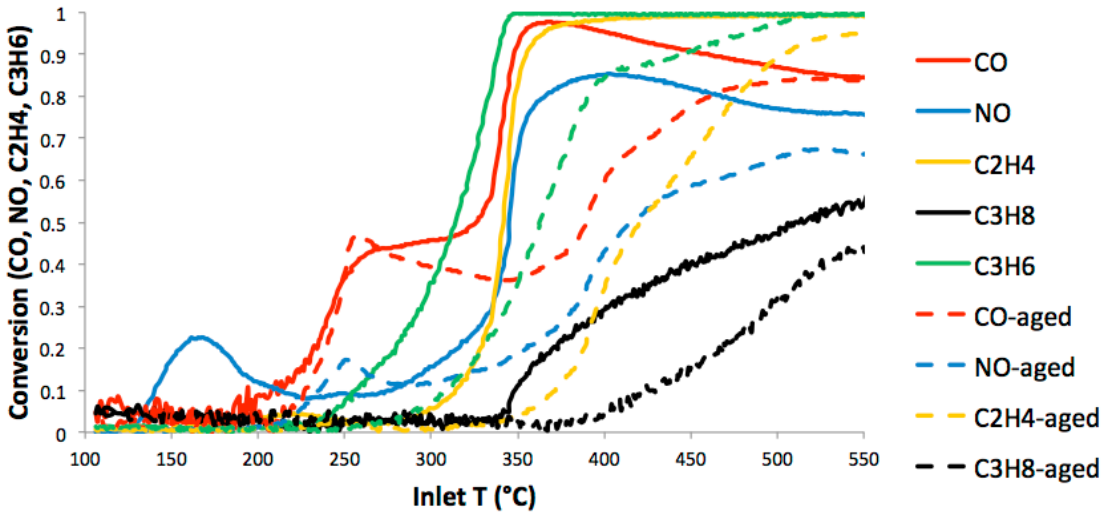

Figure 4.4 Activity of Pd/SiO_2 following the reaction condition listed in Table 4.1 (Solid: Fresh catalyst, Dash: Catalyst hydrothermally aged at 800 °C for 10 h)

Therefore, hydrothermally aged Pd@SiO_2 catalysts were further analyzed to check for changes in catalyst morphology. As seen in Figure 4.5b, neighboring SiO_2 shells merged after hydrothermal aging at 800 °C. However, the core@shell morphology remains throughout the catalyst. A more severe change occurs when the catalyst is hydrothermally aged at 900 °C [15]. As seen in Figure 4.5c, aging at 900 °C results in destruction of the core@shell structure. All Pd seems to have sintered and deposited to form one big particle outside the SiO_2 support. This result suggests the limits of maintaining core@shell morphologies in a 3-way catalyst.

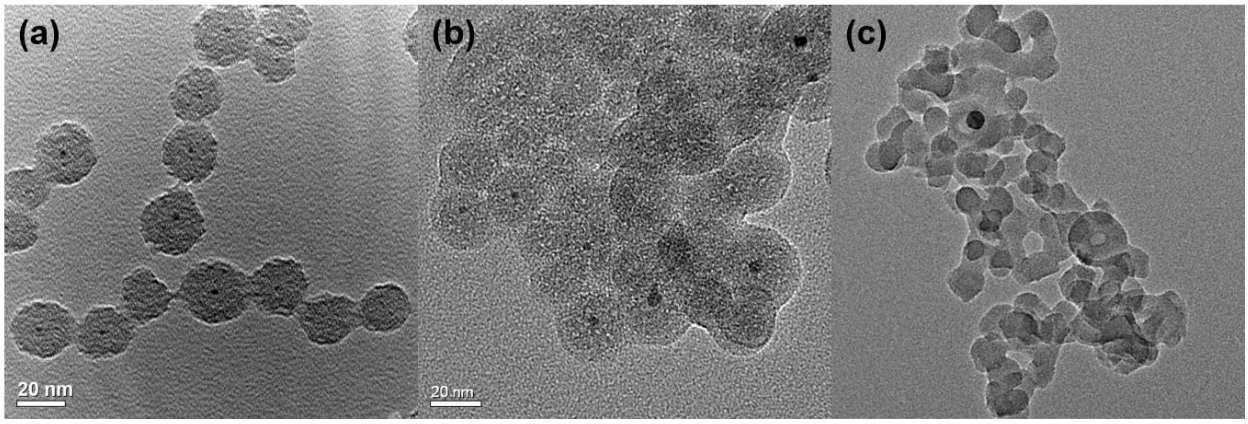

Figure 4.5. TEM images of Pd@SiO_2 catalyst used for 3-Way activity evaluation (a) Fresh, (b) 800 °C hydrothermal aging, 10 h, (c) 900 °C hydrothermal aging, 10 h

Despite confirming inevitable destruction of the core@shell architecture under hydrothermal aging at 900 °C, the activity study was continued by expanding the synthesis towards materials that can promote the TWC activity. This way, the catalyst may remain active even after a morphology change. As general catalyst design goals, the activity was promoted using CeO_2 [2, 16, 17] and the hydrothermal stability was improved by dding ZrO_2 [18, 19]. The core@shell architecture also provides a larger number of active sites by decorating the exterior of an already existing catalyst with another precious metal.

A series of catalysts were prepared to demonstrate the design goals, as shown in Figure 4.6. As predicted, switching from a SiO_2 to a CeO_2 shell brought a significant decrease in T_{90} for all reactants. Adding an additional ZrO_2 layer did not alter the activity by much, as the ZrO_2 layer was implemented to improve hydrothermal stability. In fact, the $Pd@CeO_2@ZrO_2$ catalyst performed slightly worse than the $Pd@CeO_2$ catalyst. Finally, decorating the exterior with Rh at low loading further improved the activity.

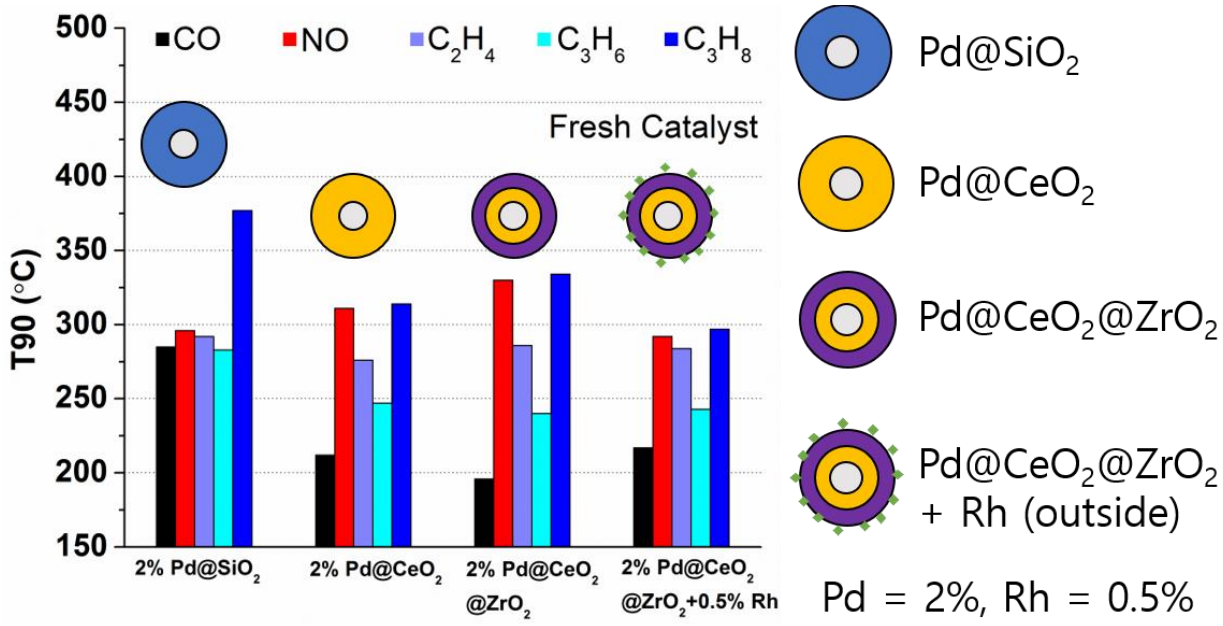

Figure 4.6. A summary of fresh core@shell catalysts' performance under 3-Way environment described in Table 4.1.

The durability was tested by aging all catalysts listed in Figure 4.6 under the reaction stream at 800 °C for 10 h. After aging, in general, the activity degrades (Figure 4.7), as expected. However, catalysts with ZrO_2 double-shell were more hydrothermally stable than catalysts without, as the $Pd@CeO_2@ZrO_2$ catalyst performed better than $Pd@CeO_2$ after aging. This result confirms that application-specific core@shell catalysts can be designed and synthesized based on the properties needed for the application. While the demonstrated survival of

core@shell structures during aging at 800°C is quite remarkable, there is still the challenge of making these types of catalysts survive temperature spikes exceeding 1000°C, so that they meet automotive industry requirements.

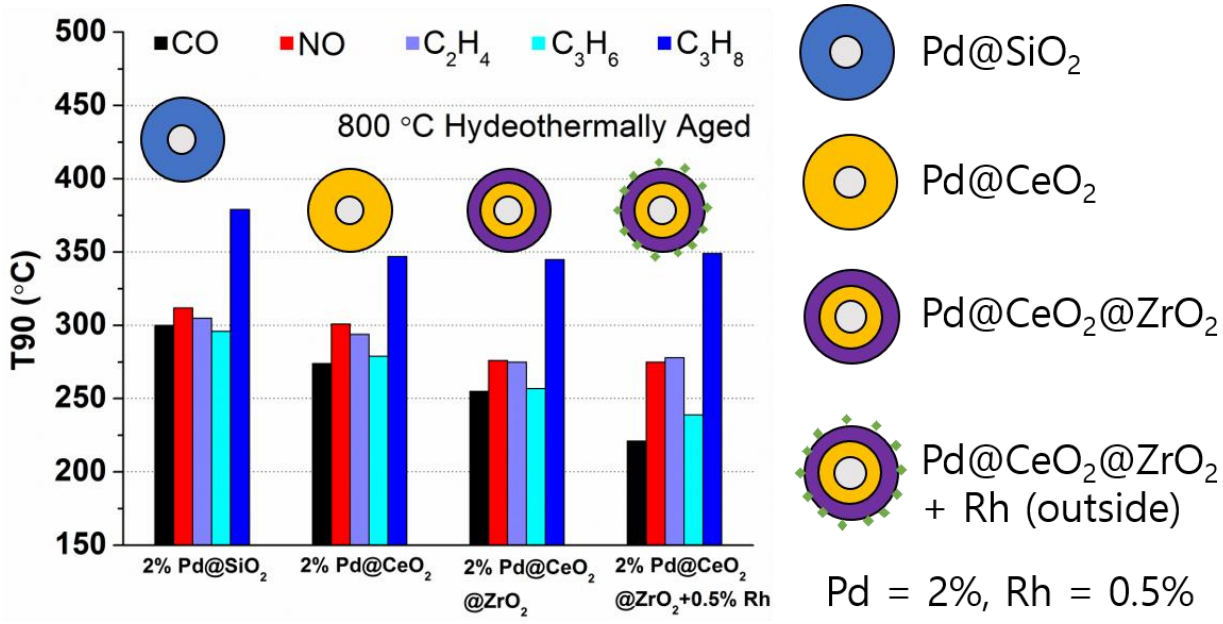

Figure 4.7. A summary of hydrothermally aged core@shell catalysts' performance under 3-way environment described in Table 4.1.

Apart from apparent catalyst deactivation, an interesting change in activity was observed, which may indicate interaction between Pd and CeO_2. When comparing the results in Figures 4.6 and 4.7, NO is the only species with decreased T_{90} after aging. This was an interesting result, because all other reactants' T_{90} increased after aging. As of now, we believe this phenomenon is an indication of a Pd-CeO_2 interaction. When the catalyst is fresh, CeO_2 can donate oxygen to the reaction scheme which may interfere with NO reduction. Once aged, there may not be as much active oxygen transfer from CeO_2 to Pd allowing NO to be reduced. One hypothetical explanation is that the aged CeO_2 may only act as an oxygen storage material with minimal

capability to deliver the oxygen to the Pd as a reactant. Based on this hypothesis, a study of interaction between Pd and CeO_2 was initiated (Chapter 6).

Conclusions

In this chapter, the efforts were made to prepare a new TWCs that can achieve 90 % conversion of all criteria pollutants at 150 °C. In the Schwank Lab, the applicability of Pd-based core@shell catalysts was surveyed by testing both fresh and aged catalysts under TWC conditions. Although the T_{90} = 150 °C was not achieved, a few important findings resulted from this study. First, even the simplest synthesis method for core@shell materials is not suitable for industrial production. During the project, all materials were prepared in a one-pot, aqueous environment. However, because of inherent limitations of nanoparticle preparation, the current scheme was concluded to be unsuitable for catalyst production on an industrial scale. Second, interesting behavior of encapsulated Pd was observed during aging. As shown in Figure 4.5b, numerous "core-less" SiO_2 particles were found after aging. This observation provides the possibility of using core@shell materials as model catalysts to observe the behavior of a metal at high temperature, because the geometry offers clear distinction between particles.

References

[1] A.M. Beale, F. Gao, I. Lezcano-Gonzalez, C.H.F. Peden, J. Szanyi, Chemical Society Reviews 44 (2015) 7371-7405.

[2] P. Gélin, M. Primet, Applied Catalysis B: Environmental 39 (2002) 1-37.

[3] J. Li, H. Chang, L. Ma, J. Hao, R.T. Yang, Catalysis Today 175 (2011) 147-156.

[4] J. Wang, H. Chen, Z. Hu, M. Yao, Y. Li, Catalysis Reviews 57 (2015) 79-144.

[5] A. Abdel-Rahman, International Journal of Energy Research 22 (1998) 483-513.

[6] T.V. Johnson, SAE International Journal of Fuels and Lubricants 3 (2010) 16-29.

[7] N. Docquier, S. Candel, Progress in energy and combustion science 28 (2002) 107-150.

[8] M. Weilenmann, J.-Y. Favez, R. Alvarez, Atmospheric environment 43 (2009) 2419-2429.

[9] M. Weilenmann, P. Soltic, C. Saxer, A.-M. Forss, N. Heeb, Atmospheric environment 39 (2005) 2433-2441.

[10] K. Horie, K. Nishizawa, T. Ogawa, S. Akazaki, K. Miura, The development of a high fuel economy and high performance four-valve lean burn engine, SAE Technical Paper, 1992.

[11] N. Takahashi, H. Shinjoh, T. Iijima, T. Suzuki, K. Yamazaki, K. Yokota, H. Suzuki, N. Miyoshi, S.-i. Matsumoto, T. Tanizawa, Catalysis Today 27 (1996) 63-69.

[12] N. Miyoshi, S.i. Matsumoto, K. Katoh, T. Tanaka, J. Harada, N. Takahashi, K. Yokota, M. Sugiura, K. Kasahara, Development of new concept three-way catalyst for automotive lean-burn engines, SAE Technical Paper, 1995.

[13] J.K. Hochmuth, P.L. Burk, C. Tolentino, M.J. Mignano, Hydrocarbon Traps for Controlling Cold Start Emissions, SAE Technical Paper, 1993.

[14] C.D. Michael Zammit, Chang Kim, Christine Lambert, George Muntean, Chuck Peden, Jim Parks, Ken Howden, (2012).

[15] K.L.S. Masias, T.C. Peck, P.T. Fanson, RSC Advances 5 (2015) 48851-48855.

[16] J. Zhang, L. Li, X. Huang, G. Li, Journal of Materials Chemistry 22 (2012) 10480-10487.

[17] C. Seo, E. Yi, M. Nahata, R.M. Laine, J.W. Schwank, Materials Letters 206 (2017) 105-108.

[18] M. Hirano, H. Inada, Journal of materials science 26 (1991) 5047-5052.

[19] K. Yoshida, Y. Hirano, H. Fujii, T. Tsuru, M. Asaeda, Journal of chemical engineering of Japan 34 (2001) 523-530.

Chapter 5

Palladium redispersion at high temperature within the Pd@SiO_2 core@shell structure

Introduction

The sintering of platinum group metals (PGM) at high temperatures is often responsible for the loss of catalytic activity during practical applications of environmental catalysts. Recently, researchers suggested tackling the sintering problem by designing unique catalyst formulations [1-3] and structures such as embedded [4] and core@shell [5, 6] geometries, where a PGM core is surrounded by an oxide shell. For example, different synthesis methods have been developed to prepare a catalyst with a Pd core and SiO_2 shell (Pd@SiO_2) [7-9] with improved thermal stability. However, to the best of our knowledge, not many articles report the stability beyond 800 °C [10], where thermal PdO-to-Pd decomposition occurs and severe sintering is expected [11-13]. Instead, most Pd@SiO_2 catalysts reported in the literature were aged only up to about 700 °C, at which no severe sintering is expected. In fact, according to some previous studies [12-15], aging at 700 °C might induce redispersion of PdO under an oxidizing atmosphere. Therefore, testing the thermal stability of Pd@SiO_2 at temperatures above the PdO

decomposition temperature (800 °C) is important to demonstrate the thermal stability benefit resulting from the core@shell geometry.

A study by Zhang et al. [16] illustrates such efforts. By studying a Pd@CeO_2 catalyst, supported on Si-functionalized Al_2O_3, they observed that the Pd core underwent structural reconfiguration at temperatures between 500 and 800 °C. However, the catalyst was not thermally stable, and the core@shell morphology was lost after high temperature exposure [17], resulting in similar outcomes with recently reported PGM trapping onto reducible oxides such as CeO_2 [18-20]. Therefore, it was difficult to isolate the behavior of the Pd core apart from the recrystallization of the CeO_2 shell. Overcoming such shortcomings, direct evidence of high-temperature Pd redispersion are reported here, using a Pd@SiO_2 catalyst. By maintaining the core@shell geometry throughout the high temperature aging above 800 °C, we could isolate the behavior of Pd from the effect of the shell morphology change. The finding provides a meaningful insight into the high-temperature redispersion behavior of PGM over a non-reducible oxide, a phenomenon which is scarcely observed [21], and gives new perspectives for the preparation of thermally stable PGM catalysts.

Experimental

Synthesis of palladium-core@silica-shell catalyst (Pd@SiO_2)

Pd@SiO_2 catalysts with 4.0 nm Pd core diameter and 22 nm SiO_2 shell thickness were prepared by a modified one pot, two-step method introduced in Chapter 2. To synthesize the catalyst, 20 mL of 0.12 mmol $Pd(NO_3)_2{\cdot}2H_2O_{(aq)}$ solution was mixed in 20 ml of 0.2 mmol $TTAB_{(aq)}$ solution. Subsequently, a 7.1 mmol $N_2H_4{\cdot}H_2O$ solution was added to produce Pd nanoparticles protected by the TTAB surfactant, signified by a rapid color change from bright

orange to clear black. The Pd nanoparticle suspension was stirred for 10 minutes and further diluted by adding 120 ml of 1.2 mmol TTAB solution. The diluted suspension did not show any sign of agglomeration and was stirred vigorously for 20 minutes. After stirring, the pH of the diluted Pd nanoparticle suspension was adjusted to 10.7 by NaOH. To this basic suspension, 10.8 mmol TEOS diluted in 5 mL ethanol was added in three aliquots with 10-minute intervals between each addition. The catalyst was stirred for 24 hours to complete the encapsulation of Pd nanoparticles by SiO_2. The catalyst was then collected by centrifugation, washed three times with water and three times with ethanol, and finally dried overnight in air at 80 °C.

CO oxidation procedure

Prior to CO oxidation, the catalyst was pretreated at a desired aging temperature under ambient air. The aging was carried out by ramping the temperature at 2 °C/min to the desired temperature (500 °C or 800 °C). After holding the catalyst for 4 hours at the aging temperature, the furnace was cooled down without forced convection. CO oxidation was carried out by loading a pretreated 60 mg of 60-80 mesh catalyst powder into a vertical quartz reactor with ID = 4 mm. Prior to reaction, the catalyst was oxidized by air and was used as is. To obtain the CO light-off curve, the pretreated catalyst was cooled down to 50 °C, and was saturated by the reactant gas (1% CO and 1.5% O_2, bal. N_2) for 30 minutes at 200 ml/min of total flow. After 30 minutes, the temperature was raised at 2 °C/min up to 400 °C. The exit stream was analyzed by measuring both CO and CO_2 concentrations by a Thermo Nicolet FTIR gas analyzer.

Electron microscopy experimental procedures

Samples were prepared for electron microscopy by dispersing the prepared catalysts in ethanol, and loading the suspension by placing a drop onto the appropriate support for the

electron microscope(s) used. Standard bright-field transmission electron micrographs (BF-TEM) images were recorded using a JEOL 2010 TEM operated at 200 kV, with the catalysts loaded onto 200-mesh copper grids coated with amorphous carbon as the support. High-resolution BF-TEM images (HRTEM) were recorded with the catalyst suspension deposited on copper grids with holey carbon support films.

For the *in situ* reaction experiments, a 200 kV JEOL 2200FS (scanning) transmission electron microscope ((S)TEM) with aberration correction for the illumination lenses (CEOS GmbH, Heidelberg, Ger) was used, with the catalysts dispersed onto Protochips "Fusion™" heaters (Protochips Inc., Raleigh, NC) having a SiN membrane support). The instrument permits both BF and high-angle annular dark-field (HAADF) images to be recorded simultaneously, at a nominal HAADF resolution of 0.07 nm [3]. The Protochips Atmosphere™ closed-cell gas-reaction system with computer control of gas delivery and reaction temperature [4, 5] was used for the reaction studies reported here. Care was taken with all experiments to minimize the catalyst exposure to the electron beam with the gas cell at high temperature, to control adverse effects of the beam on the reaction behavior. The catalyst was first oxidized *in situ* in 1atm air at 200 °C for 1 hour, prior to aging at different temperatures. The *in situ* experiments were carried out by holding the sample at each temperature for 30 minutes then cooling down to 200 °C for imaging (where it was shown that the catalyst was not changed over time with imaging at magnifications of 500 kX or lower). The heater temperature was typically ramped at 10 °C/s, for both heating and cooling cycles.

Results and discussion

Confirmation of high temperature Pd redispersion

A Pd@SiO_2 catalyst with a 4.0 nm Pd core and a 22 nm SiO_2 shell thickness was synthesized by following a general procedure for a modified, one-pot, two-step method [8, 22] and CO oxidation was used as catalytic probe reaction. Since CO oxidation is a structure insensitive reaction on a Pd surface, CO conversion is closely correlated with the number of available Pd surface atoms and thus the dispersion of Pd. We found that the catalysts calcined at 500 and 800 °C did not show many morphological differences, except for the expected loss of mesoporosity of the SiO_2 shell after 800 °C aging.

However, interestingly, improved CO oxidation activity (i.e., lower light-off temperature) was observed (Figure 5.1) for the catalyst aged at 800 °C. The light-off temperatures (50% CO conversion) after aging at 500 and 800 °C were 250 °C and 229 °C, respectively, a *decrease* of 21 °C for the 800 °C aged sample. These CO oxidation light-off curves, also reported in Chapter 2, were repeatable across two different batches of samples and for multiple cycles on one sample, giving confidence that the observations are statistically valid. To verify the distinct aging impact, a conventional Pd/SiO_2 supported catalyst with a very similar Pd loading was prepared by impregnation, and again CO oxidation was used as the probe reaction. The CO light-off temperature after aging at 800 °C was 270 °C, a 21 °C *increase* from the value after the aging of this catalyst at 500 °C, a result expected for conventional catalysts where Pd undergoes sintering during aging at 800°C. The opposite behavior observed for the Pd@SiO_2 catalyst is an indicator of the improved thermal stability provided by the core@shell geometry.

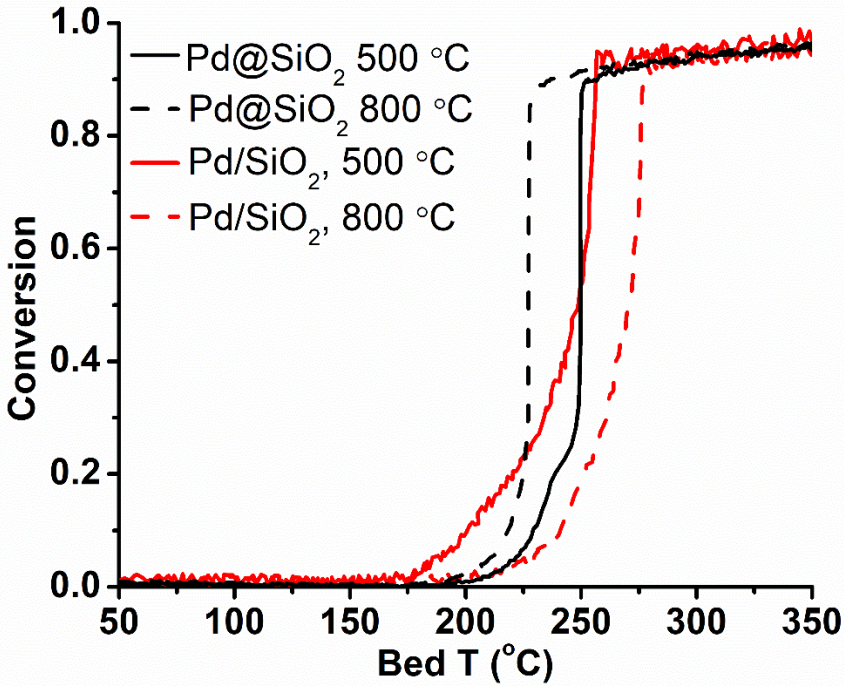

Figure 5.1 CO oxidation light-off comparison between the core@shell ($Pd@SiO_2$, black) and the supported (Pd/SiO_2, red) catalysts after calcining in air at 500 °C (solid) and 800 °C (dash).

To investigate the origins of the observed enhanced activity after aging at 800 °C for $Pd@SiO_2$ high angle annular dark field (HAADF) imaging was used to reveal the underlying reason. Figure 5.2 shows the HAADF images (in which Pd appears bright) of $Pd@SiO_2$ catalysts as-prepared, after aging at 500 °C in air, and after aging at 800 °C in air. These straightforward images indicate that the original (Figure 5.2a) and the 500 °C pretreated (Figure 5.2b) catalysts did not show any obvious signs of Pd particle size changes. In comparison, after aging at 800 °C, multiple new Pd atom clusters with diameters of less than 2 nm are clearly visible, as shown in Figure 5.2c. Since the catalyst shown in Figure 5.2c was heat-treated at 500 °C prior to aging at 800 °C, one can conclude that the redispersion of Pd nanoparticles only occurs due to aging at 800 °C. This surprising and unexpected result could reconfirm and explain the enhanced CO oxidation activity of the 800 °C aged $Pd@SiO_2$ catalyst. Previously, high thermal stability

around 700 °C has been reported in the literature for Pd-based core@shell catalysts [7-9]. However, to the best of my knowledge, Pd redispersion on SiO_2 surfaces after aging at temperatures above the PdO to Pd decomposition temperature has not been clearly demonstrated before.

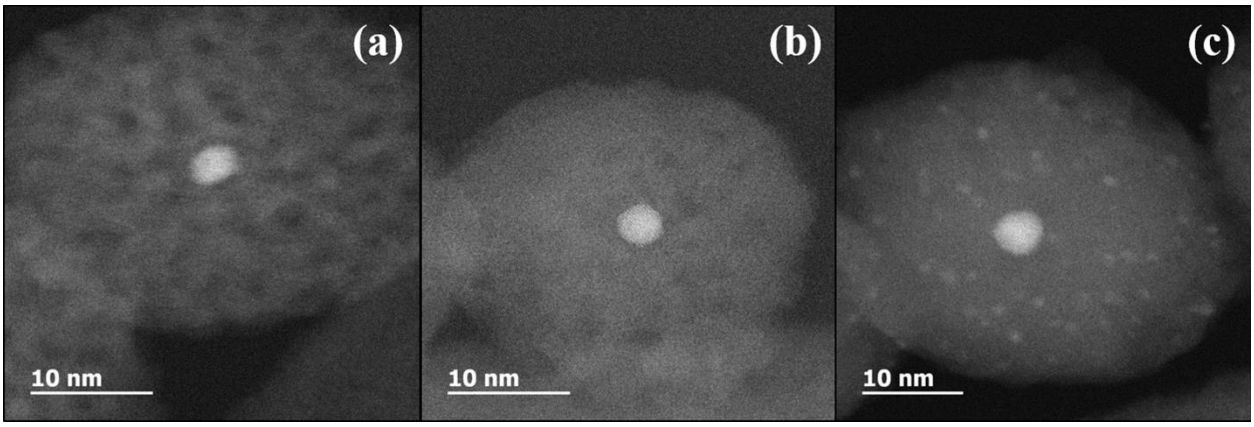

Figure 5.2 HAADF images of Pd@SiO_2 showing high-temperature redispersion of Pd particles. (a) as-prepared, (b) after 500 °C calcination in air, and (c) after 800 °C calcination in air.

Redispersion mechanism study via in situ TEM

As the CO oxidation comparison between the Pd@SiO_2 and the supported Pd/SiO_2 showed different trends in aging response, the high-temperature Pd redispersion can be related to the core@shell architecture. Therefore, to further validate the findings and to clearly demonstrate these different aging behaviors, an atmospheric *in situ* TEM experiment was carried out in air on a catalyst containing both encapsulated and exposed palladium (Pd@SiO_2 and Pd/SiO_2, respectively), prepared by loading SiO_2-encapsulated Pd nanoparticles onto an already existing Pd@SiO_2 catalyst. As shown in Figure 5.3a, encapsulated Pd (yellow arrow) as well as exposed Pd (red arrow) nanoparticles can be seen after aging at 200 °C. As the temperature increased, the exposed palladium shows high mobility (Figure 5.3b, 500 °C). The exposed Pd particles undergo geometrical transformations, indicating particle migration and coalescence [23-25].

In contrast, the encapsulated palladium particles were quite thermally stable to 700 °C, at which point PdO starts decomposing to Pd particles that diminish by vaporization/melting. After aging at 800 °C, the exposed Pd forms a large crystal (Figure 5.3c), while the encapsulated Pd was no longer observable. Since the encapsulated Pd sinters onto the large crystal via Ostwald ripening [24, 26, 27] at high temperature, a separate and parallel experiment containing only $Pd@SiO_2$ was conducted as a comparison. In this additional *in situ* experiment, only the disappearance of Pd particles was observed without the formation of a large, sintered Pd particle after aging at 800 °C (Figure 5.4). These *in situ* results provide direct evidence that encapsulated Pd particles can completely redisperse within the SiO_2 shell in the form of very small atomic clusters, while the conventionally supported Pd particles canno. On further analysis, we found convincing evidence that embedded Pd cores that disappear during the *in situ* TEM experiments redisperse as Pd atomic clusters. Such migration and relocation of Pd clusters could be caused by the vaporization of Pd nanoparticles and diffusion of atomic Pd clusters.

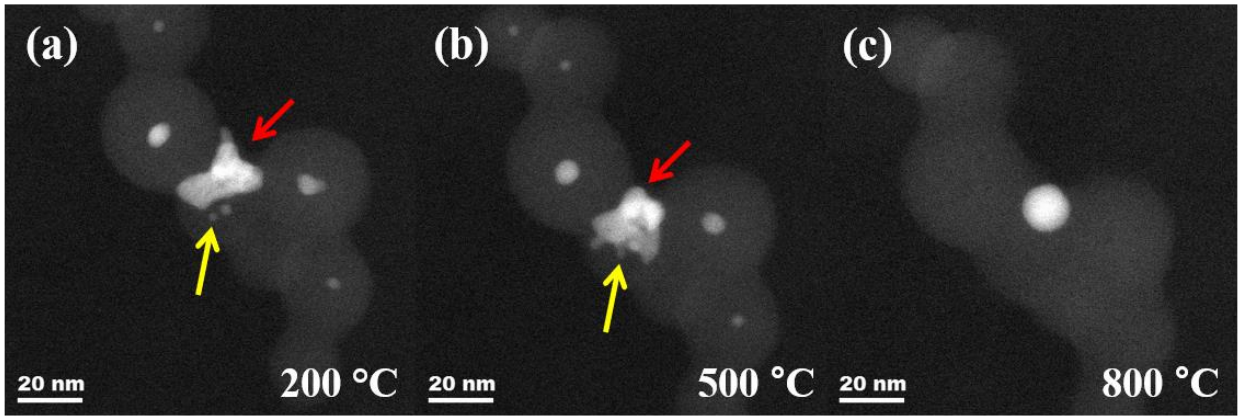

Figure 5.3 Sintering behaviors of different Pd particles at high temperature. *In situ* TEM of the $Pd@SiO_2$ + Pd/SiO_2 mixed catalyst after aging in air at different temperatures for 30 min: (a) 200 °C, (b) 500 °C, and (c) 800 °C (red arrow: exposed Pd; yellow arrow: encapsulated Pd).

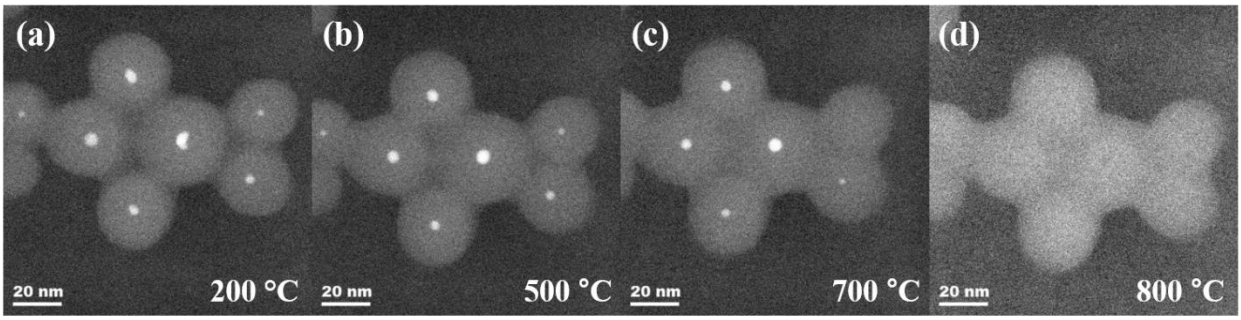

Figure 5.4 HAADF images showing results of the *in situ* (S)TEM experiment with Pd@SiO_2 alone after *in situ* aging at (a) 200 °C, (b) 500 °C, (c) 700 °C, and (d) 800 °C. No large sintered Pd particle is observed after aging at 800 °C.

The *in situ* experiment helped us understand the reason for Pd redispersion within Pd@SiO_2 catalysts. As mentioned above, very different moderate-temperature sintering behaviors were observed between exposed and encapsulated Pd nanoparticles. By encapsulation, moderate-temperature particle migration and coalescence was minimized due to the structural restriction caused by the pores in the core@shell geometry. At high temperatures, the encapsulated Pd core can melt and then vaporize. Once the Pd cores vaporize, there is no large Pd crystal in the vicinity, on which mobile Pd atoms can recrystallize. Therefore, during cooling, the molten/vaporized Pd atoms condense locally into atom clusters, essentially increasing the Pd dispersion (Figure 5.2c). In contrast, for Pd/SiO_2, the supported Pd particles have a chance to migrate and form larger aggregate even at moderate temperatures. At high temperatures, this aggregate sinter into bigger Pd crystals. Some Pd atoms would go through melting and vaporization, however, and then recondense onto an already existing Pd particle without any restriction. The Pd redispersion is much less likely for a Pd/SiO_2 catalyst, despite the fact that a very similar Ostwald ripening process may occur at high temperature for both geometries. A schematic mechanism for the different sintering and redispersion behaviors of Pd nanoparticles in the Pd@SiO_2 and Pd/SiO_2 catalysts is illustrated in Figure 5.5.

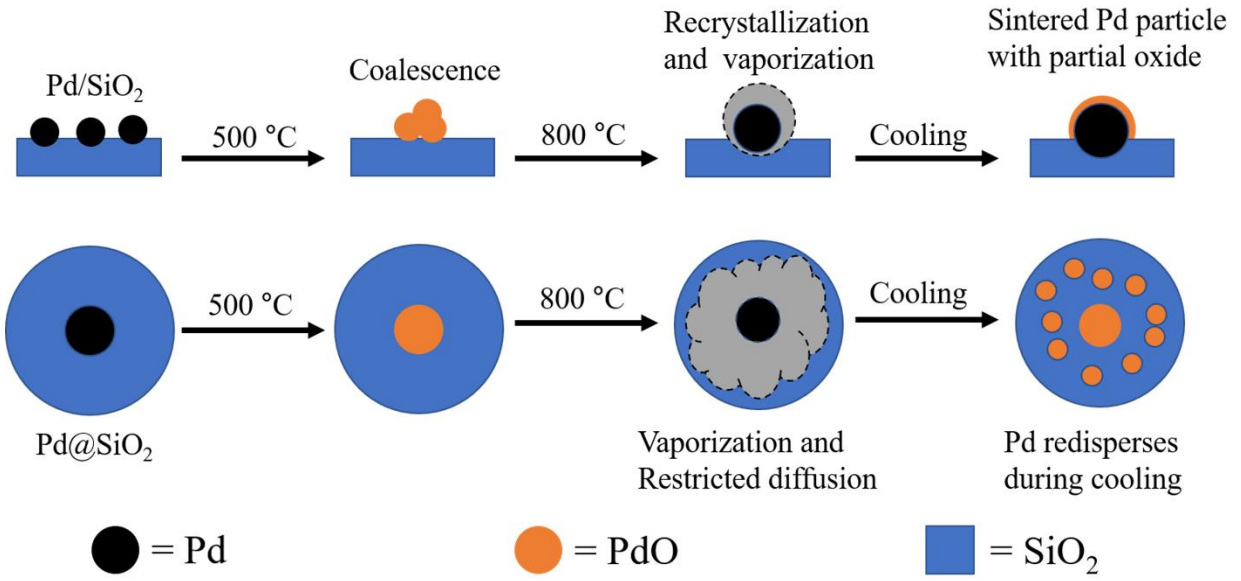

Figure 5.5 Schematic comparison of sintering and redispersion of Pd particles in different environments: (top row) supported Pd/SiO_2, (bottom row) $Pd@SiO_2$.

Conclusions

We discovered that the catalytic CO oxidation activity of the $Pd@SiO_2$ catalyst improved, when catalyst aging temperature was increased from 500 to 800 °C in an oxidizing environment. This behavior is completely opposite from the expected behavior for a conventional Pd/SiO_2 supported catalyst, where 800 °C aging would result in severe sintering and activity loss. HRTEM proved that, after aging at 800 °C, encapsulated Pd nanoparticles (~ 4 nm) could redisperse into much smaller Pd atom clusters (≤ 2 nm), which is rarely observed on a non-reducible oxide such as SiO_2. On the other hand, a supported Pd/SiO_2 catalyst did not show the formation of such atom clusters and instead underwent the expected sintering into larger Pd particles. To further confirm this unique Pd redispersion over a non-reducible oxide, *in situ* TEM experiments were carried out. Based on the TEM experiments, we propose a mechanism explaining the high temperature redispersion of Pd in the $Pd@SiO_2$ catalyst.

Acknowledgements

This work was supported by the US Department of Energy under Cooperative Agreement [No. DE-EE0006845], Subcontract agreement [No. RQ15-337R01]. The support of the University of Michigan College of Engineering and NSF grant [DMR-9871177] for the JEOL 2010F transmission electron microscope is also acknowledged.

References

[1] C.W. Han, P. Majumdar, E.E. Marinero, A. Aguilar-Tapia, R. Zanella, J. Greeley, V. Ortalan, Nano Letters 15 (2015) 8141-8147.

[2] A.M. Venezia, L.F. Liotta, G. Pantaleo, V. La Parola, G. Deganello, A. Beck, Z. Koppány, K. Frey, D. Horváth, L. Guczi, Applied Catalysis A: General 251 (2003) 359-368.

[3] B. Pawelec, V. La Parola, R.M. Navarro, S. Murcia-Mascarós, J.L.G. Fierro, Carbon 44 (2006) 84-98.

[4] Y.H. Ng, S. Ikeda, T. Harada, T. Sakata, H. Mori, A. Takaoka, M. Matsumura, Langmuir 24 (2008) 6307-6312.

[5] A.J. Forman, J.-N. Park, W. Tang, Y.-S. Hu, G.D. Stucky, E.W. McFarland, ChemCatChem 2 (2010) 1318-1324.

[6] S.H. Joo, J.Y. Park, C.-K. Tsung, Y. Yamada, P. Yang, G.A. Somorjai, Nature Matererials 8 (2009) 126-131.

[7] J.-N. Park, A.J. Forman, W. Tang, J. Cheng, Y.-S. Hu, H. Lin, E.W. McFarland, Small 4 (2008) 1694-1697.

[8] Y. Hu, K. Tao, C. Wu, C. Zhou, H. Yin, S. Zhou, The Journal of Physical Chemistry C 117 (2013) 8974-8982.

[9] Y. Xu, J. Ma, Y. Xu, L. Xu, L. Xu, H. Li, H. Li, RSC Advances 3 (2013) 851-858.

[10] D. Pi, W.Z. Li, Q.Z. Lin, Q.F. Huang, H.Q. Hu, C.Y. Shao, Energy Technology 4 (2016) 943-949.

[11] M. Peuckert, The Journal of Physical Chemistry 89 (1985) 2481-2486.

[12] J.A. Lupescu, J.W. Schwank, K.A. Dahlberg, C.Y. Seo, G.B. Fisher, S.L. Peczonczyk, K. Rhodes, M.J. Jagner, L.P. Haack, Applied Catalysis B: Environmental 183 (2016) 343-360.

[13] X. Chen, J.W. Schwank, G.B. Fisher, Y. Cheng, M. Jagner, R.W. McCabe, M.B. Katz, G.W. Graham, X. Pan, Applied Catalysis A: General 475 (2014) 420-426.

[14] X. Chen, Y. Cheng, C.Y. Seo, J.W. Schwank, R.W. McCabe, Applied Catalysis B: Environmental 163 (2015) 499-509.

[15] H. Lieske, J. Voelter, The Journal of Physical Chemistry 89 (1985) 1841-1842.

[16] S. Zhang, C. Chen, M. Cargnello, P. Fornasiero, R.J. Gorte, G.W. Graham, X. Pan, Nature communications 6 (2015) 7778.

[17] C. Seo, E. Yi, M. Nahata, R.M. Laine, J.W. Schwank, Materials Letters 206 (2017) 105-108.

[18] Y. Guan, E.J.M. Hensen, Physical Chemistry Chemical Physics 11 (2009) 9578-9582.

[19] J. Jones, H. Xiong, A.T. DeLaRiva, E.J. Peterson, H. Pham, S.R. Challa, G. Qi, S. Oh, M.H. Wiebenga, X.I. Pereira Hernández, Y. Wang, A.K. Datye, Science 353 (2016) 150-154.

[20] Y. Gao, W. Wang, S. Chang, W. Huang, ChemCatChem 5 (2013) 3610-3620.

[21] E.J. Peterson, A.T. DeLaRiva, S. Lin, R.S. Johnson, H. Guo, J.T. Miller, J. Hun Kwak, C.H.F. Peden, B. Kiefer, L.F. Allard, F.H. Ribeiro, A.K. Datye, Nature Communications 5 (2014) 4885.

[22] J.-T. Song, X.-S. Zhang, M.-Y. Qin, Y.-D. Zhao, Dalton Transactions 44 (2015) 7752-7756.

[23] R.J. Liu, P.A. Crozier, C.M. Smith, D.A. Hucul, J. Blackson, G. Salaita, Applied Catalysis A: General 282 (2005) 111-121.

[24] T.W. Hansen, A.T. DeLaRiva, S.R. Challa, A.K. Datye, Accounts of Chemical Research 46 (2013) 1720-1730.

[25] Z. Jin, D. Nackashi, W. Lu, C. Kittrell, J.M. Tour, Chemistry of Materials 22 (2010) 5695-5699.

[26] S.B. Simonsen, I. Chorkendorff, S. Dahl, M. Skoglundh, S. Helveg, Surface Science 648 (2016) 278-283.

[27] A.K. Datye, Q. Xu, K.C. Kharas, J.M. McCarty, Catalysis Today 111 (2006) 59-67.

Chapter 6

Preliminary effort to quantify Pd-CeO_2 interactions

Introduction

To date, the study of core@shell material in this dissertation progressed from synthesis to application and then to a means of studying a material's catalytic properties. Such progress was possible, because the versatile synthesis method allows preparation of many different types of core@shell materials. In this chapter, a more creative use of the core@shell nanomaterials is suggested. Here, we introduce a quantification method for metal-support interactions using Pd@CeO_2 catalysts. The quantification, which would be very difficult with the traditional catalyst designs, was simplified by the unique geometry.

An observation in Chapter 4 is the evidence of oxygen donation from CeO_2 to Pd via metal-support interaction, which is well-known in the field of catalysis [1-5]. To date, articles regarding the interactions focus on demonstrating the presence of such interactions and the effects on the catalytic activity at the interface [6-8]. However, the answer to the following question is not easy to find: How far do "interfaces" extend? In other words, in a system composed of Pd and CeO_2 (which are known to interact), how much oxygen from CeO_2 can be supplied to Pd to participate in catalysis? At first, it seems that the answer can be simply deduced by measuring the amount of lattice oxygen liberated by a reducing agent [9-11]. However, it

turns out that the answer may not be so simple. We realized that the quantification of the interaction boundary was very difficult with conventional catalyst morphologies. The reason is that uniform distances between Pd particles cannot be guaranteed using traditional preparation methods, as represented in Figure 6.2. Without a uniform distribution of the Pd particles, quantitative measurement of oxygen donated by CeO_2 is impossible. In particular, such non-uniform distribution will result in inaccurate result, if the "interface" extends further out from the immediate neighboring atoms. Moreover, even if uniform distribution is achieved, the oxygen contribution from CeO_2 underneath Pd particles cannot be quantified.

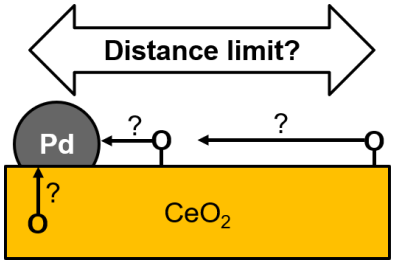

Figure 6.1 Illustration of the "distance limit of interaction" between Pd and CeO_2

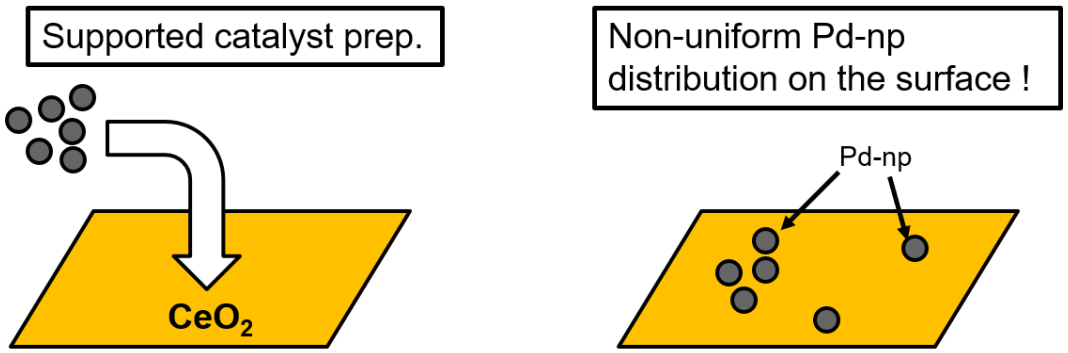

Figure 6.2 Illustration of the difficulty posed by the supported catalyst system in terms of quantifying/measuring the distance of interaction

The answer to the above question may be derived by measuring the amount of oxygen donation by CeO_2 in core@shell nanomaterials. In a core@shell geometry, the metal core is surrounded by the shell in all directions, eliminating the possibility of "overlapping" interactions

between two Pd particles. Furthermore, the geometry imposes spherical symmetry to the system, which can significantly simplify the calculation. By assuming all Pd surface atoms are interacting with the CeO_2 shell in a concentric geometry, the amount of oxygen donated from the CeO_2 shell can be related to the shell thickness. Therefore, by comparing the amounts of oxygen donated by Pd@CeO_2 catalysts with different shell thicknesses, the "extent" of the interaction can be obtained. The "extent," once calculated, can be used to suggest the optimum ratio between the metal (Pd) and the active support (CeO_2). Upon successful completion, this study will provide new insights into quantifying the metal-support interaction and designing a catalyst with maximized interaction.

Experimental

Preparation of the Pd@CeO_2 catalysts

Pd@CeO_2 catalysts with different thicknesses were prepared by following the procedure outlined in Chapter 3. Overall, Pd@CeO_2 catalysts with three different shell thicknesses were prepared, while keeping the Pd core size constant. The shell thickness was controlled by varying the amounts of CeO_2 shell precursor. In addition, three different Pd core sizes were prepared, following the core size control introduced in Chapter 2. Lastly, two more reference materials (Pd@SiO_2, CeO_2 only) were prepared as controls. Pd@SiO_2 was used to estimate the amount of oxygen from PdO reduction. CeO_2 without Pd core was used as a reference to Pd@CeO_2 catalysts in order to measure the amount of released oxygen without the Pd.

Measuring the amount of oxygen from CeO_2

The amount of oxygen donation from CeO_2 was measured by temperature programmed reduction (TPR) by CO, within thermogravimetric analysis (TGA) equipment. In a brief description, more than 200 mg of each catalyst was loaded to a TGA with platinum pan. After a stable mass reading was obtained, the catalyst was first oxidized in-situ by air at 500 °C for 2 hours to remove any residual organics and to ensure full oxidation of the catalyst. After oxidation, the furnace was cooled to 50 °C, at which the atmosphere was switched to nitrogen for 90 minutes. Following the N_2 flush, CO was adsorbed at 50 °C by flowing 1% CO (bal. N_2) at 100 ml/min for 90 minutes. After adsorption, the temperature was ramped up at 10 °C/min to 500 °C under the CO flow.

Preliminary Results

To begin measuring the amount of transferred oxygen, a minimum of four catalysts are needed: two $Pd@CeO_2$ with different shell thicknesses, $Pd@SiO_2$, and CeO_2 only. First, a $Pd@CeO_2$ catalyst with a "regular" shell thickness was used as a standard. Another $Pd@CeO_2$ catalyst with thicker shell was prepared to observe any possible increase in the amount of transferred oxygen. Two additional catalysts were used as reference materials.

The $Pd@SiO_2$ catalyst was used to calculate the amount of oxygen that evolves from PdO -> Pd reduction, despite the fact that the amount of Pd within each $Pd@CeO_2$ catalyst was expected to be minimal. As a second reference, CeO_2 nanoparticles, without Pd cores, were prepared using the same synthesis method. As the oxygen storage capacity (OSC) and oxygen transferability can significantly change depending on the preparation method, it was important to synthesize CeO_2 using the same method. This second reference was used to quantify the

increased amount of oxygen release due to interaction, if any. The catalyst preparation was confirmed by TEM. As shown in Figure 6.3, Pd@SiO_2, Pd@CeO_2 with two different shell thicknesses, and CeO_2 without Pd core were successfully prepared. All samples were dried at 80 °C and calcined at 500 °C for 2 hours under ambient air prior to TPR analysis, in order to remove residual organic compounds.

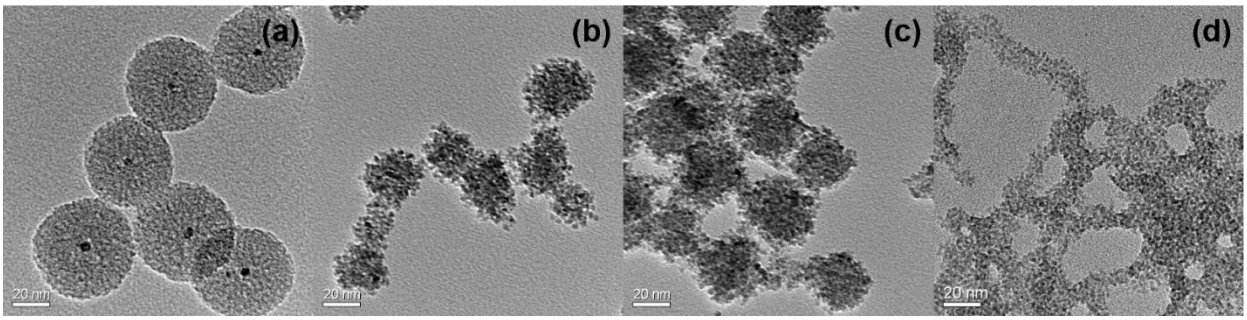

Figure 6.3 Catalysts prepared to measure the amount of oxygen transferred from CeO_2 to Pd. (a) Pd@SiO_2 (Pd = 1.2%), (b) Pd@CeO_2 (regular shell, Pd = 0.9%), (c) Pd@CeO_2 (thicker shell, Pd = 0.4%), and (d) CeO_2 only.

After the synthesis, the amount of oxygen release was measured by CO-TPR in a TGA instrument. An example analysis scheme is shown in Figure 6.4. The catalyst, pretreated under oxygen, was purged with N_2, then swept with CO. The initial mass gain, denoted by ① in Figure 6.4 is the result of CO adsorption as carbonate. As the temperature increases, this species decomposes as CO_2, taking oxygen from the catalyst. The amount of oxygen loss was measured by comparing the weight of the catalyst prior to CO adsorption and after the first weight loss peak, which is commonly denoted as the interfacial oxygen [9]. This way, the complication caused by the simultaneous formation/decomposition of carbonate was eliminated.

The preliminary results of CO-TPR experiments are shown in Table 6.1. As shown in Table 6.1, the largest amount of oxygen release is observed when Pd and CeO_2 are in contact. However, the amounts were not different between two core@shell catalysts with different shell

thicknesses ($Pd@CeO_2$ vs. $Pd@2CeO_2$). This indicates that the extent of oxygen transfer must be very short, possibly limited only to the CeO_2 nanocrystals in direct contact. Therefore, further work is suggested to accurately calculate the extent of interaction.

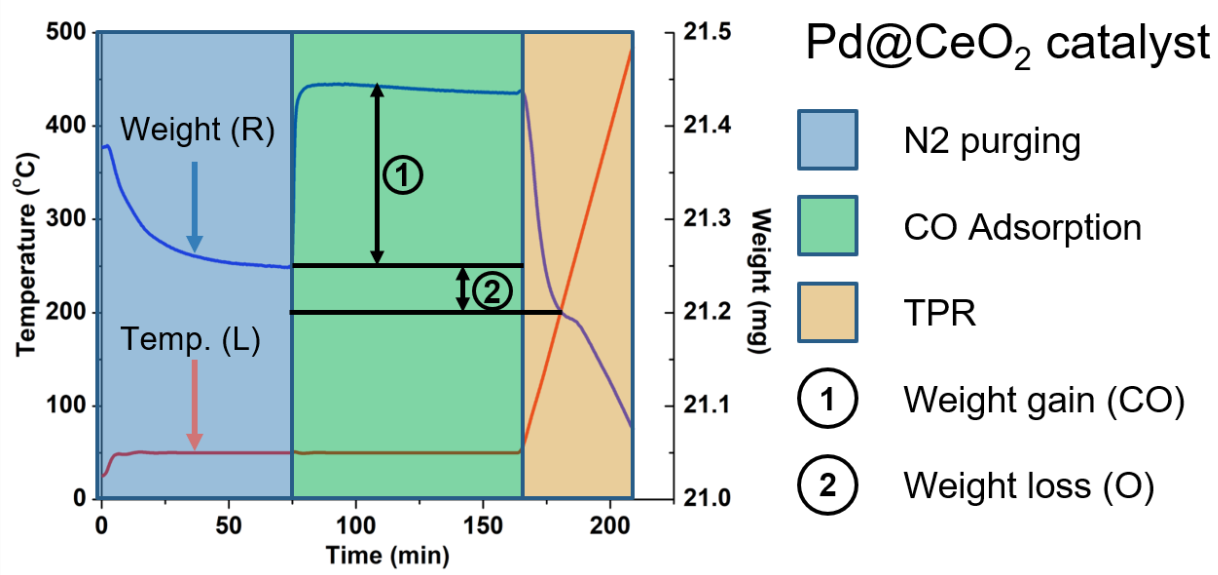

Figure 6.4 Example CO-TPR scheme on $Pd@CeO_2$ catalyst used to measure the amount of oxygen released from the catalyst. Other catalysts were tested following the same procedure

Table 6.1 Summary of the oxygen released by CO-TPR.

Sample Type	Weight % of Pd	Released amt. of O (wt. %)
$Pd@SiO_2$	1.2	0.06
$Pd@CeO_2$	0.88	0.26
$Pd@2CeO_2$	0.33	0.24
CeO_2 only	N/A	0.14

Summary and remaining work

The quantification of Pd-CeO_2 interaction was initiated by using core@shell catalysts. Being able to quantify the amount (or extent) of interaction will naturally lead to designing a catalyst with an optimum ratio between the metal and an active support, which often involves rare-earth metaloxide. So far, the approach involved controlling the thickness of the CeO_2 shells

with the same size Pd cores to observe the change in oxygen loss, if any, under CO-TPR. This way, the number of interaction sites between Pd and CeO_2 remained similar between catalysts while the total available oxygen could be varied based on the thickness of the shell. Based on the preliminary result, the prepared samples' CeO_2 shells have already reached the maximum thickness for the oxygen transfer. Therefore, further research is needed to accurately quantify the interaction.

To advance this study, two different sets of experiments need to be completed. First, a thinner CeO_2 shell can be prepared to check if the amount of oxygen transfer is affected by the thickness. If thinner shell shows decreased amount of oxygen release, then the distance limit of metal-support interaction can be calculated based on the result. However, there is a possibility that the thinner shell may not yield a decreased amount of oxygen release. In this case, the core size must be varied to further demonstrate that the amount of oxygen release is dependent on the number of sites that are located at very close proximity. For example, by decreasing the Pd core size while keeping a constant loading, the number of interaction sites between Pd and CeO_2 will increase. If the amount of oxygen release increases proportionally, then it can be concluded that the "extent of interaction" is limited to perimeter sites around the Pd core.

Lastly, a structure such as $Pd@SiO_2@CeO_2$ can be prepared to check if the low temperature oxygen release requires direct contact between Pd and CeO_2. This catalyst design, which was demonstrated in Chapter 3, allows the system to contain oxygen storage capacity (OSC). However, the middle SiO_2 layer does not allow direct contact between Pd and the OSC material. By comparing it with a catalyst with a reverse shell geometry, $Pd@CeO_2@SiO_2$, with both OSC and metal-support interaction, the increased amount of oxygen release can be further examined. This comparison can also shine a light to another interesting topic: OSC vs. activity.

Often, the materials with OSC promote the oxidation activity of a catalyst. However, the relationship between the OSC and activity is not well-defined. This question may be answered by using catalysts with ideal compositions and OSC but different geometries that controls the metal-support interaction.

References

[1] A.K. Datye, D.S. Kalakkad, M.H. Yao, D.J. Smith, Journal of Catalysis 155 (1995) 148-153.

[2] Y. Gao, W. Wang, S. Chang, W. Huang, ChemCatChem 5 (2013) 3610-3620.

[3] S.J. Tauster, S.C. Fung, R.T.K. Baker, J.A. Horsley, Science 211 (1981) 1121-1125.

[4] S.J. Tauster, S.C. Fung, R.L. Garten, Journal of the American Chemical Society 100 (1978) 170-175.

[5] J. Zhang, L. Li, X. Huang, G. Li, Journal of Materials Chemistry 22 (2012) 10480-10487.

[6] L. Artiglia, F. Orlando, K. Roy, R. Kopelent, O. Safonova, M. Nachtegaal, T. Huthwelker, J.A. van Bokhoven, The Journal of Physical Chemistry Letters 8 (2017) 102-108.

[7] B. Li, T. Gu, T. Ming, J. Wang, P. Wang, J. Wang, J.C. Yu, ACS Nano 8 (2014) 8152-8162.

[8] T.P. Senftle, A.C.T. van Duin, M.J. Janik, ACS Catalysis 7 (2017) 327-332.

[9] H. Zhu, Z. Qin, W. Shan, W. Shen, J. Wang, Journal of Catalysis 225 (2004) 267-277.

[10] M.-F. Luo, Z.-Y. Hou, X.-X. Yuan, X.-M. Zheng, Catalysis letters 50 (1998) 205-209.

[11] J.B. Park, J. Graciani, J. Evans, D. Stacchiola, S.D. Senanayake, L. Barrio, P. Liu, J.F. Sanz, J. Hrbek, J.A. Rodriguez, Journal of the American Chemical Society 132 (2009) 356-363.

Chapter 7

Future directions and conclusions

Future Directions

Core@shell materials: An interesting research tool

In Chapter 5 and 6, creative uses of core@shell materials have been introduced. Based on such findings, some other foreseeable research pathways are suggested in Figure 7.1. By securing a versatile synthesis method, expansion of the research in the field of catalysis and materials science can be envisioned. In the field of catalysis, core@shell materials can be used to quantify and rank metal-support interaction. For example, the metal-support interaction between Pd and TiO_2 vs. Pd and CeO_2 cannot be simply compared by preparing two catalysts with identical loadings. The reason is that the dispersion of the metal will be different depending on the support's characteristics. Also, as mentioned above, the even distribution of the particles cannot be guaranteed with the traditional design. In addition, a common annealing step used to clean the catalyst's surface may induce sintering, which will affect the comparison. However, by using core@shell catalysts, a much better comparison can be carried out, because core@shell catalysts offer a stable geometry with isolated metal particles with possible metal-support in all

directions. Such research would enable the ranking of different support (shell) materials for their ability to interact with the metal to enhance catalytic activity or selectivity.

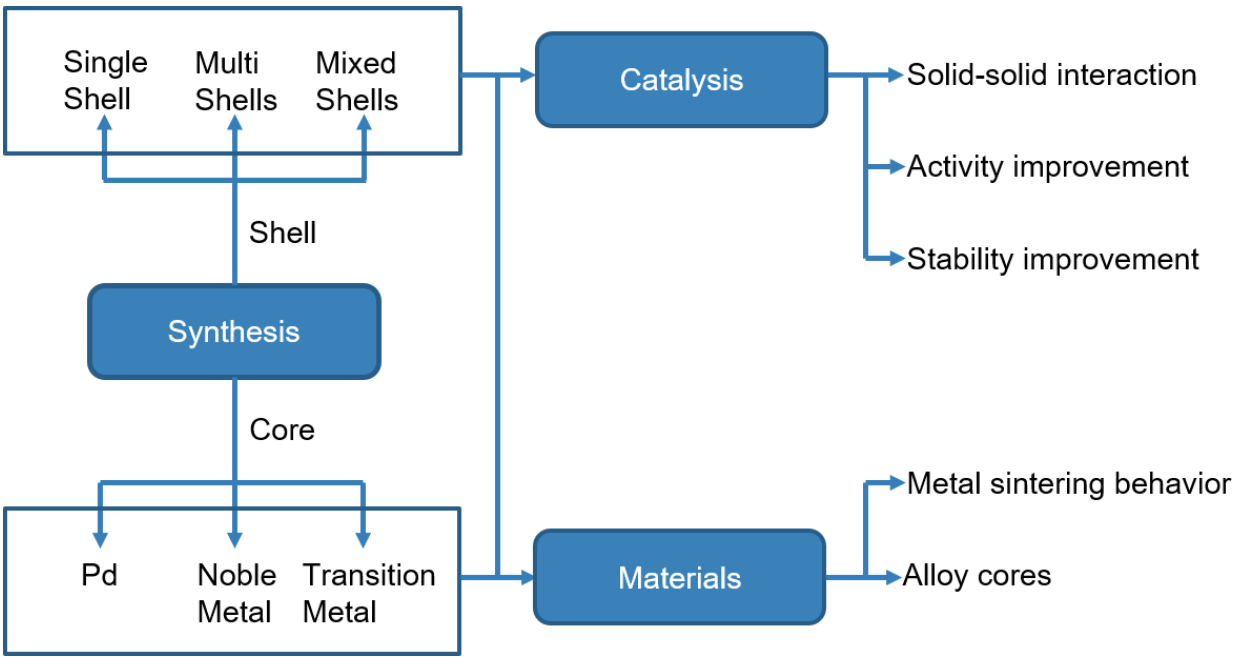

Figure 7.1 Graphical summary of the future directions which may originate from the synthesis method

In the perspective of materials research, core@shell materials can offer different viewpoints for metal sintering. As studied in Chapter 5, core@shell materials may show different sintering behavior at elevated temperature. This unique discovery is highly encouraging, because it provides a method of preparing thermally stable catalysts. Therefore, a similar study can be carried out under different atmospheres and with different formulations. For example, a similar study carried out with $Rh@SiO_2$ catalyst shows a very different response from $Pd@SiO_2$ catalyst (Figure 7.2). In $Rh@SiO_2$, instead of redispersion, significant migration of Rh is observed after high temperature aging. Another significant advantage of using core@shell material in such studies is that the geometry offers a very clear view of any change in morphology. In a core@shell catalyst, the distinction between the core and the shell is very clear. Therefore, small changes that may need to be speculated by a supported catalyst has higher chance to be observed

by a core@shell catalyst. By using such advantages, new ways of researching the sintering mechanism of metal particles can be envisioned, which will ultimately provide a better catalyst design and composition.

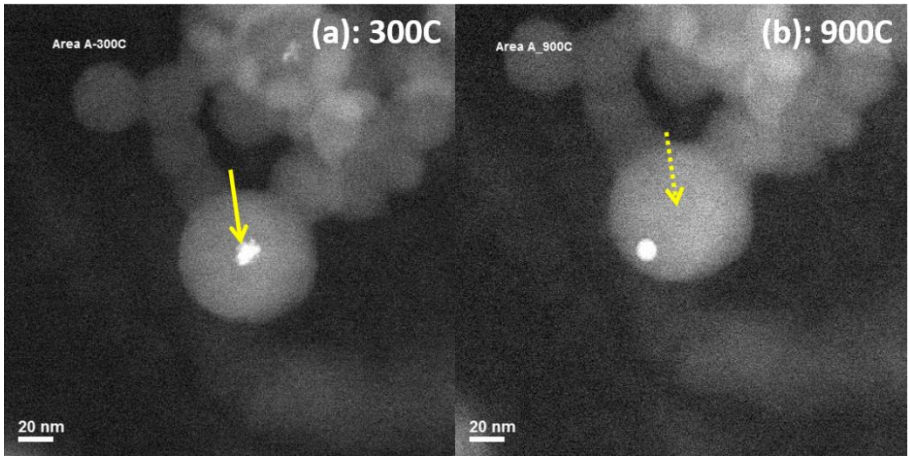

Figure 7.2 *in situ* TEM experiments on $Rh@SiO_2$ catalyst (yellow arrow: Rh). The experiment was carried out under the same conditions as $Pd@SiO_2$ (Chapter 5).

Conclusions

Since catalysts serve such a critical role in solving the environmental and energy problems of the present and the future, developing catalytic materials with improved stability, activity, and durability is a topic with huge interest from both academia and industry. Recent development in core@shell nanomaterial synthesis has shown a new pathway towards achieving such catalysts with interesting geometries such as core@shell. So far, various core@shell catalysts, composed of an active metal core and a stable oxide shell have been synthesized to demonstrate improved stability, activity, and selectivity. However, the synthesis methods have been too expensive to be scaled up for practical use. In addition, most of reports focus on preparation of the catalysts, when other interesting studies can be carried out using the special

geometry. In this dissertation, a simpler synthesis method for core@shell nanomaterials is designed and studied in detail to lay down a basis for creative usage of core@shell materials.

Chapters 2 and 3 illustrate the effort to simplify core@shell material synthesis. In Chapter 2, Pd@SiO_2 catalysts with different core and shell sizes were prepared by carefully studying the parameters that control the Pd core size and the SiO_2 shell thickness. Based on the outcome of both successful and unsuccessful synthesis trials, a governing Pd@SiO_2 formation mechanism was deduced. Studying the formation mechanism was very important, because the mechanism could answer a few unanswered synthesis questions posed by others, such as the formation of empty shells and connected particles. In addition, the mechanistic study enabled the synthesis of Pd@SiO_2 with independent tunability of the core size and the shell thickness at a wide range. A superior thermal stability up to 850 °C was observed from the prepared Pd@SiO_2 catalysts.

Once the basis of facile synthesis method was established, the synthesis was expanded to other shell material, CeO_2. Traditionally, synthesis of CeO_2 shell required many steps and highly controlled hydrolysis due to high reactivity of CeO_2 precursor with water. In this chapter, a modification of the CeO_2 precursor retarded the hydrolysis, allowing the core@shell geometry to form over an extended period of time. Once the precursor was found, Pd@CeO_2 catalysts could be prepared in water, with the same method studied in Chapter 2. Here again, the Pd core sizes and CeO_2 shell thicknesses were independently tunable. Another interesting outcome of this synthesis expansion was that the synthesis method could be applied to prepare a shell composed of more than one oxide. By combining two shell materials together, we could achieve higher thermal stability of the catalyst, which is difficult to achieve with the CeO_2 shell alone.

In Chapter 4, the prepared core@shell materials were used as three-way catalysts. The applicability of the core@shell material was explored as a 3-Way catalyst under realistic reaction as well as aging conditions. Because of the versatility of the synthesis method, many types of catalysts containing Pd, Rh, SiO_2, CeO_2, ZrO_2, TiO_2 were prepared under similar conditions. The prepared catalysts were aged and tested under 3-Way reaction conditions which includes hydrothermal and redox aging environments up to 850 °C. Through this study, a design optimization of core@shell catalysts was attempted for this application. For example, incorporating CeO_2 drastically enhanced the activity. On the other hand, the addition of ZrO_2 did not improve the activity but improved hydrothermal stability. However, after testing many types of materials, it was concluded that the 3-Way conditions were indeed too harsh for the catalysts to retain their unique architecture. Furthermore, despite the simple and inexpensive production method, the production volume per batch was limited to only lab-scale production. Therefore, it was concluded that that another breakthrough in synthesis is required prior to the application of core@shell catalysts in real-life applications.

Since an industrial application of core@shell catalysts would require a significant amount of time and effort, the use of material was shifted to encourage fundamental understanding of materials. In Chapter 5, the thermal stability of Pd@SiO_2 and disappearance of some Pd cores observed in Chapter 2 were revisited. The focus was to elucidate the improved CO oxidation activity of the catalyst improved after aging at high temperature. By revisiting the problem under high resolution TEM as well as *in situ* environmental TEM, direct evidence of Pd redispersion was obtained, which was not observed with a supported catalyst. Following, the mechanism for redispersion was established. The mechanism explains that the Pd cores underwent vaporizing/melting followed by redepositing as atom clusters, after high temperature aging. This

discovery may explain the reason behind a core@shell catalyst's improved thermal stability and may lead to future design of catalyst with improved thermal stability.

Lastly, initial efforts to answering another topic in catalysis using core@shell materials are introduced. Here, the focus was on the fact that the core is in close contact with the shell, in all directions. By using this geometry, the quantification of the metal-support interaction between Pd and CeO_2 was attempted. So far, the initial efforts show that there is a limit to the oxygen transfer distance from CeO_2 to Pd. However, the transfer limit could not be quantified, as it required preparation and analysis of more samples than initially anticipated. Nonetheless, the quantification of the metal-support interaction is certainly a very interesting research topic that can be better answered by using core@shell catalysts, along with some other questions in catalysis and materials.

In summary, this dissertation illustrates a series of efforts to prepare core@shell catalysts with improved stability and activity. The investigation began with careful analysis and deducing the formation mechanism of core@shell nanoparticles with a facile synthesis method. The developed synthesis method acted as the foundation of this study, as the method's versatility allowed preparation of many different formulations. The ability to prepare many types of nanomaterials allowed us to pose two interesting questions:

- Why are core@shell materials often more thermally stable?
- Can we use the well-defined geometry of core@shell systems to study fundamental questions such as how far lattice oxygen from the support can transfer to the active metal sites via metal-support interactions?

The first question was answered clearly via a comparative study between Pd@SiO_2 and Pd/SiO_2 at elevated temperature up to 800 °C. By combining the synthesis technique, TEM characterization, and catalytic oxidation of CO, we found that the catalyst architecture can significantly impact the sintering mechanism. We discovered that in core@shell structures, one of the major contributions to sintering, namely particle agglomeration, is effectively shut down. Furthermore, we discovered that the Ostwald ripening process leads to redispersion of the Pd cores in form of atomic clusters, inside the SiO_2 shell pores. The mechanism we found illustrated that it is important to confine small Pd particles within the oxide shell to retain good thermal stability. This discovery provides a new insight in designing thermally stable catalysts, which can impact the operation of three-way catalysts as well as reforming catalysts which require exposure to high temperatures.

Regarding the second question, an initial, creative method of measuring the extent of metal-support interaction was proposed. The core@shell geometry offers an opportunity to study the effect of shell thickness. Our approach to measuring the transfer distance of oxygen from CeO_2 to Pd was to vary the CeO_2 shell thickness and Pd core sizes and carry out CO oxidation in absence of gas-phase oxygen. We hoped to find the critical shell thickness where oxygen is capable of interacting with Pd. Preliminary results reported in this thesis, with two different CeO_2 shell thicknesses (12 nm and 20 nm) did not provide clear enough evidence and further experiments spanning a wider range of shell thicknesses may be necessary. However, the approach to this problem is promising and being able to clearly calculate the limits of interactions will provide a great benefit in optimizing the design of future catalysts.